Improved modeling of nanocrystals from atomic pair distribution function data

Soham Banerjee

Submitted in partial fulfillment of the

requirements for the degree

of Doctor of Philosophy

in the Graduate School of Arts and Sciences

COLUMBIA UNIVERSITY

2020

ABSTRACT

Improved modeling of nanocrystals from atomic pair distribution function data

Soham Banerjee

Accurate determination of the structure of nanomaterials is a key step towards understanding and controlling their properties. This is especially challenging for small nanoparticles, where traditional electron microscopy provides partial information about the morphology and internal atomic structure for a limited number of particles, and x-ray powder diffraction data is often broad and diffuse and not amenable to quantitative crystallographic analysis. In these cases a better approach is to use atomic pair distribution function (PDF) analysis of synchrotron x-ray total scattering data, in tandem with high-resolution imaging techniques. Even with these tools available, extracting detailed models of nanoparticle cores is notoriously difficult and time consuming. For many years, poor fits were considered to be a *de facto* limitation of nanoparticle studies using PDF methods, and semi-quantitative analyses were commonly employed.

We started with a survey of 12 canonical metallic nanomaterials, both elemental and alloyed, prepared using different synthesis methods, with significantly different shapes and sizes as disparate as 2 nm wires and 40 nm particles, using PDF data collected at multiple synchrotron sources and beamlines. Widely applied shape-tuned attenuated crystal (AC) fcc models proved inadequate, yielding structured, coherent, and correlated fit residuals. How-

ever, equally simple discrete cluster models could account for the largest amplitude features in these difference signals. A hypothesis testing based approach to nanoparticle structure modeling systematically ruled out effects from crystallite size, composition, shape, and surface faceting as primary factors contributing to the AC misfit, and it was found that these previously ignored signals could be explained as originating from well defined domain structures in the nanoparticle cores. This analysis gave insight into how sensitive PDF techniques could be towards identifying the presence of interfaces inside ultrasmall nanoparticle cores using atomistic modeling, but still hinged on manual trial-and-error testing of clusters from different structural motifs. To address this challenge, we developed a structure screening methodology, called cluster-mining, wherein libraries of clusters from multiple structural motifs were built algorithmically and individually refined against experimental PDFs. This differs from traditional approaches for crystallographic analysis of nanoparticles where a single model containing many refinable parameters is used to fit peak profiles from a measured diffraction pattern. Instead, cluster-mining uses many structure models and highly constrained refinements to screen libraries of discrete clusters against experimental PDF data, with the aim of finding the most representative cluster structures for the ensemble average nanoparticle from any given synthesis. Finally, we wanted to identify other nanomaterial systems where this approach might prove useful, and demonstrated that the PDF was also capable of detecting seemingly subtle morphological variations in highly faceted TiO_2 photocatalyts. This opens a new avenue towards characterizing shape-controlled metal oxide nanomaterials with well-defined surface facets. To extend this work in the future, our goal is to develop new tools for building discrete nanoparticles algorithmically, integrate statistical approaches to make model selection more efficient, and ultimately, move towards an atomic scale understanding of nanoparticle structure that is comparable to bulk materials.

Table of Contents

List of Figures

List of Tables

Acknowledgments

First and foremost, I would like to thank Simon Billinge, without whom I would not be the scientist or person I am today. I joined his group as a scatterbrained young student with ambitious goals of tackling any and all problems that came my way. Simon taught me that in research, it's important to explore many topics, but to prioritize finding the interesting questions that best leverage my own skills and expertise. Communicating scientific results was also a challenge, but he gave me a few important guidelines I won't soon forget: say what you know, say it simply, and say it with confidence. This was part of the culture in our group during my PhD, and it allowed us to tackle scientific concepts together, without clouding discussions with partial information and jargon. It was a privilege being mentored by Simon during this journey, and at every hurdle, he was there to provide optimism and foresight. It is rare to find an adviser that cares so deeply about all of their students finding success and happiness, and I was lucky enough to have that.

I would also like to acknowledge my group-mates and friends at Columbia including Max Terban, Tim Liu, Kirsten Jensen, Zurab Guguchia, Long Yang, Chris Wright, Anton Kovyakh, Elizabeth Culbertson, Songsheng Tao, Yevgeny Rakita, Ben Frandsen, Xiaohao Yang, Chenyang Shi, Neno Fuller, Baruch Tabanpour, Karim Mukaddem, and Justin Calamari. Additionally I sincerely thank my mentors at Brookhaven National Lab who taught me much of what I know about x-ray scattering, crystallography, and how to be a good experimentalist: Ian Robinson, Emil Bozin, Yue Cao, Tadesse Assefa, Sanjit Ghose, Eric Dooryhee, Milinda Abeykoon, John Trunk, and Rob Koch.

The scientific results presented in this dissertation would not be possible without my collaborators and coauthors. I am grateful for their insight, patience, and of course their beautiful samples! A special thanks to Matthias Epple and Oleg Prymak at the University

of Duisburg-Essen who set me down the path of investigating the structure of metallic nanoparticles long before my PhD.

Finally, I would like to thank my family. Their unconditional love was a refuge during difficult times. They instilled a belief that no challenge was too big to overcome, and that the ultimate successes are not just scientific, but through personal growth and finding balance.

To my family, friends, and the process.

Chapter 1

Introduction to nanoparticles and their structural characterization

Nature has always exploited the unique properties of matter that emerge at the nanoscale. Many of the functional structures in living cells that carry out our most essential life-preserving processes are nanometer-sized, and have been engineered over millennia to operate, more often than not, precisely and reproducibly. Scientists have also worked at the nanoscale for a long time, but mimicking nature and manipulating the building blocks of matter is an exceptionally challenging endeavor. To do so, it is not sufficient to understand the properties of the smallest constituent unit, the atom, nor can we consider nanomaterials as miniaturized versions of their macroscopic counterparts. These obstacles are also what make nanoscience exciting. Emergent properties, often with tantalizing technological prospects, drive new questions, push our ability to control materials, and necessitate the development of probes able to examine nanoscale phenomena at a fundamental level.

Nanoparticles, or nanocrystals, are broadly categorized as finite sized structures, with at least one dimension between 1 and 100 nanometers. At the simplest level, the distinct

properties of nanoparticles can be attributed to the increased role of their external surfaces, which can be manipulated by changing experimental parameters in a synthesis to obtain particles of a certain size, shape and composition. For some perspective on this dramatic change in surface area to volume ratio, consider a 1 cm^3 cube with a surface area of 6 cm^2, slightly larger than a postage stamp. The same cube divided into 1 nm^3 blocks has a surface area of 6,000 m^2, or approximately the area of 15 basketball courts placed end to end. Although we sometimes think of *particles* as strictly spherical objects, the terminology is used to describe structures exhibiting a variety of anisotropic morphologies and specific crystallographic habits [142]. Atoms at the surfaces of nanoparticles have undercoordinated or dangling bonds that allow them to be functionalized with adsorbates such as organic ligands. This not only helps stabilize the nanocrystal as a whole, but ligands and surfactants can also preferentially attach to specific facets, thereby changing the relative free energies of different surfaces, leading to anisotropic growth [145]. Nanocrystals with complex morphologies are typically in metastable, kinetically frozen states where high fractions of edge and corner-like regions serve to enhance spatial confinement phenomena that cannot be achieved in the isotropic case alone [1]. Collectively, surface functionalization and shape-controlled growth are some of the most intensely pursued avenues towards tailoring the properties of nanoparticles, with diverse applications including, but not limited to, catalysis [81, 153, 144], plasmonics [9, 83], energy conversion [7, 52], and biomedicine [109, 143, 2, 114, 49, 26]

The properties of nanocrystals are also often thought of as a bridge between molecules and crystalline solids. When a particle, or an assembly of atoms, increases in size from the angstrom to nanometer and micrometer scale, several important changes occur, some of which are illustrated in Fig. 1.1. Discrete energy levels turn into a continuous band structure, electrons confined in molecular orbitals become delocalized, and molecular symmetry transitions to a long range ordered crystalline lattice [5]. From low temperature optical spec-

troscopy one signature of these changes in thiolate capped gold clusters is that well-defined sharp features in the absorption spectra, indicative of a molecule with a discrete electronic structure, transitions to a spectrum with broad, bulk-like, or plasmonic features at a critical size between 144-187 atoms [112, 80], as shown in Fig. 1.1(c). However, this division be-

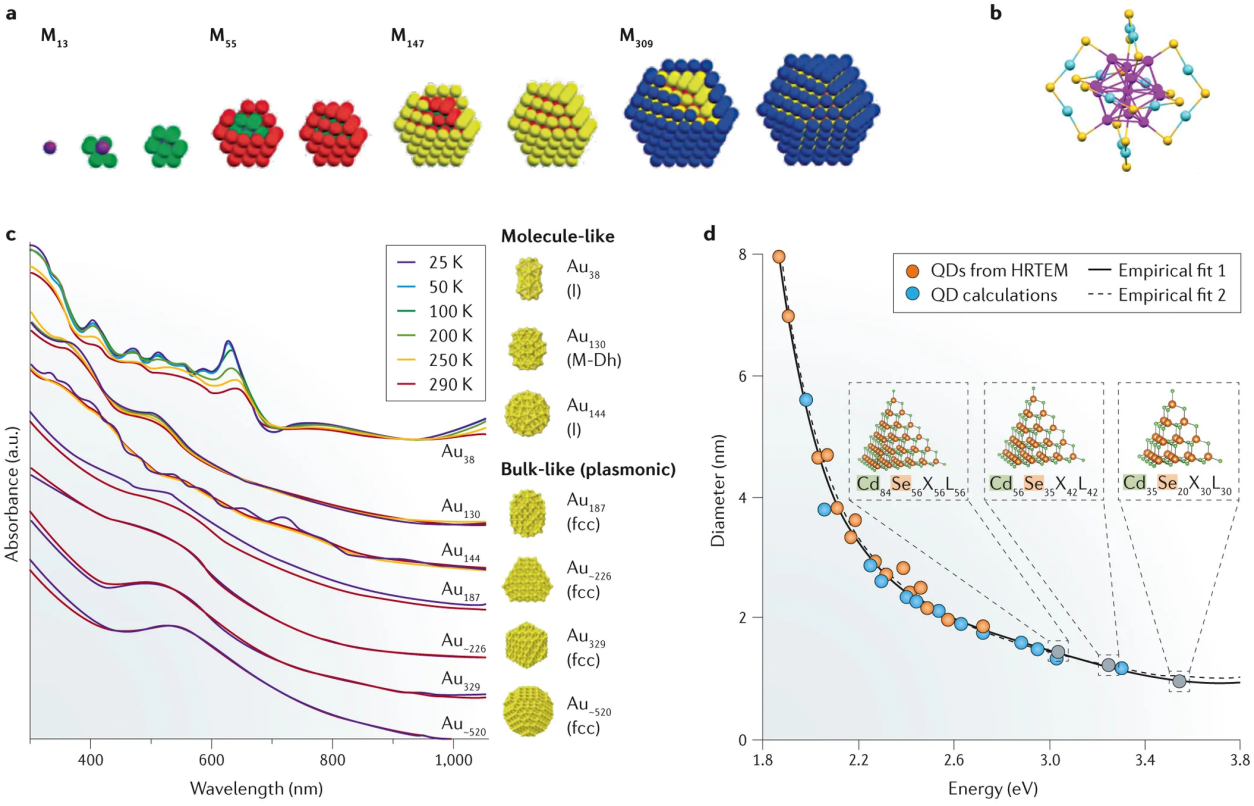

Figure 1.1: (a) A series of *magic* closed-shell cuboctahedra (b) $[Au_{25}(SR)_{18}]^-$ superatomic cluster (SR: thiol ligand) with a 13 atom icosahedral core capped with 6 $Au_2(SR)_3$ staples [138] (c) Temperature dependent optical absorption spectroscopy for a series of Au clusters with increasing size (M-Dh: Marks decahedral, I: Icosahedral) [112] (d) Size dependent bandgap energies for CdSe clusters and nanoparticles [17]. Adapted with permission from Lee et al., *Nat. Rev. Mater.* 1, 16034. Copyright 2016 Springer Nature. [80]

tween a crystal and it's monomeric building blocks is rather blurry, and there exists a broad spectrum of potential intermediate structures between molecules and solids, depending on

the specific system and synthesis method. These intermediates are typically referred to as nanoclusters, molecular clusters, or in cases where clusters retain some properties of their constituent element, superatoms (Fig. 1.1b).

One common characteristic to many nanoclusters, especially metals and metal chalcogenides, is the presence of discrete atomic configurations with a "magic" number of atoms that are particularly stable energetically and structurally. In bare metal clusters this stability is attributed to their closed-shell structure [99] where the surfaces contain a complete layer of close-packed atoms without vacancies. To generate the next closed shell, only a specific number of atoms can be layered on top, and hence the magic number sequences are discretized (Fig. 1.1a). Although these clusters sometimes adopt simple polyhedral topologies, their internal atomic structures need not be crystallographic to have closed shells.

Characterizing "ultrasmall" nanoclusters, with sizes well below 5 nanometers, containing only hundreds of atoms, is essential to understanding the nature of the molecule-to-solid transition, which in turn guides our ability to predict and tailor how nanocrystals nucleate, restructure, and grow [22, 80]. In order to engineer the next generation of these materials by design, rather than empirical optimization, it is necessary to develop structural probes and modeling methodologies capable of quantifying the arrangements of atoms at the smallest length-scales possible.

1.1 Approaches to nanoparticle characterization

1.1.1 Single crystal solution of atomic clusters

In some cases, nanoclusters can be crystallized and single crystal x-ray methods (SCXRD) used to solve their structures [157, 168, 58, 146, 161]. Structure solution via SCXRD is done by determining structure factor amplitudes directly from measured intensities (typically

for tens of thousands of reflections over all possible crystal orientations), recovering phase information with various algorithms (ie. direct methods, Patterson methods, charge flipping, etc.), and finally obtaining the real space electron density and atomic positions by inverse Fourier transformation of the amplitude and phase data [82, 150, 121]. While this procedure is routine for pristine bulk crystals and small molecules with fewer than 100 atoms that are readily crystalized, nanoclusters, or more generally macromolecules, with hundreds to many thousands of atoms in the asymmetric unit present a limiting case for SXCRD not only because these materials are significantly more challenging to crystallize into micrometer sized grains, but also because the electron density becomes smeared out and atomic positions are thus determined with less resolution [62]. The right panel of Fig. 1.2 shows the atomic structures of the largest gold structures solved by SCXRD (as of October 2017), with a maximum number of atoms of 256, corresponding to a particle size well below ∼3 nm. The left panel of Fig. 1.2 includes the complete structure solution for a specific thiolate capped gold cluster, Au_{146}*p*-MBA_{57} (*p*-MBA: *para*-mercaptobenzoic acid) where we can see how the structure of the 146 atom core are determined together with the ligand units [160].

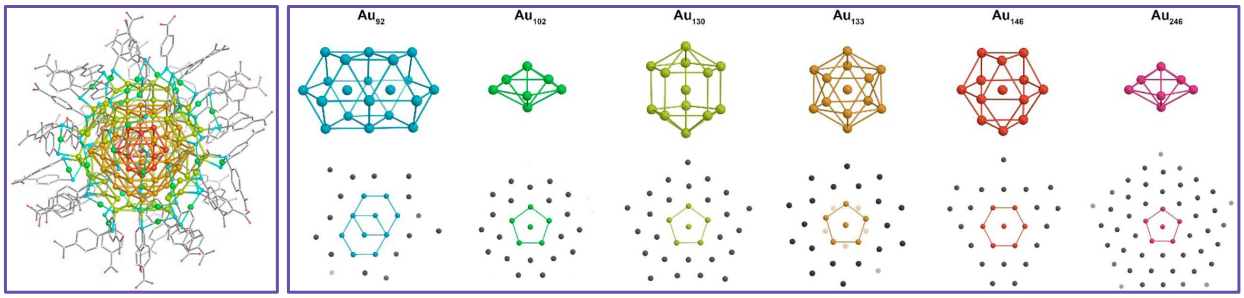

Figure 1.2: Left: Structure of Au_{146}*p*-MBA_{57} (*p*-MBA: *para*-mercaptobenzoic acid) with an anti-cuboctahedral, or singly-twinned core. Right: Atomic structures of the largest gold clusters solved by single crystal x-ray diffraction as of October 2017. Bottom row shows different projections of the clusters. Adapted with permission from Vergara et al., *J. Phys. Chem. Lett.* 8, 5523-5530. Copyright 2017 Americal Chemical Society. [160]

The level of precision with which different atomic structures can be determined with SCXRD for ultrasmall clusters is invaluable, and gives us deep insight into the local structures of atomic cores and ligand coated overlayers. However, this represents a very small fraction of the technologically relevant nanocrystals that are synthesized and studied today. Real nanoparticle systems are often heterogeneous, disordered, present in low concentrations, embedded in supports, and with sizes and preparations that are unamenable to most single crystal methods. A recurring theme in this thesis is taking what can be learned about atomic core configurations (or "kernels") from unique SCXRD solutions, and applying them to a broader survey of nanocrystals.

1.1.2 Traditional Bragg diffraction

Determining the atomic structures of nanoparticles using conventional x-ray powder diffraction methods is difficult [21]. The information obtained in these experiments is degraded not only due to finite size effects, but also because the internal arrangements of atoms deviate significantly from bulk materials. In a bulk micrometer-sized grain thousands of interplanar spacings exist which can be used to determine hundreds of atomic positions. In a nanoparticle with dimensions less than < 5nm, there are typically < 100 lattice planes. The finiteness violates symmetry by limiting translational invariance and by breaking the local coordination of surface atoms. The diffraction pattern from a powder of randomly oriented finite sized crystals, even when the crystal is a perfect chunk of a bulk material, contains very few, broad, featureless, and often asymmetric Bragg peaks. The limited structural coherence makes an imperfect diffraction grating compared to a regular crystal, leading to a considerable amount of diffuse scattering. Should the crystallites contain defects, for example twin planes or stacking faults, the diffraction line shapes are additionally broadened, superimposed on the size dependent broadening effect [34].

Constructing a model to describe a featureless spectrum is a challenge for any scientist, not just crystallographers. Very often what we encounter when it comes to structural characterization of small nanoparticles, especially with laboratory source diffractometers, is a phase identification procedure wherein large intensities in a measured one-dimensional diffraction pattern are indexed based on the expected reflections of a crystallographic unit cell/phase. An example of this is shown in the top panel of Fig. 1.3. Here two sets of reflections, one for a face centered cubic (fcc) unit cell with a lattice parameter for bulk palladium (blue), and one with a significantly smaller fcc lattice parameter for nickel (red), are used to interpret the diffraction patterns from a $Pd_{1-x}Ni_x$ ultrathin nanowire alloy series [84]. This type of indexing is highly qualitative, often misleading, and quite clearly insufficient in terms of describing the measured diffraction pattern. When there is a scientific question or physical property that may be better understood with a more accurate determination of the atomic structure, we can and should aim to do better. We will revisit these same nanowire samples in Chapter 3 of this thesis.

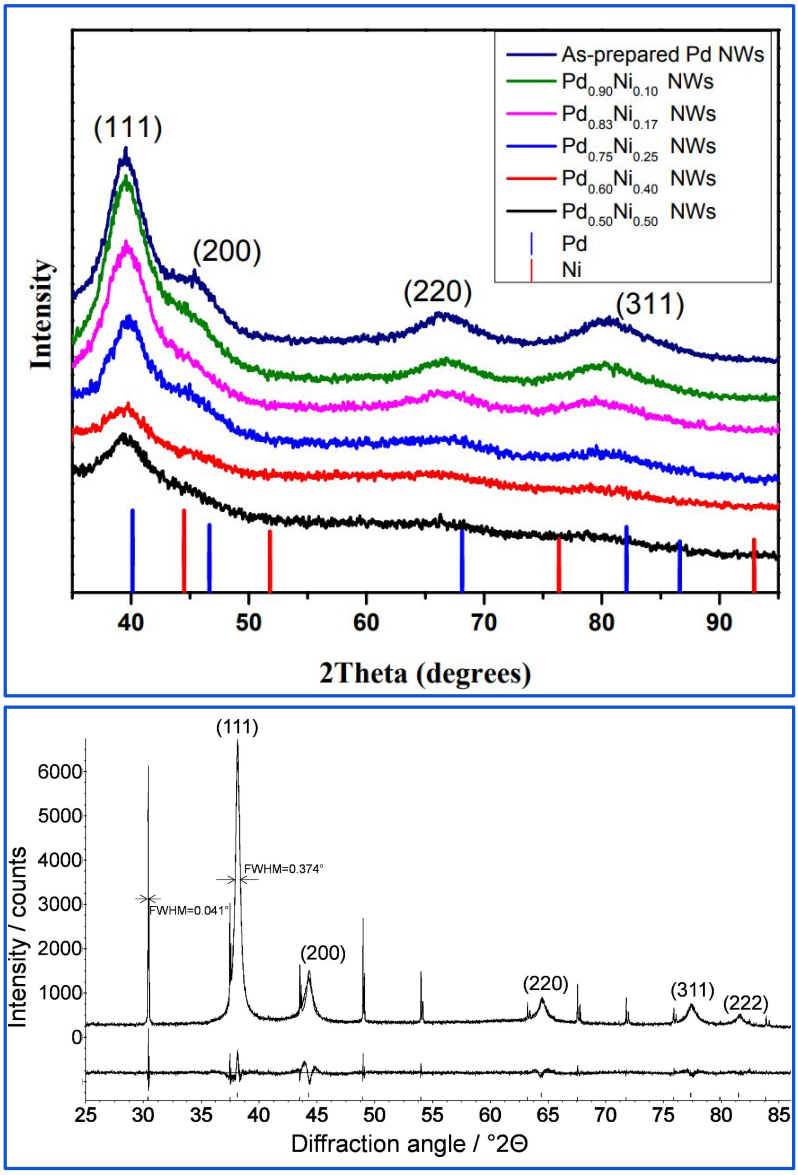

Figure 1.3: Top: Diffraction patterns from ultrathin $Pd_{1-x}Ni_x$ nanowires indexed using fcc Bragg reflections Bottom: Rietveld refinement of Ag nanoparticles mixed with an internal LaB_6 calibrant [13]. Top figure reprinted with permission from Liu et al., *ACS Catal.* 4, 25442555. Copyright 2014 Americal Chemical Society [84]

A step up from phase identification via peak indexing is a quantitative structural refinement of the full powder diffraction pattern using whole-pattern profile methods such as Rietveld [139, 34]. For bulk materials this works well. Unit cell parameters are determined

by peak positions, atomic position parameters are determined by integrated peak intensities, and these are varied within a least-squares regression until the difference between a calculated diffraction profile and the observed signal is minimized. For nanocrystals, and crystallographically challenged materials, a number of other highly parametrized analytical functions are used to remove background intensities, which also removes important information in the diffuse scattering, and select peak shapes (typically by trial and error) to capture effects from reduced grain size, stress, and strain. Again, this can be sufficient for certain nanoparticle systems, especially when particle sizes are on the order of tens of nanometers, and with good angular resolution, common on even lab source diffractometers today, unit cell parameters such as lattice constants can be obtained reliably. An example of this is shown in the bottom panel of Fig. 1.3 where a Rietveld refinement was done on ∼100 nm silver nanoparticles mixed with an internal LaB_6 calibrant, and fit to an fcc model in an attempt to obtain accurate lattice parameters [13]. However, even in this case for large metallic nanoparticles, it is unclear how well the fcc structure model alone describes the data, and clear discrepancies are seen in the fit residual underneath the Bragg peaks. For Rietveld approaches in general, the degrees of freedom in the refinement are often skewed towards the parameters describing the analytical peak shape functions, which can lead to over-fitting and makes it difficult to extract physically meaningful information from refinements, especially for materials with very limited structural coherence. In such cases local structure sensitive powder methods such as total scattering and PDF analysis are quickly becoming the industry standard.

1.1.3 Electron microscopy

Conventional scanning (SEM) and transmission electron microscopy (TEM) are two of the most commonly used methods for characterizing nanoparticles, and have become essential

tools in any study of nanostructure. At a certain level, the importance of these local probes is that one obtains pictures of a nanoparticle or a few nanoparticles, instead of a spectrum or pattern, and the old saying that *seeing is believing* cannot be underestimated. Low magnification micrographs with a wide field of view are readily used to determine particle size, size distribution, and the number density of different particle species in heterogeneous samples [73, 173]. The shape of nanopartcles can also be gleaned from electron microscopy, however these images only provide partial information about the actual morphology [148]. The profiles and particle outlines seen in electron micrographs represent specific projections of a particle. For example an octahedron, cube, and square pyramid may all show an identical profile in an image, depending on their orientation. Moreover, most programs used for segmentation analysis assume spherical cross sections when tabulating a distribution of particle diameters, which is not particularly accurate for nanocrystals with anisotropic morphologies [149].

In Fig. 1.4 we show a few typical characterization steps done with electron microscopy images. Here, SEM micrographs were obtained from a colloidal synthesis of silver nanoparticles where aliquots were extracted as a function of time during the synthesis [13]. The system is heterogeneous with separate populations/phases of "spherical" particles, triangular prisms, and a smaller fraction of rods.

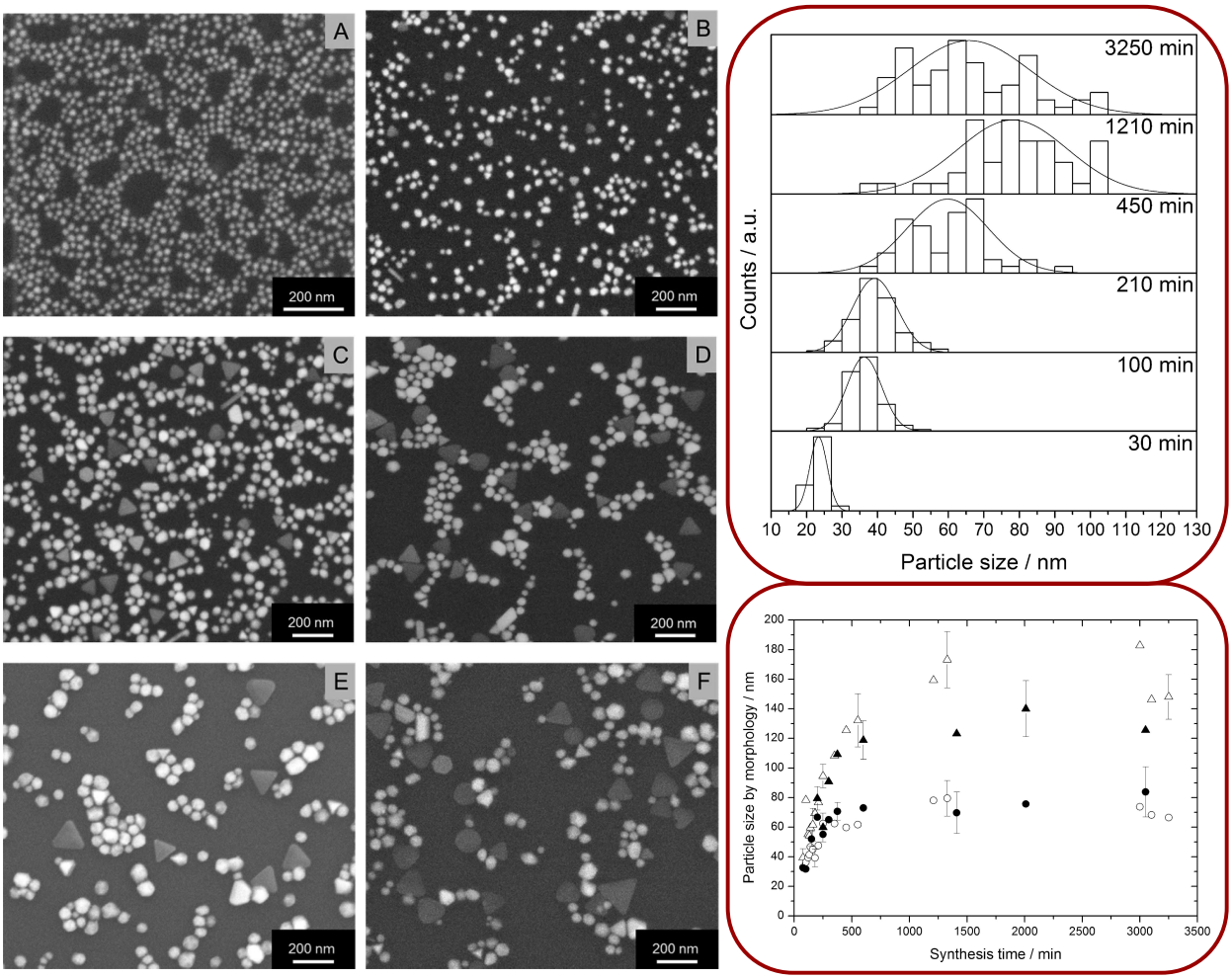

Figure 1.4: Left: Representative SEM images of silver nanoparticles synthesized under reflux and ambient light exposure after 30 (A) to 3250 (F) minutes Top right: Particle size distributions obtained from 200 or more particles sampled as a function of reaction time Bottom right: Particle size for different morphologies vs time: spheres (maximum diameter) and triangles (edge length of a perfect triangle)[13].

The size and relative abundance of the spherical and triangular particles changed with the synthesis time and this was quantified by manually counting at least 200 particles per image/aliquot, and drawing line segments on individual particles to estimate maximum dimensions after calibrating the scale of the images. In many cases experienced microscopists

argue that manual counting methods are in fact more reliable than automated segmentation analysis due to some of the reasons outlined previously, but as one of the researchers tasked with analyzing the images shown in Fig. 1.4, human error and selection bias are simply unavoidable: heavily agglomerated regions of an image are avoided, if sharp boundaries of the particle cannot be discerned the particle isn't counted, and so on. Even the steps taken to deposit nanoparticles on sample holders for SEM and TEM measurements are known to affect the particle size distribution. Despite these obstacles, clearly useful information about the nanoparticles can be obtained from this type of image analysis, but the inherent limitation or feature of the methodology, independent of automated or manual analysis, is that only hundreds of particles are sampled. This is not a statistically representative measure of the average nanoparticle obtained from a given synthesis, where yields can exceed gram scale quantities. In a typical PDF measurement of a nanopowder with a $\sim$0.5 μm^2 beam, and a cylindrical cross-section/volume through a 1.0 mm diameter capillary, on the order of $\sim 10^8$-10^{12} particles with diameters less than 5 nm are averaged in the measured diffraction pattern. It should come as no surprise when crystallite sizes and other ensemble average properties determined from powder diffraction differ from estimates from electron microscopy images. Simply put, the two probes measure different things, and these differences must be considered if a one-to-one comparison is absolutely necessary.

In Fig. 1.5 we show a different situation where low resolution TEM (left panel) and high-resolution TEM images were obtained for ultrasmall palladium NPs. The lower resolution image shows the particles as highly uniform circular dots. The HRTEM image on the other hand blurs this picture, and we see projections of particles that are not only non-spherical, but the images also show an absence of well defined lattice fringes that may suggest that the atomic arrangements inside the particles are not monocrystalline.

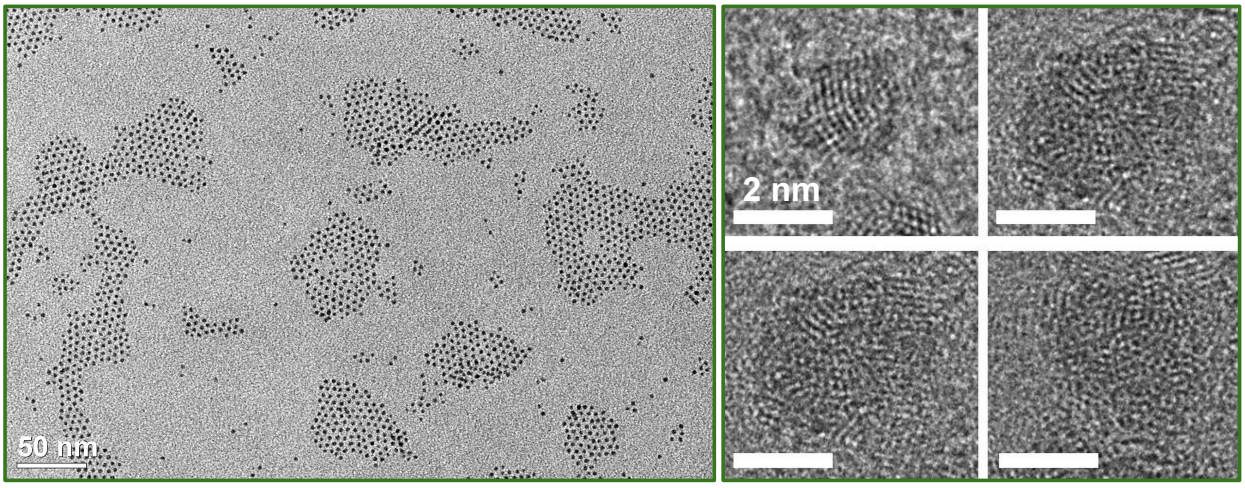

Figure 1.5: Left: TEM image of Pd nanoparticles with an estimated average particle size of 3.0 ± 0.3 nm Right: HRTEM images of isolated particles (all scale bars are 2 nm) [15].

In this sub-5 nm size regime where particles contain hundreds of atoms, TEM and HRTEM microscopy can offer us clues about particle morphology and internal atomic structure, but average nanostructure probes such as the PDF, become essential complements.

Chapter 2

PDF approaches for quantitative analysis of nanomaterials

2.1 Basics of x-ray scattering

Rigorous descriptions of x-rays and their interaction with matter are provided in texts by Warren [164] and Guinier [48]. For a more contemporary reference we also recommend *Elements of Modern X-ray Physics, 2nd edition* by Als-Nielsen and McMorrow [6] which pays special attention to the development and applications of kinematical scattering theory for non-crystalline materials, or systems with short-range structural order. Finally, for condensed summaries of many key powder diffraction concepts the *International Tables for Crystallography (2019). Vol. H* is an invaluable resource for student crystallographers [44].

We start with the scattering from a single electron and extend to the scattering from an isolated atom with Z electrons. If we consider electrons as classical particles the electron density can be specified as $\rho(\mathbf{r})$ and the field scattered from an atom is a superposition of all contributions from different volume elements within the charge distribution. In the

inset of Fig. 2.1 we illustrate an x-ray with wavevector $\mathbf{k_i}$ impinging on a volume element P inside of an atom located at a distance $\mathbf{r}$ away from an arbitrary origin O. For elastic scattering, where $|\mathbf{k_f}| = |\mathbf{k_i}| = 2\pi/\lambda$, the wave scattered from volume element P, $\mathbf{k_f}$, travels an additional path length of $\overline{AP} + \overline{PB}$ compared to the wave scattered from the origin. This phase difference between the two volume elements illustrated in Fig. 2.1 is simply the dot product of the two vectors $\mathbf{k}$ and $\mathbf{r}$

$$\Delta\phi(\mathbf{r}) = \frac{2\pi}{\lambda}(\overline{AP} + \overline{PB}) \tag{2.1}$$

$$= \mathbf{k_f} \cdot \mathbf{r} - \mathbf{k_i} \cdot \mathbf{r} \tag{2.2}$$

$$= (\mathbf{k_f} - \mathbf{k_i}) \cdot \mathbf{r} \tag{2.3}$$

$$= \mathbf{Q} \cdot \mathbf{r}, \tag{2.4}$$

where we specify that the momentum transfer $\mathbf{Q} = \mathbf{k_f} - \mathbf{k_i}$ and from the geometry shown in Fig. 2.1 it is clear that

$$|\mathbf{Q}| = 2|\mathbf{k}| \sin\theta = \frac{4\pi \sin\theta}{\lambda}. \tag{2.5}$$

For an isolated atom, integrating the contribution of each volume element in the electron density yields the atomic form factor

$$f_0(\mathbf{Q}) = \int_0^\infty \rho(\mathbf{r}) e^{-\imath \mathbf{Q}\cdot\mathbf{r}} \mathrm{d}^3\mathbf{r} \tag{2.6}$$

which can be recognized as the Fourier transform of the distribution of electrons, in this case, within an atom. Although we have illustrated this for a single electron separated by a distance $\mathbf{r}$ from an origin, the idea behind calculating the diffraction pattern of a material in this way is general. That is, we start with the contribution from all electrons in atom, then we *zoom out* to include the contribution from all atoms in an ensemble or motif, and if there is a well defined lattice to arrange the atomic motif, we can readily calculate the scattered

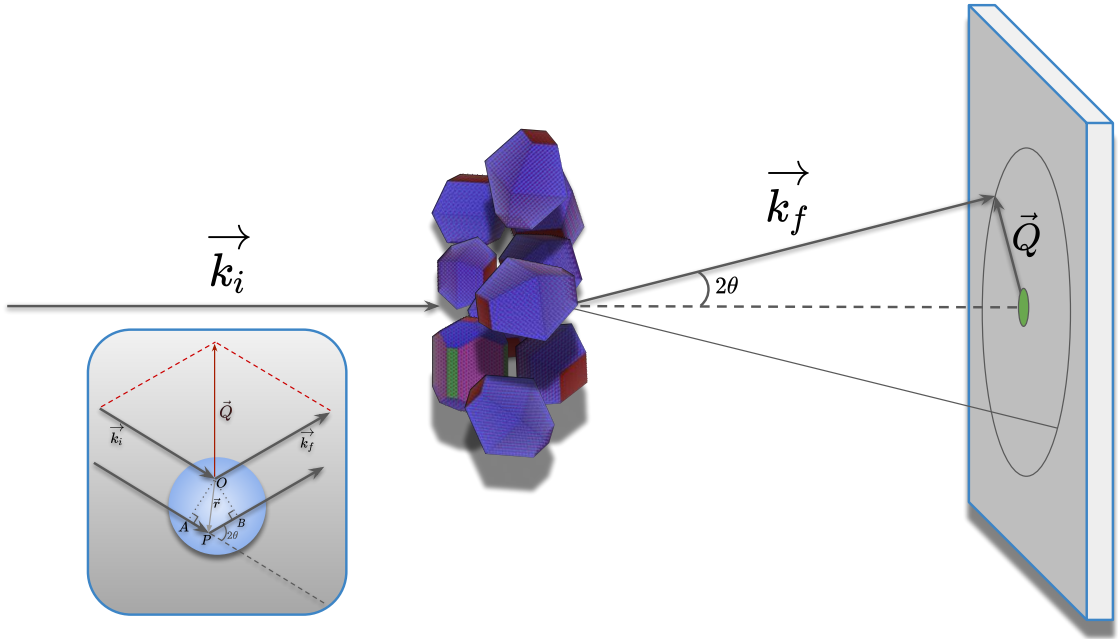

Figure 2.1: Main panel: Illustration of elastic scattering from an isotropic sample of randomly oriented anatase and rutile TiO_2 nanocrystals Inset: Scattering from an atom (see text for details)

intensity from the crystal. What is important to remember is that the scattering amplitude is a function of distances between scattering centers in a material, whether those distances are from a continuous charge distribution in an electron density, or interatomic distances in a molecule, or the symmetry defined tiling of an asymmetric unit in a long-range ordered bulk lattice.

We take these concepts a bit further by comparing the coherent scattering intensity from an arbitrary ensemble of atoms and the crystallographic, or unit cell structure factor, commonly used in the analysis of powder diffraction patterns. Here we start with the scattering amplitude measured from a set of i atoms located at points $\mathbf{r_i}$

$$\Psi(\mathbf{Q}) = \sum_i f_i(Q) e^{-\imath \mathbf{Q}\cdot\mathbf{r_i}} \tag{2.7}$$

where we have replaced the integral for a continuous electron distribution in Eq. 2.6 with a

sum that runs over all interatomic vectors, $\mathbf{r_i}$, from the origin to the i-th atom in the material. The scattering contribution from the electron density within each atom is captured in the Q-dependent atomic form factor term, $f_i(Q)$. The full coherent scattering intensity is then given by

$$I_{coh}(\mathbf{Q}) = |\Psi(\mathbf{Q})|^2 = \Psi(\mathbf{Q})\Psi^*(\mathbf{Q}) \tag{2.8}$$

$$\Psi^*(\mathbf{Q}) = \sum_i f_i^*(Q) e^{\imath \mathbf{Q}\cdot\mathbf{r_i}} \tag{2.9}$$

$$I_{coh}(\mathbf{Q}) = \sum_i \sum_j f_j^* f_i e^{-\imath \mathbf{Q}\cdot(\mathbf{r}_i - \mathbf{r}_j)} \tag{2.10}$$

$$I_{coh}(\mathbf{Q}) = \sum_{i,j} f_j^* f_i e^{-\imath \mathbf{Q}\cdot\mathbf{r}_{ij}} \tag{2.11}$$

$$I_{coh}(\mathbf{Q}) = N\langle f^2\rangle + \sum_{i\neq j} f_j^* f_i e^{-\imath \mathbf{Q}\cdot\mathbf{r}_{ij}} \tag{2.12}$$

where we have dropped the Q-dependence of the atomic form factors for convenience in Eq. 2.10, defined the interatomic distance vector $\mathbf{r}_{ij} = |\mathbf{r}_i - \mathbf{r}_j|$ as the distance between atoms i and j in Eq. 2.11, and removed the self-scattering contribution when $i = j$ and $\mathbf{r}_{ij} = 0$ in Eq. 2.12.

Now if we imagine a perfect crystal, the structure can be described as the convolution of scattering from the unit cell contents (the basis), with the translational symmetry of the periodic long-range ordered lattice. In this case it is not necessary to calculate the scattered intensity by summing over all atoms in the material and instead we can treat the scattering from the unit cell basis separately. This is often called the crystallographic structure factor F_{hkl} and given by

$$F_{hkl} = \sum_{j=1}^{N} f_j \mathrm{e}^{-2\pi\imath(hx_j + ky_j + lz_j)} \tag{2.13}$$

where the sum is only over the atoms in the unit cell, the positions of the j-th atom are x_j, y_j, z_j, f_j is the atomic form factor for the j-th atom, and hkl defines the reciprocal

lattice point at $(h\mathbf{a}^*, k\mathbf{b}^*, l\mathbf{c}^*)$, corresponding to the real space lattice plane given by the Miller indices (hkl). In other words, the scattering observed from a perfect crystal can be described as sharp Bragg peaks located at the reciprocal lattice points, with intensities given by the squared modulus of the unit cell structure factor $|F_{hkl}|^2$. The peak intensities can then be multiplied by Debye-Waller factors and convoluted with an instrumental profile to generate more realistic diffraction patterns. It is clear at this point that $|F_{hkl}|^2$ is no different from the coherent scattering intensity defined in Eq. 2.11, except for the latter, there is no presumption of a symmetry-defined reciprocal lattice or unit cell motif, and the scattering is simply calculated as a function of all interatomic distance vectors in a model. Although methods for structural analysis based on calculating Bragg intensities from crystallographic unit cells and symmetry relationships work well in many cases, for noncrystalline materials such as liquids, molecules, atomic clusters, and small nanoparticles, where the structural coherence between atomic ensembles is very limited, it is often favorable to calculate the scattering intensity with a continuous function of Q, which we describe in the following section.

2.1.1 Orientational averaging and the Debye scattering equation

In a powder of crystals with a small grain size, or a nanopowder, we can typically assume that the orientation of the crystallites in the material is isotropic, and the scattered intensity samples all randomly oriented grains with equal probability. This is illustrated in Fig. 2.1, where a monochromatic x-ray beam is incident on an aggregate of randomly oriented nanocrystals and the scattering is collected on two-dimensional detector behind the sample. Here we can define θ as the angle between $\mathbf{Q}$ and $\mathbf{r}_{ij}$ and Eq. 2.11 becomes

$$I_{coh}(\mathbf{Q}) = \sum_{i,j} f_j^* f_i e^{-\imath Q r_{ij} cos\theta} \tag{2.14}$$

where the vector **Q** reduces to a magnitude since the probability of finding interatomic distance vectors r_{ij} with respect to **Q** is equal in all directions. By taking the spherical integral of the exponential term in Eq. 2.14 we obtain the Debye scattering equation [33],

$$I_{coh}(Q) = \sum_{i,j} f_j^* f_i \frac{\sin(Qr_{ij})}{Qr_{ij}}. \tag{2.15}$$

In a two-dimensional diffraction pattern from an isotropic sample the result of this spherical averaging is that for all interatomic distances r_{ij}, the diffracted rings have constant intensity as a function of azimuthal angle.

2.2 The atomic pair distribution function

We have shown how the coherent scattering amplitude can be described as the Fourier transform of distances between scattering centers in an electron density. Naturally then, a real space correlation function describing the distances between scattering centers, or analogously atoms, with ∼spherical distributions of scatterers about the nucleus, can be obtained by taking the inverse Fourier transform of the diffracted intensities measured from a material, following some normalizations. For a full derivation of the PDF and its relatives see *Underneath the Bragg peaks: structural analysis of complex materials* [37] and *Section 5.7, International Tables for Crystallography (2019). Vol. H* [44]. Here we outline a few key equations in context of the data reduction and transformation steps necessary for producing PDF data.

In a typical total scattering PDF measurement, finely ground bulk powder or nanopowder samples are sealed in, or deposited on, standard sample supports such as polyimide tubes/-tape and carbon paper. Two dimensional diffraction patterns are then collected using the rapid acquisition PDF geometry [28] with hard x-rays in the range of 66.7-86.5 keV using large-area 2D Perkin Elmer detectors. The detector can be placed at various distances or off-

set relative the beam center position in order to tune the angular range and resolution of the measurement. A variety of programs including FIT2D [51], PYFAI [68], and DIOPTAS [134] can then be used to calibrate experimental geometries, mask data, subtract backgrounds, and azimuthally integrate diffraction intensities to 1D diffraction patterns, as shown in the top panel of Fig. 2.2 which shows data for a bulk and nanoparticle sample.

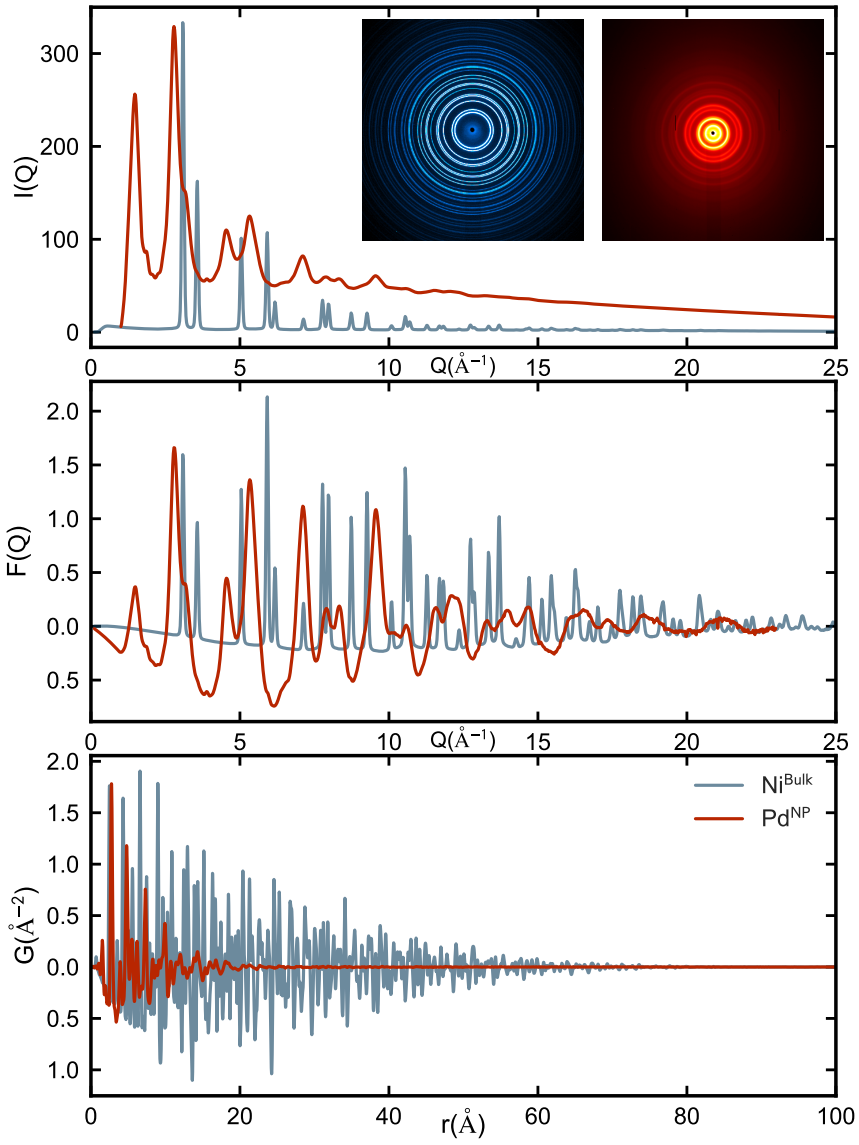

Figure 2.2: Representative integrated and raw intensities (top), $F(Q)$ (middle) and $G(r)$ (bottom) from bulk Ni (blue) and Pd nanoparticles (red).

The coherent scattering intensity $I_{coh}(Q)$ is then divided by the total scattering cross-section of the sample and the self scattering contribution is removed, resulting in the total scattering structure function $S(Q)$

$$S(Q) - 1 = \frac{I_{coh}(Q) - \sum c_i \left| f_i(Q)^2 \right|}{\sum c_i \left| f_i(Q)^2 \right|} \tag{2.16}$$

where c_i and f_i are the concentration and atomic form factor, per atom type i. This is equivalent to normalizing the spherically averaged Debye scattering equation (2.15) by the number of scatterers, N and the average scattering power per atom $\langle f \rangle^2$, yielding

$$S(Q) - 1 = \frac{1}{N\langle f \rangle^2} \sum_{i \neq j} f_j^* f_i \frac{\sin\left(Qr_{ij}\right)}{Qr_{ij}}. \tag{2.17}$$

To take the inverse Fourier transform of the total scattering structure function $S(Q)$ we need the correct Fourier kernel which connects the reciprocal space scattering to the real space pair correlation function, which we define as the reduced total scattering structure function, $F(Q) = Q[S(Q) - 1]$. Because the scattering cross section becomes very small at high-Q, an important result of the normalization to the raw scattered intensities, $I(Q)$ is that the high angle data are significantly amplified in the normalized structure functions, which is almost always neglected or removed in traditional Bragg difraction analysis. This can be seen by comparing the top and middle panels in Fig. 2.2 where we have plotted the $I(Q)$ and $F(Q)$ data over the same Q-range. While the raw diffraction patterns for both the bulk and nanoparticle samples appear to have almost no distinguishable peaks beyond $\sim$15 Å^{-1}, the $F(Q)$ contains well resolved, high amplitude peaks extending to a Q_{max} near 25 Å^{-1}. Finally to obtain the atomic pair distribution function $G(r)$, we can take inverse Fourier transform of the reduced total scattering structure function $F(Q)$, including both Bragg and diffuse components, and since $F(Q)$ is an odd function, the Fourier transform can be simplified to a sine Fourier transform as

$$G(r) = \frac{2}{\pi} \int_{Q_{\min}}^{Q_{\max}} Q[S(Q) - 1] \sin(Qr) dQ. \tag{2.18}$$

The range of data used in the Fourier transform (Q_{min} to Q_{max}) is tuned depending on the sample to give the best trade-off between statistical noise and real-space resolution, and in some cases, to truncate low-Q scattering unambiguously originating from organic species in the sample which are not intended to be part of a structural model.

2.2.1 Some practical considerations

Two important data processing and normalization steps that differentiate total scattering experiments from conventional powder diffraction are 1) the background intensity is removed by obtaining an independent measurement of the sample holder, instead of commonly used polynomial approximations which are prone to remove diffuse scattering and 2) a much wider Q-range is included with an increased weighting applied to the high-Q information. A consequence of the latter is that the high-Q signal is weak and one must take care to ensure that good statistics are obtained in this Q-range in $F(Q)$ by optimizing the total image acquisition time, background subtraction scale, and carefully masking all detector artifacts, dead pixels, hot pixels, and other aberrations which can lead to undesired high-Q intensities, typically with amplitudes significantly higher than the real material signal.

Take for example a more challenging case of amorphous Boron nanoparticles where the scattering from the sample is exceptionally weak. In Fig. 2.3(b) we can see how the integrated intensity from the nanoparticles (blue) is barely distinguishable from the scattering from the kapton sample holder (red). In principle, if the images are collected with the same exposure time (inverse frame rate), and the total counts per pixel are normalized by the total exposure or total number of frames collected, the ratio between the background and sample scale should be 1:1. For a number of reasons this is not always the case, and the optimal background is not known *a priori*. This situation makes background subtraction challenging, especially for weakly scattering samples, because small differences in the background scaling

can lead to significant changes in the subtracted pattern, and subsequently the PDF. One way of handling this which is viable when a structure model, or series of candidate structure models are available against which the PDF data can be tested, is to apply a continuous range of background scalings during the subtraction step. The transformed PDFs, each obtained with a different background scale, can then be iteratively refined against a set of candidate models, to determine an optimal background scaling for which the agreement between the measured and calculated PDFs is best. This was the procedure used in Fig. 2.3(c) which shows well resolved signal from the local ordering in the amorphous nanoparticles after optimizing the background subtraction. Another option is to identify specific correlations in the PDF which should or should not exist, and to tune the background scale until the amplitude of the correlation is maximized or minimized. Both of these routines are manual, time consuming, and conditioned based on expected outcomes. Work is underway to develop more robust tools for automated background subtraction, but this remains a fairly sizable hurdle in PDF analysis of weakly scattering materials, and time series reactions which track the formation of atomic nuclei and precipitates from precursor solutions *in situ*.

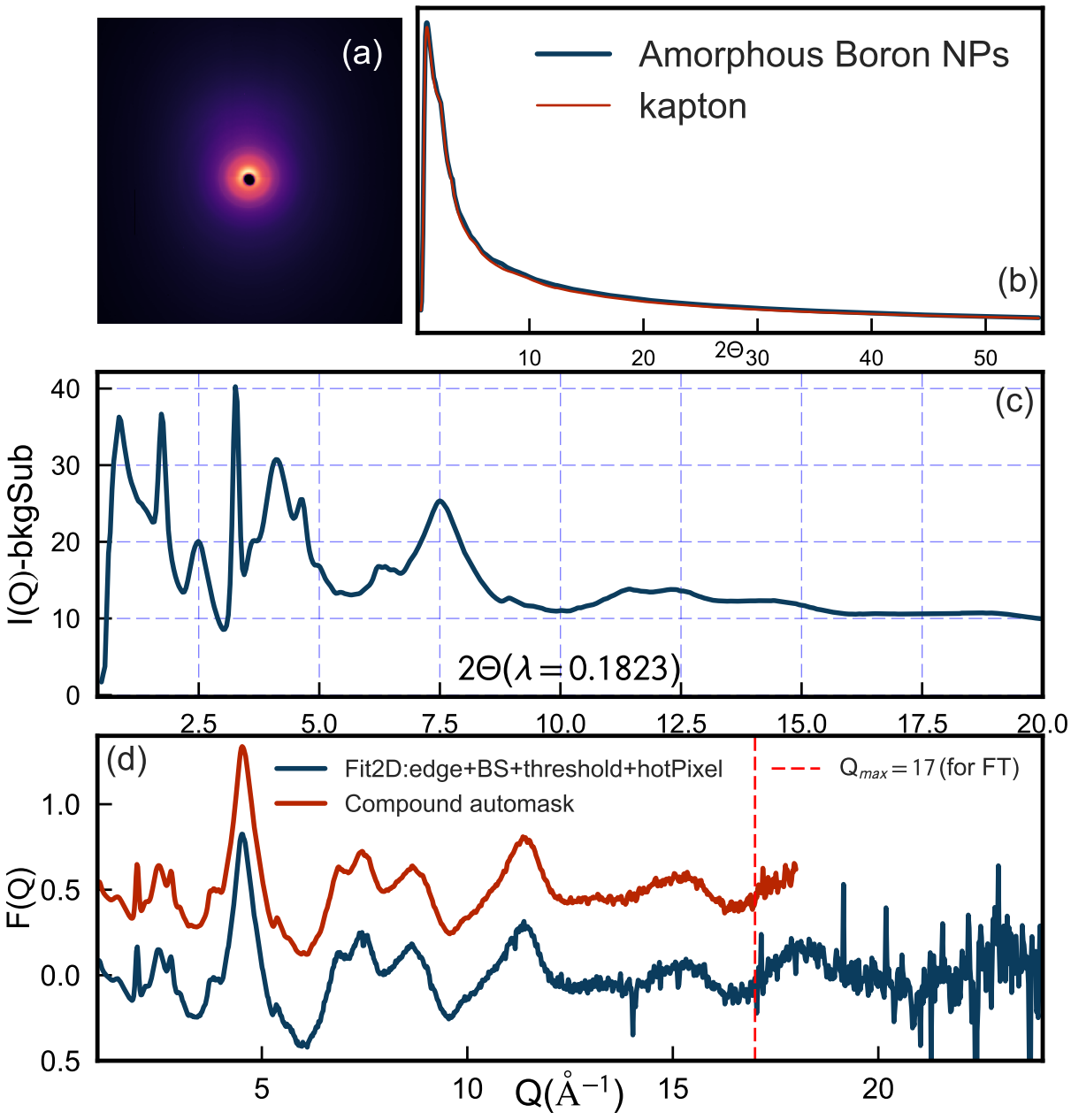

Figure 2.3: (a) 2D diffraction image of amorphous Boron nanoparticles (b) Azimuthally integrated $I(Q)$ for sample (blue) and background (red) (c) Optimized background subtracted $I(Q)$ (d) Comparison between different masking routines and their effects on $F(Q)$

Fig. 2.3(d) also illustrates another challenge with data processing which is the accurate

masking of data from area detectors. Here, careful manual masking did not adequately remove spurious signals in $F(Q)$ and the data became very noisy even below a Q_{max} of 15 Å^{-1} (blue). However, an automated masking protocol [166] used to remove outlier pixels at the image level, resulted in considerably cleaner high-Q data (red).

A final point on data reduction which is relevant to the study of noble metallic nanoparticles discussed in Chapter 3 and 4 of this thesis, is the selection of Q_{min} used in the transformation of $F(Q)$ to $G(r)$ (Eq. 2.18). In any PDF measurement there is an absolute lower limit of Q_{min} determined by the position and size of the beamstop used to prevent scattering from the direct beam. This incorrectly removed signal from the scattering in the low angle range leads to a modification of the PDF baseline, on top of negative sloping sloping baseline related to the average atomic density of the sample. For bulk materials this is negligible, and typically we use either the default Q_{min} value of 0.1 Å^{-1}, or set Q_{min} to a value aligned with a sharp cutoff in $I(Q)$ corresponding to the beamstop mask. In functionalized nanoparticles however, there is often significant correlation peaks in the low angle region from organic species in the sample. If we are only considering the structure of the metallic core and not including secondary ligand phases in the modeling, we found that it is appropriate to increase Q_{min} to a value that removes the low-Q correlation peaks that can be unambiguously attributed to the organic species.

An example of this is shown in Fig. 2.4, where in the top left panel we plot $I(Q)$ from small palladium nanoparticles with differing Q_{min} truncations, and their corresponding PDFs in the bottom left panel. The Q-range over which the signal originates from organic species is highlighted with red dashed lines. Very subtle modifications are observed to the PDF baseline for different Q_{min} values. However, if the low angle scattering is removed in this way, one must take care in how the PDF from the structural model is calculated as it can have rather large effects on the goodness of fit. In the right panel of Fig. 2.4 we've plotted the

R_w dependence of a discrete fcc sphere fit to the measured data from small Pd nanoparticles with a fixed experimental $Q_{min} = 2.0$. Ultimately it was found that applying a Q_{min} value equal to the experimental Q_{min} yielded the best fit, seen as a sharp minimum in the right panel of Fig. 2.4, but it is still unclear why other fine features in the R_w dependence appear as a function of the calculated Q_{min}, or whether this heuristic can be used for all samples.

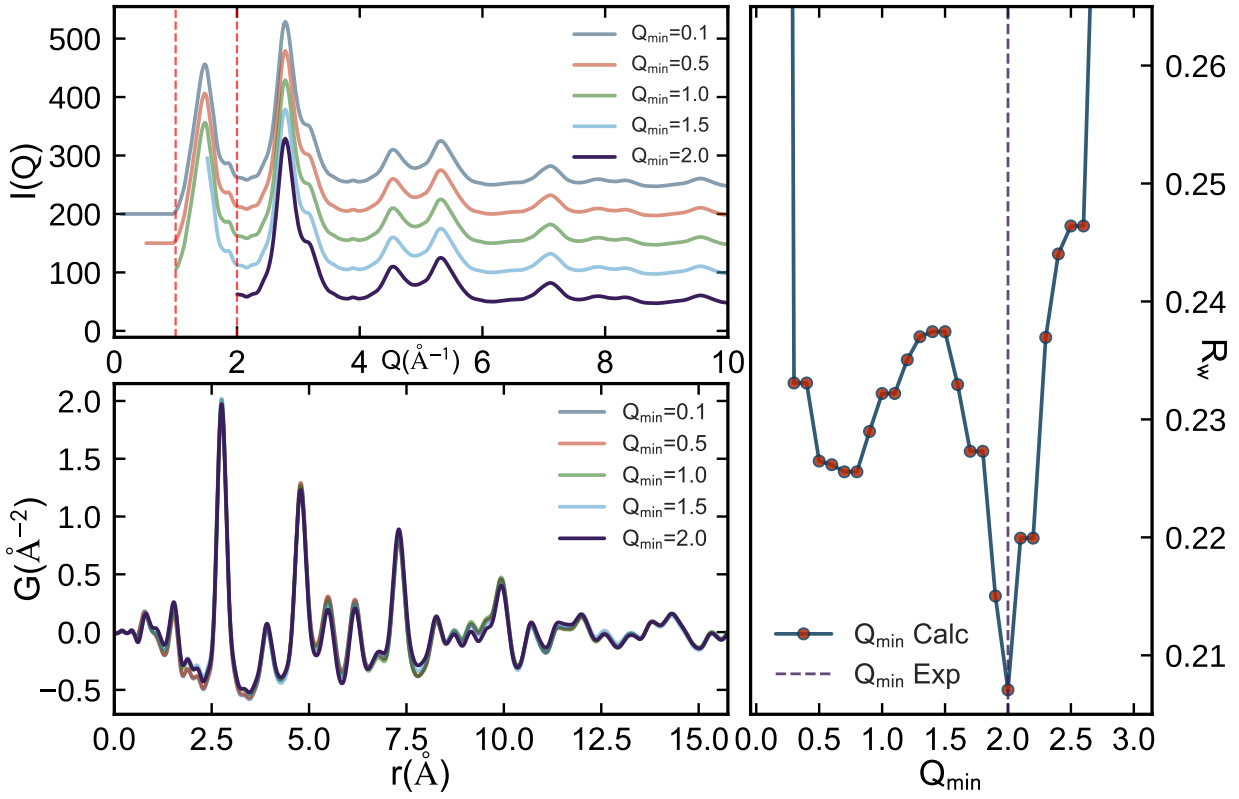

Figure 2.4: Left panels: Experimental I(Q) following background subtraction for Pd nanoparticles where the extent of the small angle scattering is truncated with different values of Q_{min} (top) and their corresponding PDFs after transformation (bottom). Right panel: R_w dependence of a discrete fcc sphere fit to the measured data from small Pd nanoparticles with a fixed experimental $Q_{min} = 2.0$. See text for additional details.

2.2.2 Calculating the PDF in real-space as attenuated bulk crystals

The PDF is an intuitive, structurally determined function which gives the scaled probability of finding two atoms in a material a distance r apart, or in other words, a histogram of interatomic distances. Given a structure model, the PDF can be calculated according to

$$G(r) = 4\pi r\rho(r) - 4\pi r\rho_0\gamma_0(r), \tag{2.19}$$

$$\rho(r) = \frac{1}{4\pi r^2 N}\sum_i\sum_{j\neq i}\frac{b_i b_j}{(b)^2}\delta(r - r_{ij}). \tag{2.20}$$

where ρ_0 is the atomic number density of the material, and $\rho(r)$ is the atomic pair density, or the mean weighted density of neighbor atoms at distance r from an atom at the origin. The sums in $\rho(r)$ run over all atoms (N) in a crystallographic unit cell, and periodic boundary conditions are applied according to the symmetry of the lattice. Atomic vibrations and static disorder lead to peak broadening in the PDF, and the delta functions in Eq. 2.20 are convoluted with Gaussians, $\exp\left(-(r - r_{ij})^2/\sigma_{ij}^2\right)$ where σ_{ij} is parameterized as

$$\sigma_{ij} = \sigma'_{ij}\sqrt{1 - \frac{\delta_1}{r_{ij}} - \frac{\delta_2}{r_{ij}^2} - Q_{broad}^2 r_{ij}^2}. \tag{2.21}$$

Here, σ'_{ij} is the the peak width without correlation, computed from the components of the tensor describing the atomic displacement parameters (ADP), δ_1 and δ_2 are linear and quadratic corrections for correlated motion effects [135], and Q_{broad} is an *ad-hoc* parameter for Q-dependent instrumental broadening in reciprocal space ($\Delta Q/Q$), which leads to linearly increasing peak widths in the PDF. An additional instrumental parameter, Q_{damp} is a measure of the standard deviation for a Gaussian envelope which dampens the full calculated PDF and serves as an approximation for finite, Guassian peak widths in reciprocal space. In practice, it is important to independently calibrate the instrumental parameters with a bulk material where the structure is well known and keep these fixed in any subsequent analysis

of a material where the extracted structural parameters are to be interpreted independent of instrumental effects.

In order to quantify the agreement between a calculated and experimental PDF, the parameters, p_i, describing a model are varied via least-squares refinement, until the difference between G_{calc} and G_{exp} minimized, where the goodness-of-fit can be quantified as

$$R_w(p_1, p_2, \ldots) = \sqrt{\frac{\sum_n [G_{exp}(r_n - G_{calc}(r_n))]^2}{\sum_n G_{exp}^2(r_n)}}. \tag{2.22}$$

A variety of programs are available for calculating PDFs and extracting structural information [136, 158, 29] but PDFGUI [39] and the CMI [65] python framework under DIFFPY are our favorites.

The $\gamma_0(r)$ term in Eq. 2.19 is a characteristic function which encodes the size and shape of a crystallite, also called the nanoparticle form factor. We refer to the application of characteristic (envelope) functions to PDFs calculated from crystallographic unit cells with periodic boundary conditions, as the attenuated crystal (AC) approximation. In a nanocrystal, the probability of finding correlations in the PDF decays to zero as a function of r when there are no interatomic distances beyond the maximum dimensions of the crystallite. Here, crystallite refers to the size of the domain of coherent scattering in a material. This should not be used interchangeably with the nanoparticle size, but in some cases when the atomic structure of a nanocrystal is monocrystalline, without domains, and with well ordered surfaces, the crystallite size extracted from PDF using a characteristic shape function can be in good agreement with particle size estimates from other methods. In PDFGUI this is implemented as a spherical shape function which can be used to find the maximum extent in r where signal can be differentiated from noise. This can be the diameter of a coherent spherical domain in a particle, or more generally, a measure of the structural of any given structural phase in a refinement. A variety of other characteristic functions for particle morphologies

are available in DIFFPY-CMI, along with characteristic functions for different particle size distributions which, like shape functions, affect the profile of the PDF envelope.

In Fig. 2.5 we show a specific case of different characteristic functions applied to PDF data from pure anatase TiO_2 nanocrystals.

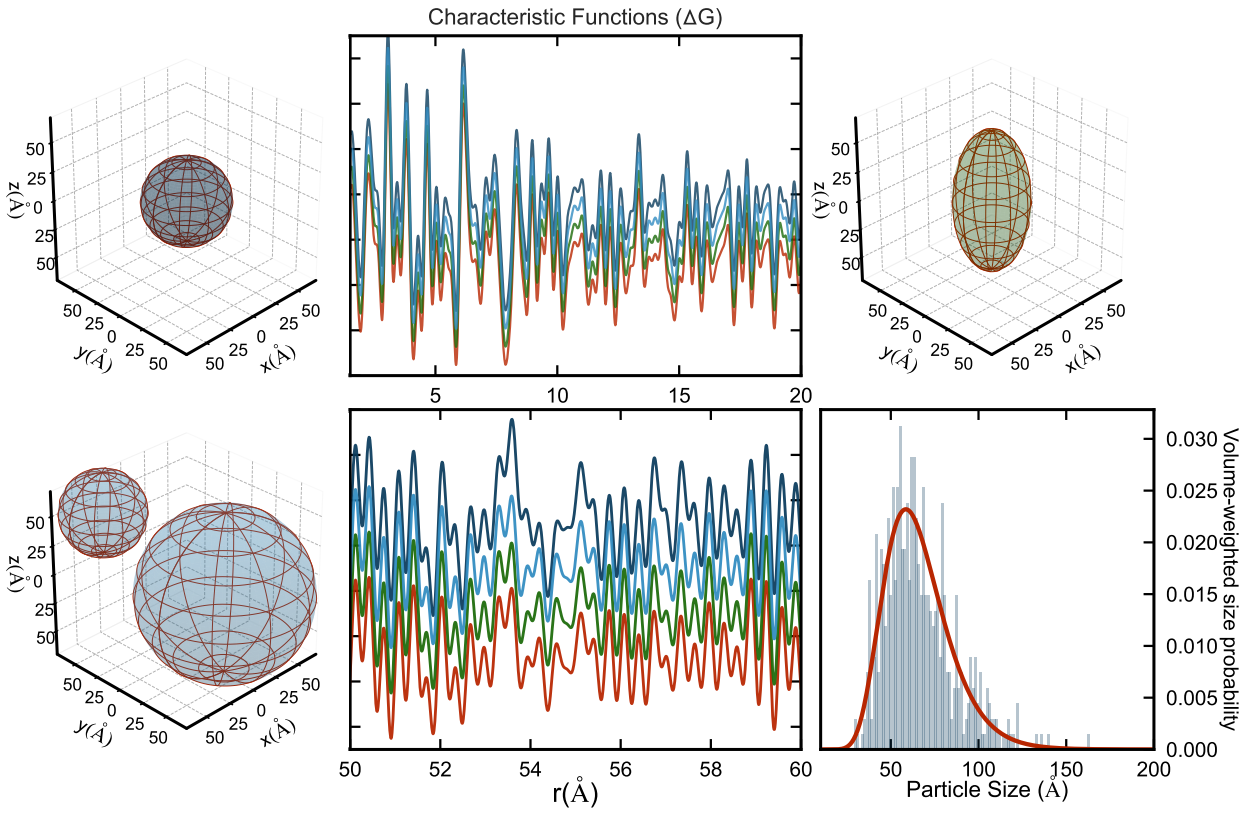

Figure 2.5: Refined dimensions and parameters of different characteristic shape and distribution functions for anatase nanoparticles and their effects on fit residuals ΔG. See text for details.

This included the standard PDFGUI AC approximation with a single average spherical particle size (top left), a model with two different populations of anatase particles with independent scale factors (bottom left), a shape function for a prolate or ellipsoidal morphology (top right), and finally a log normal particle size distribution. In most cases the refinements

resulted in plausible values for the structural parameters extracted from the characteristic functions after refinement, but what became apparent was that there was very minimal sensitivity in terms of differentiating between the scenarios from the PDF alone. This can be seen visually by inspecting the fit residuals from each model and in the middle panels of Fig. 2.5 where it is clear that the signals in the difference curves (ΔG) are almost identical, both at low and high-r. In short, caution should be exercised to ensure results are unique when using characteristic functions to quantify morphological parameters and size distributions from total scattering data. Shape functions and size distributions can also be determined directly from small angle scattering (SAXS) data, and estimated from electron microscopy. When these methods are used along with PDF analysis, the results are typically much more reliable.

2.2.3 Calculating the PDF as the Fourier transform of the Debye equation

In a growing number of nanoparticle systems it is becoming clear that the attenuated crystal (AC) approximation only gets us so far in terms of building a realistic picture of the internal atomic structure of these materials. Atomistic or discrete structures which contain well defined domain arrangements, precise surface terminations, spatially inhomogeneous atomic displacements, etc. often cannot be reproduced with periodic crystal models, but they can be built rather easily using a few software packages [77, 136]. In these cases it is better to calculate the PDF, directly from the atomic coordinates, as the Fourier transform of the properly normalized Debye scattering equation (DSE) given in Eq. 2.17, which is modified below with a multiplicative exponential term that includes Debye-Waller effects,

$$F(Q) = \frac{1}{N\langle f\rangle^2} \sum_{i \neq j} f_j^* f_i \left(e^{-\frac{1}{2}\sigma_{ij}^2 Q^2} \right) \frac{\sin\left(Q r_{ij}\right)}{r_{ij}} \tag{2.23}$$

where σ_{ij}^2 is the correlated broadening factor for the atom pair and $r_{ij} = |\mathbf{r}_i - \mathbf{r}_j|$ is the distance between atoms i and j given in a list of cartesian coordinates. Note that this term does not influence peak widths in $F(Q)$, but instead describes how peak intensities diminish as a function of Q. PDFs calculated from discrete models do not require any symmetry constraints or attenuation with shape functions because the complete histogram of distances is generated explicitly by the list of atomic coordinates. In a typical PDF refinement using the DSE, implemented in DIFFPY's DEBYEPDFGENERATOR class under SRFIT, the atomic coordinates in space are held constant and only four parameters are allowed to vary and obtain good agreement between the calculated and measured PDFs: an expansion coefficient to account for differences in nearest neighbor distances, an isotropic atomic displacement parameter (U_{iso}) per element, a global scale factor, and a parameter for correlated motion effects (δ_1 or δ_2). The drawback is that larger models with more atoms become computationally expensive.

2.3 Model independent analysis of nanoparticle PDF data

As a final point in this chapter, I would like to advocate the importance of interpreting PDF data without structural models, and interrogating fit residuals from simple highly constrained refinements. One of the simplest, but most powerful ways of understanding structural differences between two materials, or a material measured under different conditions, or the structure of a material over different length scales, is to quantify the similarity between two PDF curves. An excellent tool for accomplishing this is the Pearson correlation coefficient

which gives the linear correlation between two spectra, and is calculated as

$$P = \frac{1}{n-1}\sum_{i=0}^{n}(\frac{X_i - \bar{X}}{\sigma_x})(\frac{Y_i - \bar{Y}}{\sigma_y}), \tag{2.24}$$

where $\bar{X}$ and σ_x are the mean and standard deviations of datasets, respectively. The calculated pearson coefficient P gives a value between -1 and 1, where -1 implies anti-correlation, 0 implies no correlation, and 1 implies complete correlation [36].

In Fig. 2.6 and Fig. 2.7 we provide two basic examples of how correlation analysis can be used. In Fig. 2.6 we were interested in understanding how different a series of eleven Ag_xAu_{1-x} alloyed nanoparticles were from one another. To do this, we generated a pearson

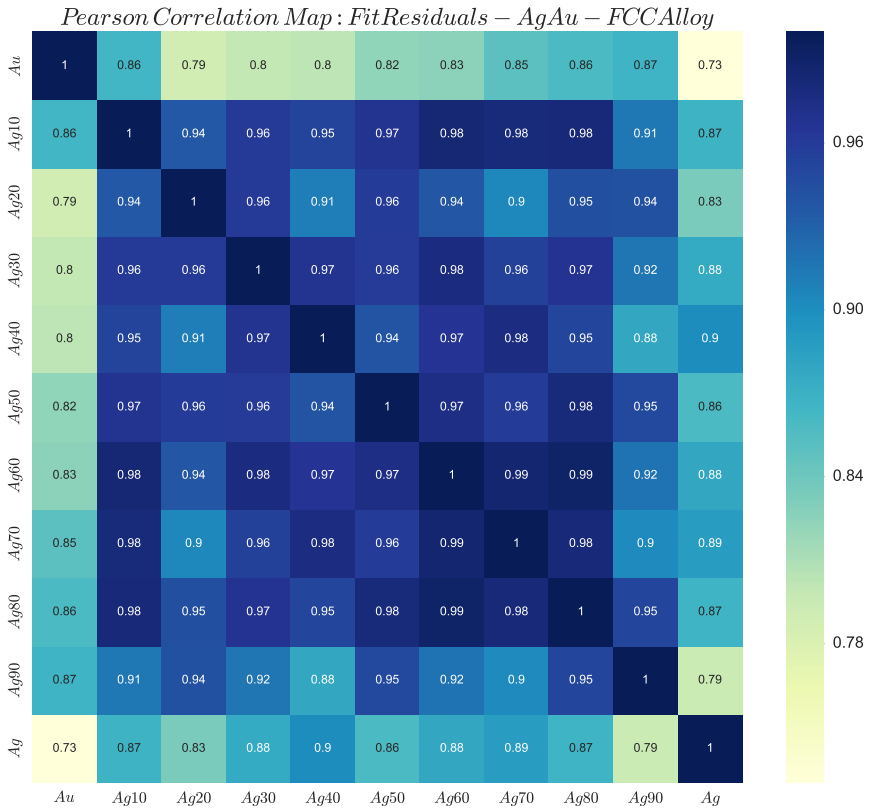

Figure 2.6: Pearson cross-correlation map for a series of 11 PDFs from an Ag_xAu_{1-x} nanoparticle alloy series

correlation map which describes the similarity between each PDF dataset, vs all 11 alloys

in the series. The map is symmetric about the diagonal, and the somewhat banal result here was that the majority of the alloys were highly similar to one another, with correlation coefficients greater than 0.9. The only exception was pure Ag, which painted a perimeter of smaller correlation values around the map. Although the result seems boring, it helped us understand the limitations in terms of differentiating the Au rich alloys, that might be assessed with more time consuming modeling.

A final example is shown in Fig. 2.7, where a well defined structured residual appeared after fitting PDF data from silicon nanoparticles hyperdoped with boron with an attenuated crystal diamond cubic structure model. One hypothesis was the local correlations in the difference curve emerged due to a secondary boron-rich impurity phase which grew on the surface of the particles. We thus screened candidate structure models from a variety of secondary phases such as boric acids, boron oxides, and elemental boron allotropes (with boric acid models shown in Fig. 2.7) by calculating PDFs from the structure models and determining the similarity to the residual itself. Because these structures were typically low symmetry with many refinable parameters, and multi-phase fits with trace impurities can become unstable, this method simply helped us understand quickly whether any of these candidate secondary phases might be promising or not. In this case, none of the models were similar enough to the misfit features to warrant further investigation, and were ruled out with reasonable confidence.

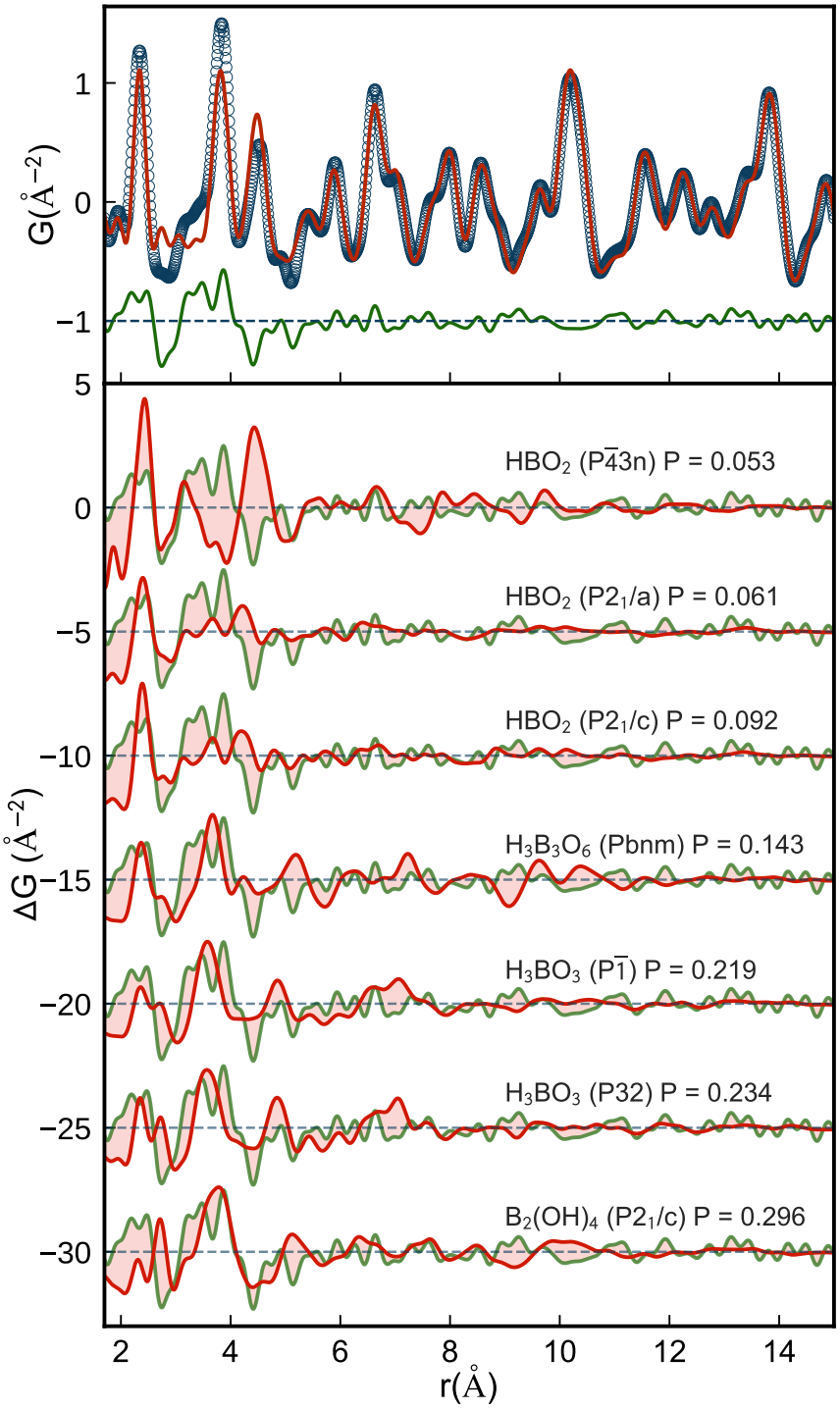

Figure 2.7: Structural misfit for most heavily boron doped sample (top panel) and screening via pearson correlation coefficients for calculated PDFs from candidate boric acid structure models.

Chapter 3

Improved metallic nanoparticle core structures from PDF data

It is possible to get information-rich PDFs of many different metallic nanomaterials, from $\sim$ 1 nm atomically precise clusters to nanocrystals with different sizes and morphologies, synthesized under different conditions, prepared with or without surfactants, and measured down to low concentrations within industry-relevant sample environments and supports. Quantitative information may be extracted from these PDFs using modelling. The simplest, but still very powerful approach to modelling nanoparticles is based on a attenuated crystal (AC) approximation. AC models are built by applying crystallographic symmetry and periodic boundary conditions to a small unit cell. Nanocrystals are finite sized, and this is accounted for by attenuating the calculated PDFs with shape functions that encode the nanoparticle morphology. The most widely used software for this kind of analysis is PDFgui [39]. AC modelling of nanoparticles using highly constrained refinements in PDFgui is simple, rapid, and less susceptible to over-fitting. The ability to independently refine local, intermediate, and long-range structure, simply by specifying an interatomic range, is also

an intuitive means of understanding structure and heterogeneity originating from different length-scales. The PDFGUI approach has been used to characterize critically important structural properties of nanoparticles such as stacking faults [100, 170], strain [43], size [151], shape [40, 69], segregation [4], and broken symmetries [152, 120].

An often overlooked benefit of calculating PDFs from simple AC models and refining them with a few parameters to high resolution experimental PDFs is that fit residuals become a critical part of data analysis, and give a trustworthy measure of how well the AC model alone can describe the data. Sinusoidal oscillations observed in PDF fit residuals from AC refinements of nanoparticles have been used to identify solvent restructuring in ZnO NPs [174] and the size-dependent emergence of amorphous-like scattering in nickel NPs, closely resembling the scattering from bulk metallic glasses [35]. Previous studies have also used finite cluster models to compute PDFs for comparison with nanoparticle PDF data where AC approximations were deemed insufficient. [63, 127, 171, 119, 17, 59, 111] In this paper, we isolate and compare seemingly benign, but in fact highly structured residuals that can be extracted reproducibly from nanostructured noble metals after fitting them to close packed AC models. We show that these may be explained by simple discrete but rational cluster structure models. We argue that any more complicated models such as highly defected [88, 18], multi-phase [23, 24] and heterogeneous core-shell models [125, 167, 130, 129, 102, 133, 128] should only be attempted to explain signal in the PDF difference curve that is not captured by the finite clusters described here, and ideally, they should be supported by complementary measurements using atomically precise local structure probes capable of identifying domain structures and disclinations inside small metallic nanoparticles.

3.1 Methods

3.1.1 Pair distribution function measurements

Total scattering measurements were performed at four synchrotron x-ray facilities and five beamlines NSLS-I (X17A), NSLS-II (XPD, PDF), ESRF (ID11), and APS (11-ID-B) across various beamtimes with hard x-rays in the range of 66.7-86.5 keV. Nanocrystals were loaded in, or deposited on, standard sample supports such as polyimide tubes/tape and carbon paper. Experimental conditions differed slightly between measurements, but all diffraction patterns were collected in a wide-angle transmission geometry with area detectors placed in close proximity to the sample. Sample information is given in Table 3.1 and measurement/PDF specific details are provided in Table 3.3 (Section 3.5).

Fit2D [51], pyFAI [68], or Dioptas [134] was used to calibrate experimental geometries and azimuthally integrate diffraction intensities to 1D diffraction patterns. Standardized corrections are then made to the data to obtain the total scattering structure function $F(Q)$, which is then sine Fourier transformed to the PDF using PDFgetX3 [64] and xPDFsuite [169].

Transmission electron microscopy (TEM) images were collected on a JEOL JEM-1400 microscope operating at 120 kV. HRTEM images were collected on a JEOL F200 scanning/-transmission electron microscope operating at 200 kV.

3.1.2 Modelling

AC modelling for samples listed in Table 3.1 was carried out in PDFgui using a close-packed fcc ($Fm\bar{3}m$) model. An isotropic gaussian atomic displacement parameter (ADP), cubic lattice constant (a), global scale, and δ_2, a parameter for correlated motion effects [135], were refined. Parameters that describe the resolution of the measurement (Q_{damp}, Q_{broad}) were

obtained by independently refining a bulk calibrant measured in the same geometry as the nanocrystalline sample. The experimental PDFs were fit over a wide r-range, $1.5 < r < 70$ Å, with an additional spherical shape function that damps PDF peak intensities with increasing r due to the finite size or structural coherence of the nanoparticle crystallites [37].

Discrete structure refinements were done within the CMI software framework [65]. The PDFs are calculated from discrete models expressed in cartesian coordinates using the Debye scattering equation [33], implemented in DIFFPY's DEBYEPDFGENERATOR class under SRFIT. The atomic coordinates in space were held constant in the refinements but four parameters were allowed to vary and obtain good agreement between the calculated and measured PDFs: an isotropic expansion coefficient (linear scaling in r) to account for differences in nearest neighbor distances, U_{iso} (isotropic ADPs), a single scale factor, and δ_2. PDF refinements were carried out over the range $1.5 < r < 20$ Å. Discrete models were built using the Python atomic simulation environment ASE [77], including twinned structure motifs formalized by Mackay [92] and Bagley [10]. Details are provided in Section 1.6, including instructions needed to reproduce all core cluster models tested in this study.

3.2 Results

X-ray PDFs were measured for a set of noble metallic nanocrystals, listed in Table 3.1. The data collection, analysis and modelling are described in the Methods section. We first compare fits of an fcc AC model to a representative nanoparticle dataset, Pd (Pd^P in Table 3.1). The results are shown in Fig. 3.1(b). For comparison, in Fig. 3.1(a) we show a fit to a well-ordered crystalline material, bulk nickel. The fit is excellent as evidenced by the low agreement factor, $R_w = 0.019$, and the very small fluctuations in the difference curve. The fit to the ∼3 nm nanoparticle sample is also quite good, with an $R_w = 0.253$ that is

Table 3.1: Metallic nanocrystalline samples used in this study. D-est.: Initial estimate of the particle or wire diameter from non-crystallographic methods, Surfact: Surfactant, Morph: particle morphology. Morphologies are nanoparticle (P), nanowire (W), nanocluster (Cl), bulk (B). C indicates the sample was on a carbon support. Primary capping agents are specified in the surfactant column, OAm: Oleylamine, TOP: Trioctylphosphine, PVP: Polyvinylpyrrolidone, ODA: Octadecylamine, PFSA: Perfluorosulfonic acid, p-MBA: *para*-Mercaptobenzoic Acid, SC6: Hexanethiol. For more information on sample preparation and characterization using TEM please see the Synthesis Methods section in Section 3.4.

Name	Composition	D-est. (nm)	Surfact.	Beamline	Morph.
Pd^{P}	Pd	3.0 [a]	OAm	XPD	P
$CoPd^{P}$	$Co_{0.2}Pd_{0.8}$	8.6 [a]	OAm, TOP	XPD	P
$PdNi^{W}$	$Pd_{0.83}Ni_{0.17}$	2.3 [a]	ODA	X17A	W
Ag^{P}	Ag	38.0 [b]	PVP	XPD	P
$AgAu^{P}$	$Ag_{0.5}Au_{0.5}$	5.0 [b]	PVP	PDF	P
$PdAu^{W}$	$Pd_{0.9}Au_{0.1}$	2.1 [a]	ODA	X17A	W
Pd^{W}	Pd	2.0 [a]	ODA	X17A	W
Au^{P}	Au	9.0 [b]	PVP	XPD	P
$PtRu^{P,C}$	$Pt_{0.5}Ru_{0.5}$	3.5 [a]	PFSA	XPD	P,C
Pt^{P}	Pt	3.0 [a]	OAm, TOP	XPD	P
Au^{Cl1}	Au	1-2	p-MBA	ID11	Cl1
Au^{Cl2}	Au	1-2	SC6	11IDB	Cl2
Ni^{B}	Ni	Bulk	None	XPD	B

[a] Estimated average size by transmission electron microscopy (TEM)

[b] Estimated average size by differential centrifugal sedimentation (DCS)

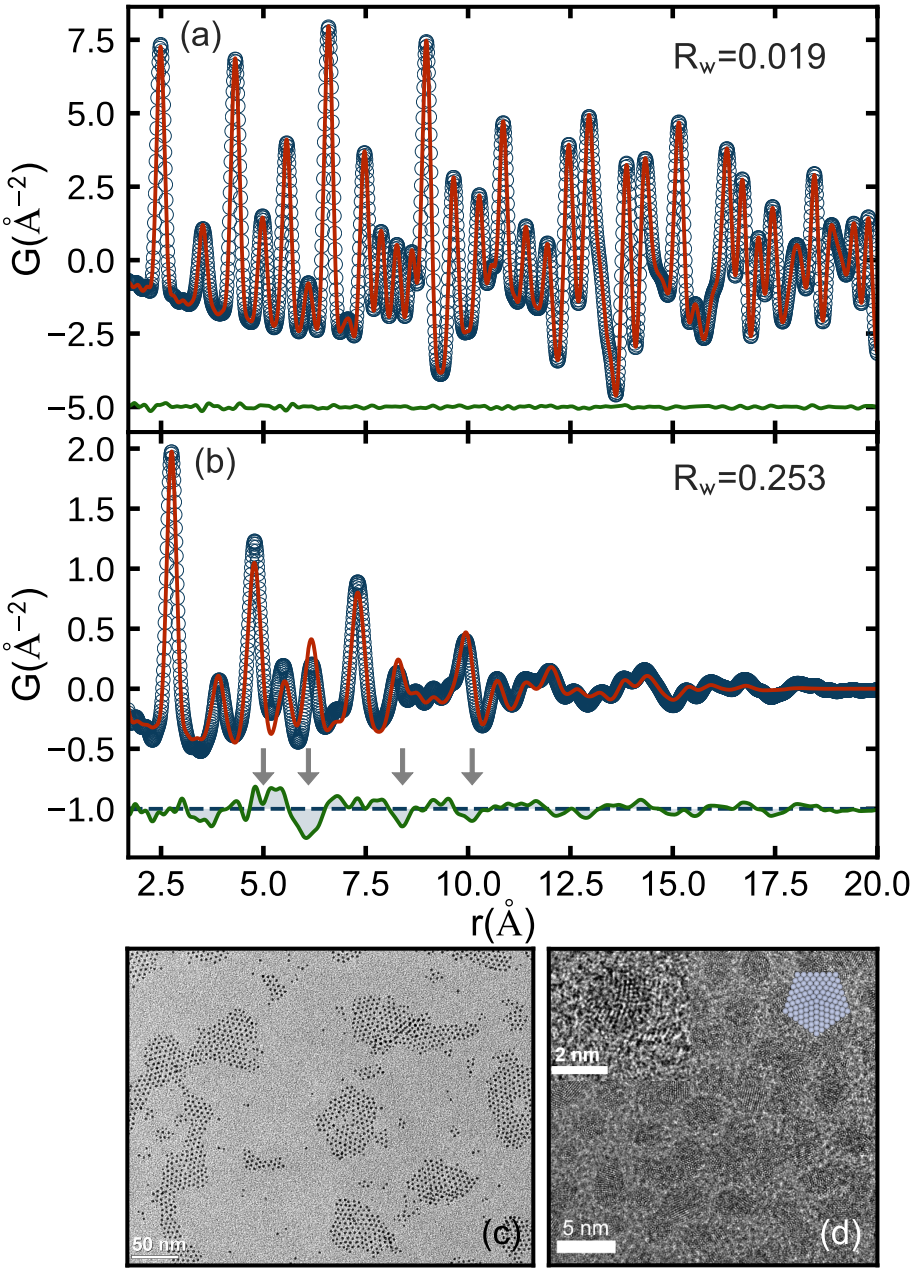

Figure 3.1: Measured (open circles) and calculated (red solid lines) PDFs with difference curves shown offset below (green) for (a) bulk nickel and (b) ∼3 nm diameter palladium (Pd) nanoparticles (NPs). Bottom row: (c) transmission electron microscopy (TEM) image of ∼3 nm Pd NPs (d) high-resolution TEM image of several ∼3 nm Pd NPs with an isolated particle shown in the inset, alongside a candidate discrete cluster model to the right. Images were obtained from the sample corresponding to the measured PDF shown in (b).

generally considered an acceptable fit of fcc models to PDFs of nanoparticle data in the literature [123, 100, 4, 126, 119, 113, 75, 41, 132, 42, 167]. The calculated and measured peaks line up well, suggesting the structural model captures a majority of the PDF signal. However, the nanoparticle fit is worse than the fit of the crystalline material, with an R_w thirteen times larger, and the difference curve contains well-resolved, structured features, for example, around 5, 6, 8.5, and 10 Å highlighted with arrows in the figure.

If we assume that this signature in the difference curve is coming from a well defined structural motif in the nanoparticle that is not captured in the AC modelling, we would like to know how ubiquitous this deviation from the fcc structure is. To do this we look at the difference curves between best-fit fcc AC models and the wide array of nanocrystalline samples listed in Table 3.1. If the difference curves are similar, it indicates that the materials surveyed share a common underlying structural modification, whereas if they are not similar, it will indicate more than one modification type, or even non-transferable structural relaxations might exist that depend on nanocrystal composition, size, dispersity, ligand coverage, or other factors. The results are shown in Fig. 3.2. Each curve in this plot is a difference curve, like the one shown offset below the Pd nanoparticle data in Fig. 3.1(b), but here they are the differences between the best-fit fcc AC models and the data from the different samples in Table 3.1. We immediately see a high degree of similarity, at least among the top 7 curves in the plot. There are some similarities, but the agreement is less clear for the curves below this. However, the most striking result is that multiple samples, made from different materials with different morphologies, as disparate as 40 nm particles and 2 nm wires, result in highly similar difference curves when fit with fcc AC nanoparticle models. In addition, we note that this characteristic difference curve is apparent in other studies in the literature [74, 147, 151, 35, 132]. This strongly suggests that a variety of noble metallic nanomaterials share a common structural modification. We next turn to investigating the

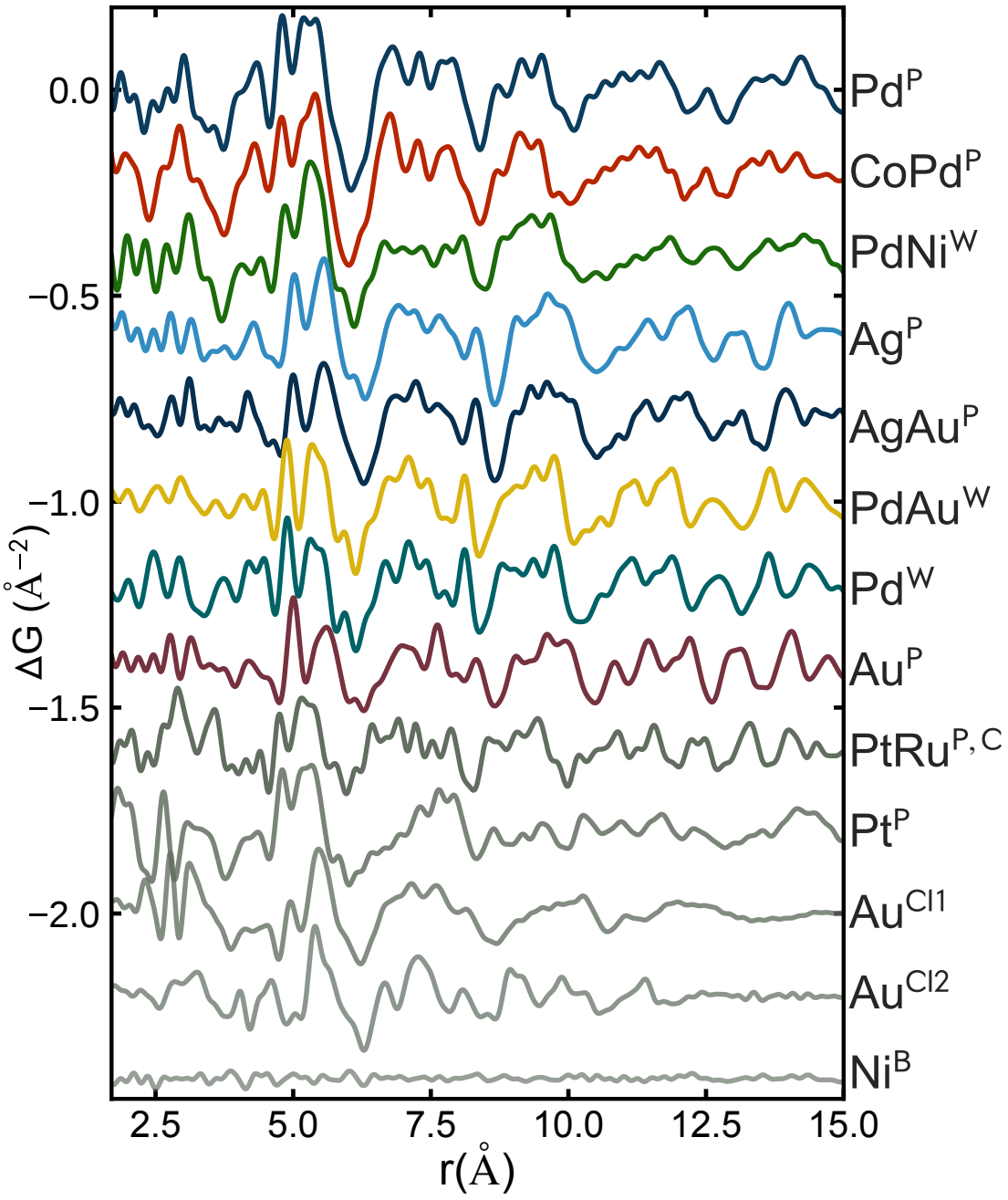

Figure 3.2: Difference curves from fcc AC refinements for samples listed in Table 3.1. The residual curves are normalized to place them on the same scale as the Pd curve for easier visual comparison. Bulk nickel is shown at the bottom, unscaled, for comparison. See Table 3.1 for the meaning of the curve labels.

structural origin of these features.

We sought simple models to explain the difference signals. Inspired by the structures of small metallic nanoparticles observed in high resolution electron microscopy (ie. Fig. 3.1d), and cluster structures solved by single crystal x-ray methods, we looked at spherical, octahedral, icosahedral, and decahedral models. The results in Fig. 3.3. show the difference curves that are obtained after each of these discrete cluster models are refined to their best-fit values, while varying only four parameters, an expansion coefficient, a scale factor, an isotropic atomic displacement parameter (ADP), and a parameter for correlated motion effects (δ_2). The top curve is the residual from the best-fit fcc AC model, yielding a refined spherical particle diameter, or fcc coherence length, of 1.9 nm. This is the first difference curve in Fig. 3.2 labeled Pd^P. Next we assess whether keeping the underlying fcc structure, but changing the shape of the cluster, in this case to a faceted truncated octahedron (suggested from a Wulff analysis) can explain the AC misfit. The best-fit difference curve of the octahedral model is shown in Fig. 3.3(b). It is largely unchanged from the fcc AC residual in Fig. 3.3(a). The prominent local structural features in the difference curve are not due to changes in nanoparticle shape. In Fig. 3.3(c) we show the best-fit difference curve for an icosahedral model. This is the closest magic sized icosahedron to a 2 nm sphere, consisting of 309 atoms. The difference curve is now considerably modified, which shows that changing from an underlying fcc basis to an icosahedral motif has a significant effect on the PDF. However, the agreement is substantially worse than the fcc AC misfit (in the figure the resulting difference curve had to be scaled down by a factor of 3), suggesting that the icosahedral structural modification is not present in the average Pd nanoparticle. Next we consider a decahedral model with a particle diameter, or maximum intervertex distance, of 2.7 nm. This model's best-fit difference curve is shown in Fig. 3.3(d). This also results in a significant change to the fit residual, suggesting that the PDF is sensitive to a decahedral structure modification,

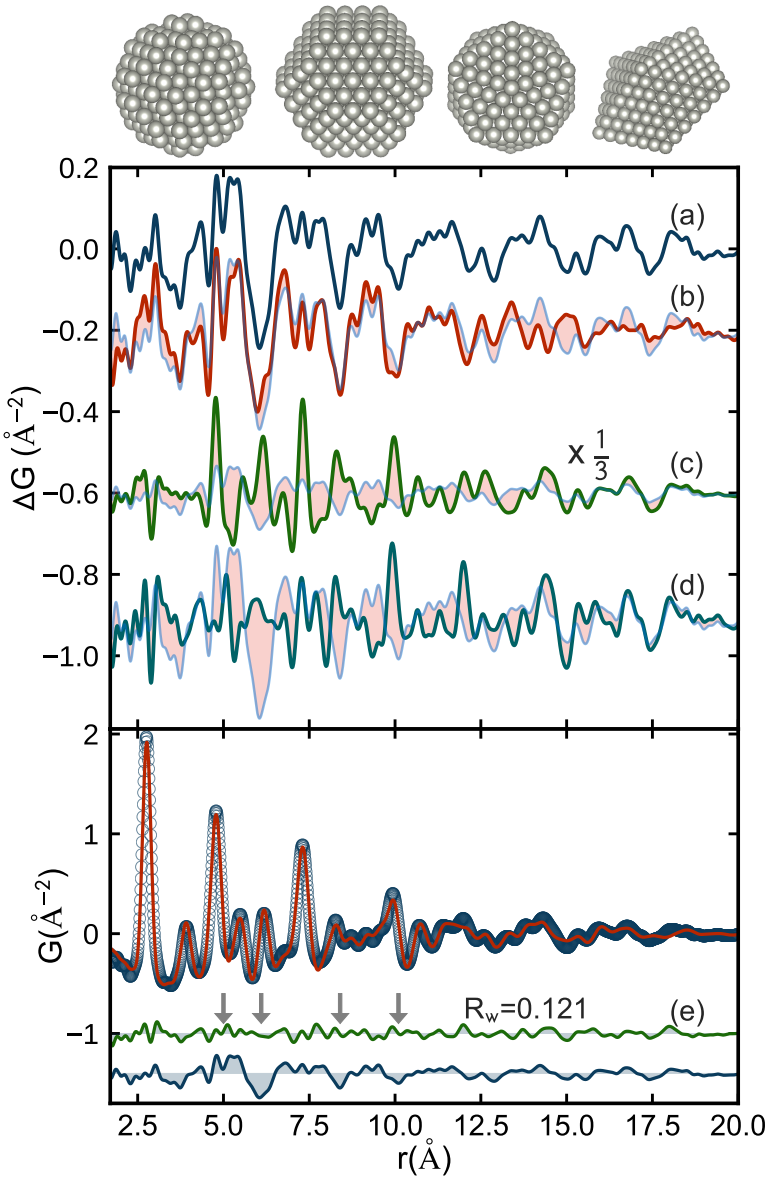

Figure 3.3: Top panel: Best-fit difference curves for different cluster models and the measured PDF of Pd^P. The cluster structures are shown above the panel in the same order from left to right. (a) fcc AC sphere (same curve as the top curve in Fig. 3.2) (b) truncated fcc octahedron (Wulff) (c) Mackay icosahedron (scaled by factor $\frac{1}{3}$) (d) regular decahedron. The difference curve from the AC model fit is shown as pale blue on each of the plots for comparison. Bottom panel (e): the measured PDF (open circles) and calculated (red solid line) from a 3.6 nm decahedron. Offset below in green is the difference curve, with again the AC residual curve reproduced below in blue. Arrows are positioned over characteristic features in the AC residual, as shown in Fig. 3.1.

but the overall agreement is still not ideal. However, close inspection of the difference curve suggests that many of the large amplitude features in the AC residual in the low-r region, below 10 Å, *are* corrected by this model, at the expense of misfit features appearing at high-r. The large features in the fcc differential in the region between 5-7 Å that are removed using the PDF calculated from a decahedral core come from two peaks, the 4th and 5th, which have an intensity ratio of around 2:3 in the fcc model but are approximately 1:1 for small decahedra, as shown in Fig. 3.3(e). This provides a way to recognize the possible presence of twinning from the PDF even before modelling. The presence of a relatively enhanced 4th peak is suggestive of decahedral twinning, though the converse is not true as decahedral models from large clusters can still produce intensity ratios close to 2:3 [111].

The appearance of additional misfit features at higher-r from this small 2.7 nm core may suggest that the decahedral structural modification is in the right direction, but a different sized cluster core is needed to fully explain the residual. We therefore tried different sized decahedra to see if we could improve the fit from $1.5 < r < 20$ Å, where the core structural misfit is most pronounced. The best-fit difference curve for a 3.6 nm diameter decahedron is shown in the lower panel of Fig. 3.3. This leads to a significant improvement in the agreement over the r-range capturing a majority of the experimental PDF signal, with the R_w decreasing by more than a factor of 2, from 0.253 to 0.121. All the large amplitude features in the difference curve are removed with this model. This analysis shows that the PDF can differentiate between different clusters, and that there are cluster models that can explain the widely seen fcc AC residuals. For demonstration we fit this same 3.6 nm decahedron to the samples generating residuals that appear to be highly correlated to the Pd difference curve in Fig. 3.2. The refined agreement factors and ADPs are given in Table 3.2, showing substantial improvements in both parameters, which is strong evidence that the core-structures for most of these samples must share important aspects in common with

Table 3.2: Comparison of fit results for attenuated crystal (AC) and decahedral (D) models to the samples that exhibit highly correlated difference curves in Fig. 3.2. R_w in the subscript indicates the refined agreement factor, and U_{iso} the refined atomic displacement parameter (ADP) values. All decahedral fits indicated by D use a single 3.6 nm (609 atom) regular decahedron, as shown in Fig. 3.3.

Name	AC_{R_w}	D_{R_w}	Δ R_w (%)	$AC_{U_{iso}}$ (Å^2)	$D_{U_{iso}}$ (Å^2)	Δ U_{iso} (%)
Pd^P	0.253	0.121	-52.1	0.016	0.012	-22.5
$CoPd^P$	0.322	0.199	-38.1	0.020	0.014	-27.5
$PdNi^W$	0.281	0.173	-38.6	0.014	0.005	-64.4
Ag^P	0.229	0.156	-31.9	0.016	0.010	-35.7
$AgAu^P$	0.237	0.162	-31.9	0.016	0.010	-37.2
$PdAu^W$	0.189	0.127	-33.1	0.012	0.007	-40.6
Pd^W	0.165	0.173	+4.90	0.009	0.005	-45.1

the best fit decahedral core for Pd^P. Other sources of structural misfit, such as different crystallite size and shape distributions, are likely to exist.

We now turn our attention to the difference curves at the bottom of Fig. 3.2 which appear slightly different to those from the decahedral samples that have been discussed previously. For a sample that is representative of this behavior we pick Au^{Cl2} whose difference curve, when fit with the AC model, is shown in grey at the bottom of Fig. 3.2 and reproduced as the top grey curve in Fig. 3.4. We carry out the same analysis that was done for the Pd^P decahedron, by comparing the difference curves of various discrete cluster models. As before, the Wulff-shaped discrete fcc cluster (Fig. 3.4b) does little to affect the AC difference curve

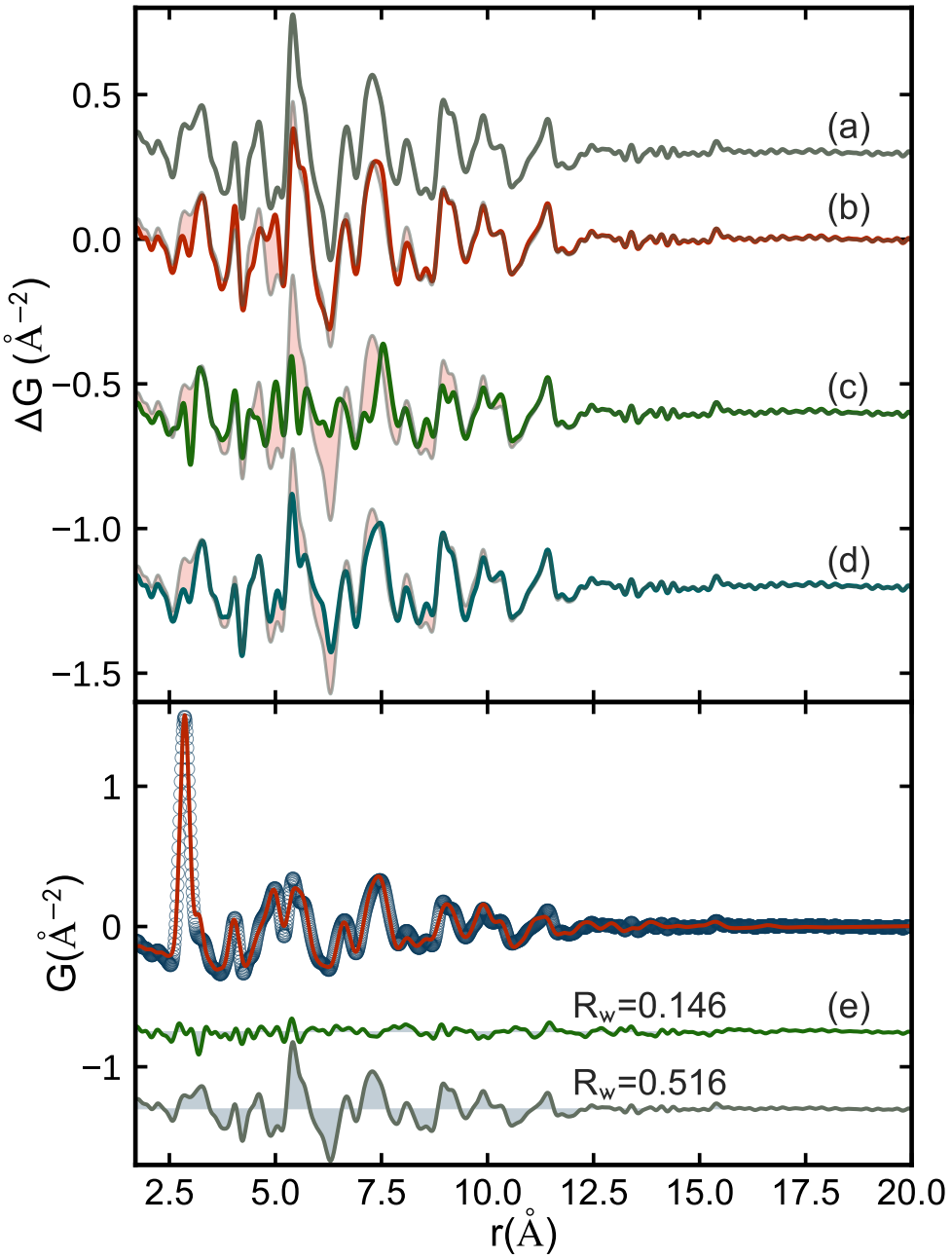

Figure 3.4: Top panel: Best-fit difference curves for different cluster models and the measured PDF of Au^{Cl2}. (a) fcc AC model (same curve as the second to bottom curve in Fig. 3.2) (b) truncated fcc octahedron (Wulff) (c) Mackay icosahedron (d) truncated decahedron. The difference curve from the AC model fit is shown as pale grey and overlaid on each of the plots for comparison. Cluster models (b-d) each contain exactly 55 atoms. Bottom panel: the measured PDF (open circles) and calculated (red solid line) from the Lopez-Acevedo 144 atom structure containing an icosahedral core. Offset below are the discrete (green) and AC (grey) difference curves.

(Fig. 3.4a). However, this time the decahedral model (Fig. 3.4d) also does little to reduce the signal in the residual. On the other hand, an icosahedral model does a significantly better job, at least in the low-r region (Fig. 3.4c). This suggests that the core of the underlying metallic cluster is icosahedral in nature rather than decahedral and that the PDF is again able to differentiate between these possibilities, as demonstrated for Pd^{P}.

Although the signal in the difference curve is greatly reduced by the icosahedral cluster, from $R_w = 0.516$ for the AC model to $R_w = 0.289$, the agreement factor is still much larger than the best-fit decahedron in Fig. 3.3(e). In fact, there is an established DFT-derived structure solution for Au^{Cl2} cluster [90] which was corroborated by STEM and PDF studies [11, 59]. We computed the PDF directly from this 144 atom model and compared it to the experimental Au^{Cl2} PDF in the lower panel of Fig. 3.4. It gives an even better agreement to the measured PDF, reducing the R_w to 0.146. It also results in much smaller refined ADPs, with U_{iso}'s reduced by a factor of ~ 5 versus the AC model, from 0.034 to 0.0066. The refined parameters are comparable to the best-fit decahedral models and approach those obtained from crystalline materials. It is interesting to investigate the differences between the Lopez-Acevedo structure (LA model) and the simple 55 atom magic icosahedral cluster that we used (see Modelling section for details). The LA model has a 54 atom icosahedral core consisting of two Mackay shells with 20 tetrahedral faces, which is nearly identical to the 55 atom icosahedron, the difference being the absence of one central atom (the first Mackay "shell"). However, in the LA model the layers surrounding this core do not follow the Mackay packing at all. Instead, they are generated by placing 60 atoms at hcp sites on the surface of the 54 atom icosahedral core, 3 per {111} faceted tetrahedral face. There is also an outermost shell protecting the 114 atom cluster with 30 thiolate-gold staples. This explains why the fit of the 55 atom icosahedral core model does well in the low-r region of the PDF, which is dominated by signal from the core, but not at high-r, which contains only

information about the outer-layers of the cluster.

3.3 Discussion

A striking aspect of these results is the robustness of the difference curve signal from the decahedral samples. Highly reproducible residuals were obtained between best-fit calculated PDFs compared to PDFs from data measured at four different synchrotron sources on single element and alloyed nanocrystals, prepared using different synthesis methods, and with markedly different morphologies. This underscores the fact that the structural information contained in the difference curves does not depend sensitively on experimental conditions, particle shape, composition, or even size. This is further borne out by the observation that the standard Wulff models did nothing to fit those signals, which therefore do not originate from differences in sample size/shape but must have a different structural origin. The fact that decahedral cluster models could be found that removed the signature features in the residual shows that the structural origins of the fcc AC misfit are in the details of the nanocrystal cores. Again, we note that it is not the morphology of the discrete decahedral models that improves the fit.

The decahedral cluster models used here are made up of 5 tetrahedral sub-units of fcc close-packed material arranged in a star shape with a common aligned $\langle 110 \rangle$ tetrahedral edge, and a slight elongation to the 5 pentagonal edges. They are faceted, similar to the Wulff and octahedral models, but the primary modification to the fcc structure captured in many fit residuals is due to the presence of $\{111\}$ type contact twins at the boundaries between tetrahedral domains in the decahedron. The presence of twin boundaries introduces new interatomic distances into the model that are not present in the unfaulted structures but are needed to explain the measured PDFs. It is also important to note that the diameter

of the decahedral model that had the best agreement with the Pd^P data was nearly double that of the best-fit spherical model (3.6 nm rather than $\sim$ 2 nm for the AC model). Actually, in a 3.6 nm regular decahedron the characteristic dimension of the fcc tetrahedral sub-unit is 1.9 nm. Presumably the somewhat low symmetry of the multi-domain structures leads to a rather large number of similar but not identical inter-domain interatomic distances which overlap and reduce the number of distinct PDF peaks in the high-r region.

The TEM estimate for the Pd^P particle diameter is 3.0 nm, whereas the best fit decahedral cluster is 3.6 nm which seems to be problematic. In Fig. 3.13 we show that there is a robust signal in the PDF that extends to around 4 nm and even above. This shows, beyond doubt, that the sample contains at least some clusters that have dimensions of $\sim$4 nm. The cluster-fitting approach determines a single average cluster, not a distribution of clusters, and the diameter of the best fit decahedron for Pd^P is consistent with the visual observation in Fig. 3.13. The TEM estimate of particle size was made by automated segmentation analysis of micrographs in ImageJ, where determination of particle size distributions are subject to user-selection of appropriate thresholding algorithms, and can be prone to error when the particles are not spherical but oblate, as is the case here.

It is interesting that we also observe a robust decahedral signal in the difference curves from the metallic nanowire samples. This clearly shows that these samples must also contain significant numbers of twin boundaries. The importance of decahedral-like twinning in large 50-100 nm wires has been widely noted in the literature [155, 172, 91, 54]. Here we also find them in very thin $\sim$ 2 nm diameter wires, previously thought to consist of single crystalline fcc segments [70, 71, 85], and show that PDF can be a powerful method for establishing the presence of domains in highly anisotropic morphologies.

This work also suggests that caution should be exercised when introducing more complex models to explain nanocrystal data. We have obtained fits to both elemental and alloyed

PDFs from metallic nanoparticles and nanowires that have R_w values well below 0.2 with a single decahedral cluster structure that contains only 4 refinable parameters. That is not to say that better fits cannot be obtained with more complicated models, such as heterogeneous core shell structures including models with surface oxide phases and nanoparticle-ligand correlations, but there is a very small signal in the difference curve that is left to be fit by the additional degrees of freedom in these models. As an example, the difference curve below the data in the lower panel of Fig. 3.3 illustrates the amplitude of the unfit signal that is left after fitting the 4-parameter decahedral cluster. This is representative of the signal left over that would be available to constrain additional parameters in other models.

Finally, we would like to emphasize the value of interrogating fit residuals carefully. While this may seem obvious, it is oftentimes forgotten in PDF studies of nanomaterials where poor fits are accepted as a *de facto* limitation of nanoparticle studies, or comparisons of simulated PDFs are used to glean understanding from experimental data without refinements [75, 119, 74, 147, 118, 4, 132, 133, 111].

3.4 Synthesis Methods and Transmission Electron Microscopy Characterization

Pd and CoPd nanocrystals (NCs) were synthesized by modifying a previously reported method [101]. For Pd NCs, palladium (II) acetylacetonate ($Pd(acac)_2$, Acros, 98%) was reduced in the presence of tert-butylamine borane (Sigma-Aldrich, 97%) and oleylamine (OAm, Sigma-Aldrich, 70%). The CoPd NCs were synthesized by coreduction of cobalt (II) acetylacetonate ($Co(acac)_2$, Sigma-Aldrich, 97%) and palladium (II) bromide, ($PdBr_2$, Strem Chemicals, 99%) at 260 °C in OAm and trioctylphosphine (TOP, Sigma-Aldrich, 97%). The Pt NCs were synthesized based on a previously reported method [162]. Platinum

(II) acetylacetonate ($Pt(acac)_2$, Acros, 98%) was reduced at 300 °C in a mixture of benzyl ether (Sigma-Aldrich, 98%), OAm, oleic acid (2.5 mmol, Sigma-Aldrich, 90%) and TOP.

Transmission electron microscopy (TEM) images were collected on a JEOL JEM-1400 microscope operating at 120 kV. High-resolution TEM (HRTEM) images were collected on a JEOL F200 scanning/transmission electron microscope operating at 200 kV. The elemental composition of CoPd NCs was determined by inductively coupled plasma-optical emission spectrometry (ICP-OES) performed on a Spectro Genesis spectrometer with a concentric nebulizer.

Representative TEM microscopy for Pd^P, $CoPd^P$, and Pt^P are shown in Figures 3.5, 3.7, 3.8 and HRTEM images of individual Pd NPs are shown in Figure 3.6. The particle size and size distributions were determined by measuring > 200 particles per sample using the ImageJ software [149]. Micrographs are imported in ImageJ and the default automated thresholding was applied. The areas of individual particles are then tabulated using the Analyze Particles function, and converted to a distribution of particle diameters, with the assumption that the areas are circular.

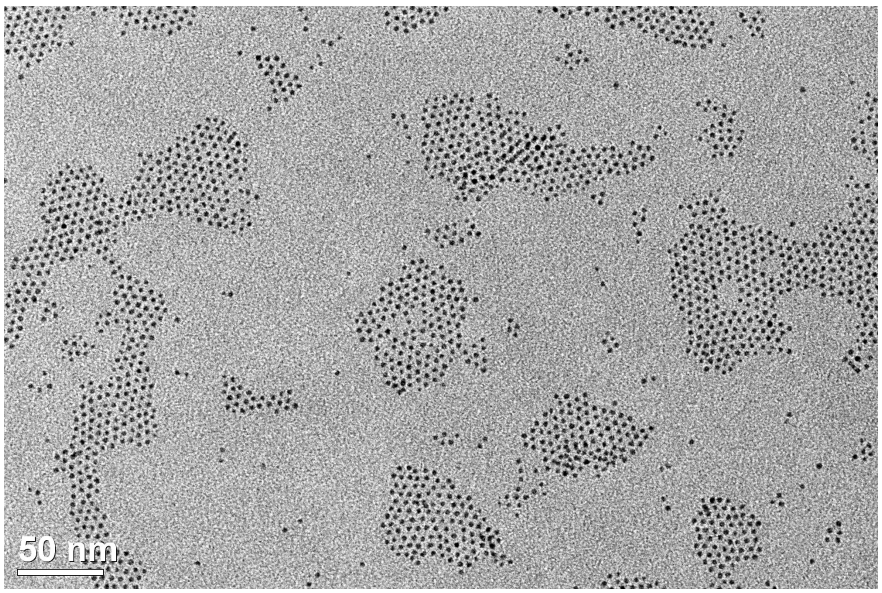

Figure 3.5: TEM image of Pd NPs with an estimated average particle size of 3.0 ± 0.3 nm

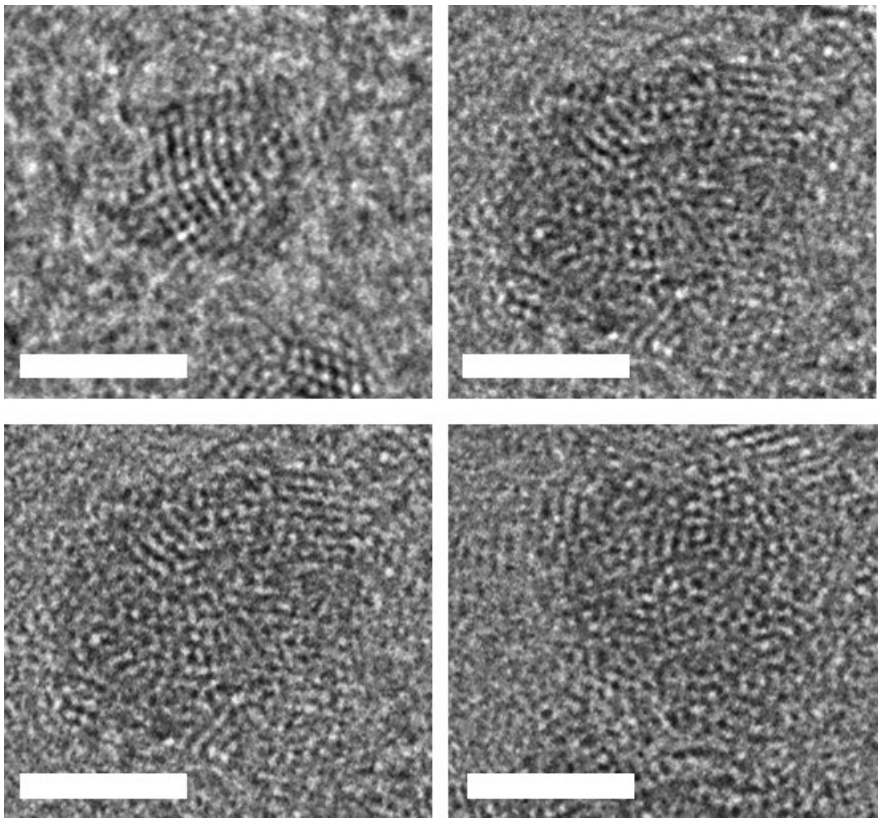

Figure 3.6: HRTEM images of isolated Pd NPs. The scale bars are 2 nm.

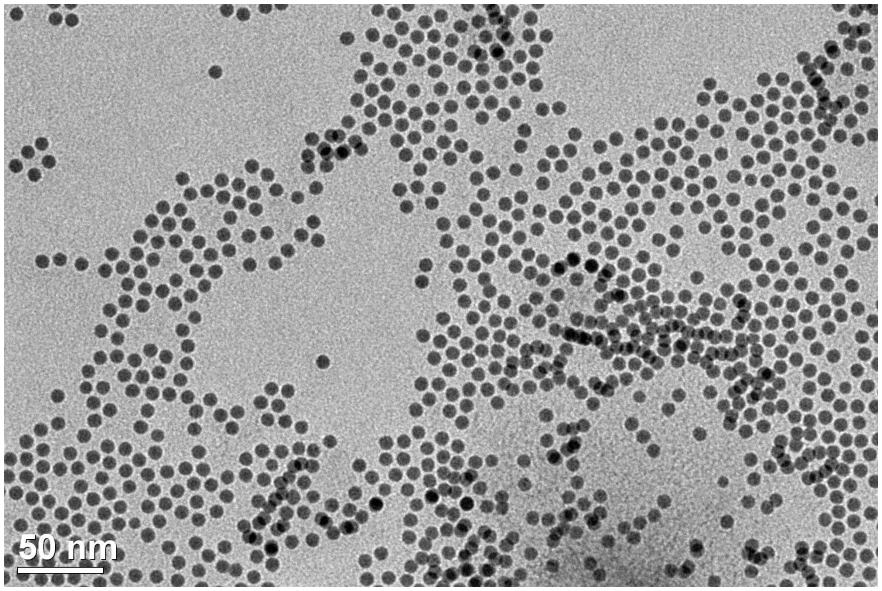

Figure 3.7: TEM image of CoPd NPs with an estimated average particle size of 8.6 ± 1.7 nm

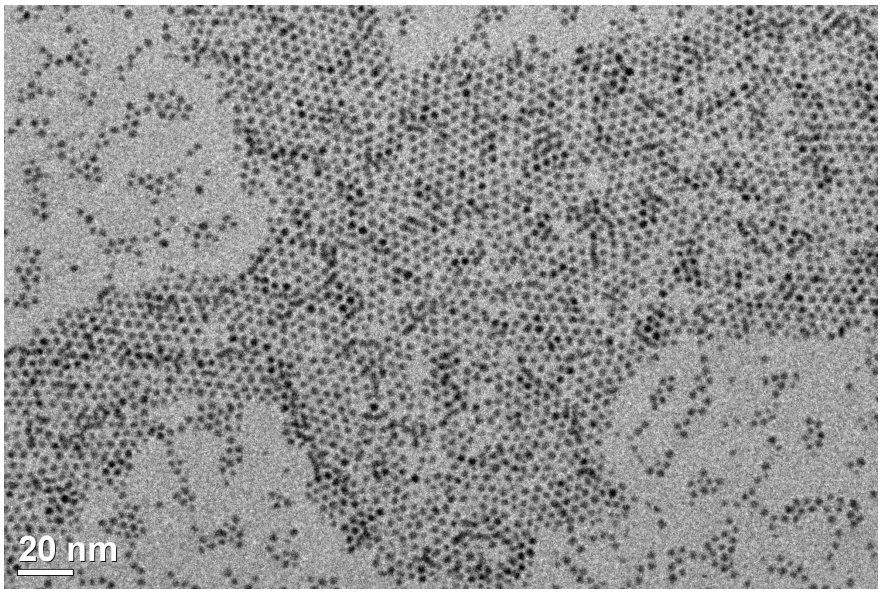

Figure 3.8: TEM image of Pt NPs with an estimated average particle size of 3.0 ± 0.4 nm

Ag^P, Au^P, $AgAu^P$ samples were prepared following synthesis methods reported in Ristig et al. [141]. Additional studies by Grasmik et al. [47], Banerjee et al. [14] and Mahl et al. [95] include HRTEM images of NPs produced by the same synthesis methods as the NPs

measured by PDF here. In Figure 3.9 we have reproduced HRTEM images of isolated Au and AgAu NPs which show evidence of domain structures for both materials, with different particle sizes and functionalized with different ligands (see Figure 3.9 for details). $PdNi^{W}$, $PdAu^{W}$, and Pd^{W} samples were prepared using protocols described, and TEM microscopy provided in, Liu et al., Koenigsmann et al. (2012) , and Koenigsmann et al. (2011) respectively [85, 71, 70]. Au^{Cl1} and Au^{Cl2} cluster data were taken from PDF measurements and synthesis methods discussed in Jensen et al. [60].

$PtRu^{P,C}$ catalysts were purchased commercially from Johnson Matthey Fuel Cells and aerosol and jet printed on mesoporous carbon supports. Bulk Ni is a commonly used calibrant for PDF measurements at beamline 28-ID-2 (NSLS-II). Please see the existing literature, as listed above, for sample characterization and microscopy corresponding to the nanoparticles and nanowires used in this PDF modelling study.

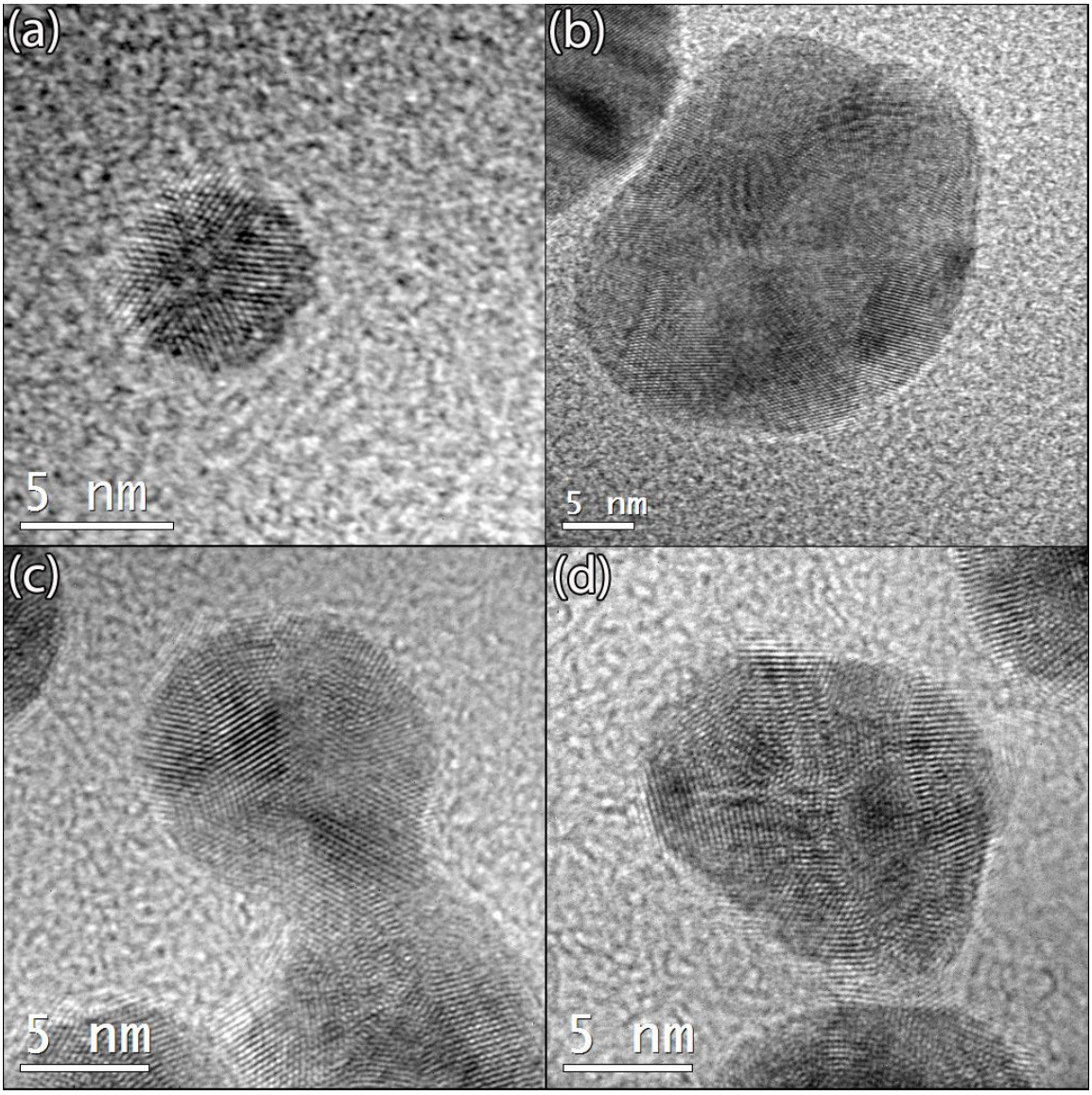

Figure 3.9: Top row: HRTEM images of (a) poly(*N*-vinylpyrrolidone) (PVP) and (b) tris(3-sulfonatophenyl) (TPPTS) functionalized Au NPs. Bottom row: HRTEM images of (c) PVP and (d) TPPTS functionalized AgAu NPs. Reprinted by permission from Springer Nature and the authors. Journal of Nanoparticle Research, "Silver, gold, and alloyed silvergold nanoparticles: characterization and comparative cell-biologic action," Mahl, D., Diendorf, J., Ristig, S. et al. (2012).[95]

3.5 Total Scattering Measurements

Table 3.3: Composition: Elemental and alloyed atomic ratios used to normalize the total scattering signal $I(Q)$ by the relative scattering strength of atomic species in the sample. Ligand atoms were not included in the normalization. Background: Samples 3, 5, and 6 are NWs embedded in a Carbon matrix and loaded as powder into Kapton tubes. The background used is the Carbon support plus Kapton. Sample 9 is a NP powder deposited directly onto a carbon paper film without any Kapton using an ink-jet printer. Q_{damp}/Q_{broad}: Instrumental parameters are calibrated using a crystalline Nickel sample measured directly before the nanocrystalline sample. *Q-range*: The *Q-range* is tuned per sample to give the best balance between statistical noise and real space resolution. The small angle ligand contribution, when significant, is removed by increasing Q_{min} to values that are appropriate for nanoparticles. Total exposure times differed between samples, but were typically less than five minutes. See Fig. 3.11 for a comparison of repeated measurements on $AgAu^P$.

Index	Date	Composition	Bkgd	λ (Å)	Q_{damp}	Q_{broad}	Q_{min}	$Q_{maxInst}$	Q_{max}	Temp (K)
1	3/2017	Pd	KaptonTape	0.1846	0.0367	0.0107	1.0	26.0	23.0	300
2	3/2017	$Co_{0.2}Pd_{0.8}$	KaptonTape	0.1846	0.0367	0.0107	1.0	26.0	23.0	300
3	6/2014	$Pd_{0.83}Ni_{0.17}$	XC72R Carbon	0.1860	0.0421	0.0188	1.0	27.4	20.5	100
4	2/2016	Ag	1mm Kapton	0.1821	0.0425	0.0155	1.0	24.0	24.0	300
5	5/2018	$Ag_{0.5}Au_{0.5}$	1mm Kapton	0.1666	0.0382	0.0221	0.1	25.0	25.0	300
6	6/2014	$Pd_{0.9}Au_{0.1}$	XC72R Carbon	0.1860	0.0421	0.0188	1.0	27.4	20.5	100
7	6/2014	Pd	XC72R Carbon	0.1860	0.0421	0.0188	1.0	27.4	20.5	100
8	2/2016	Au	1mm Kapton	0.1821	0.0425	0.0155	1.0	24.0	24.0	300
9	1/2017	$Pt_{0.5}Ru_{0.5}$	Graphitic Carbon	0.1827	0.0452	0.0171	1.0	28.0	25.0	300
10	3/2017	Pt	1mm Kapton	0.1846	0.0387	0.0106	1.0	26.0	25.0	300
11	1/2015	Au	1mm Kapton	0.1744	0.0400	0.0100	1.3	29.0	28.0	100
12	1/2015	Au	1mm Kapton	0.1430	0.0400	0.0100	0.8	30.0	27.0	100
13	3/2017	Ni	1mm Kapton	0.1846	0.0387	0.0106	0.1	26.0	25.0	300

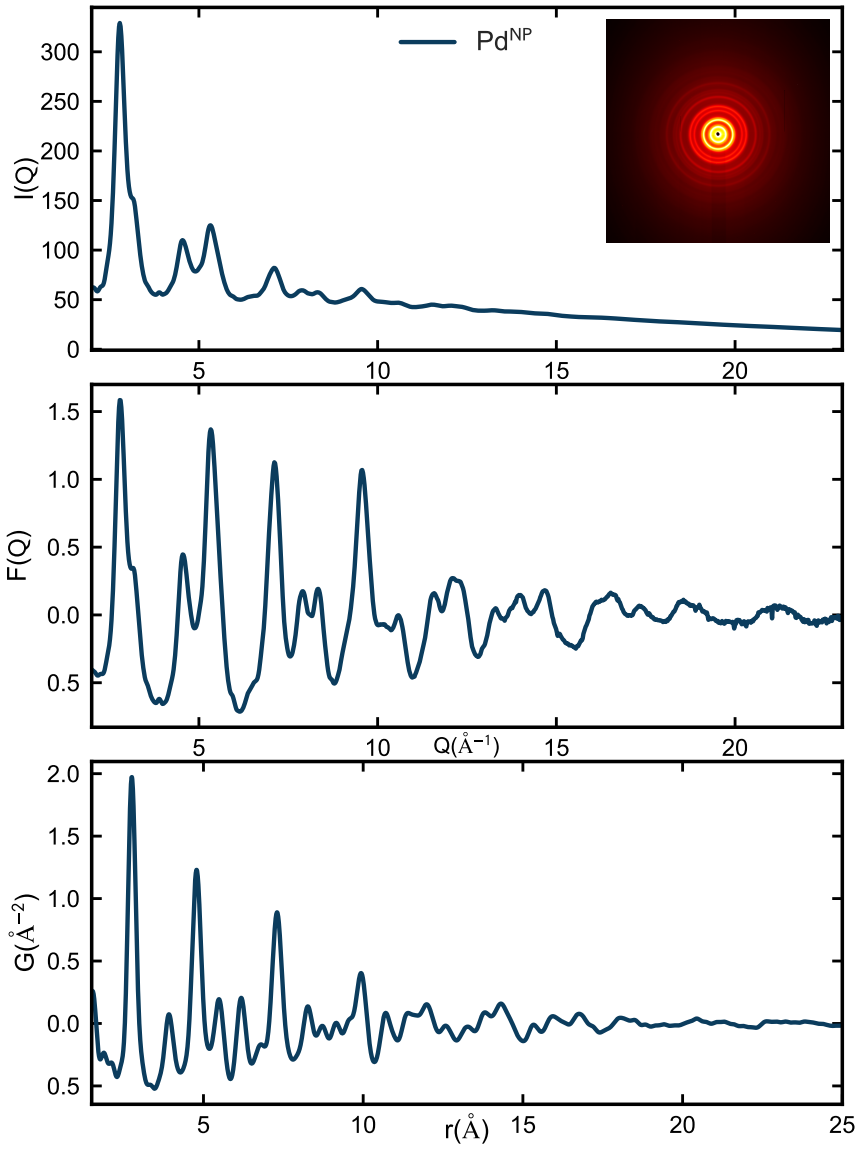

Figure 3.10: Example of the typical data reduction and PDF transformation procedure, applied to the representative Pd^P sample discussed in the results section. Top row: Background subtracted total scattered intensity $I(Q)$ obtained after masking and azimuthally integrating the raw 2D diffraction pattern shown in the inset. Middle row: The reduced total scattering structure function $F(Q)$. Bottom row: The reduced atomic pair distribution function $G(r)$, obtained from a sample after sine Fourier transformation of $F(Q)$, excluding the small angle scattering (SAS). See the PDF methods section for additional details.

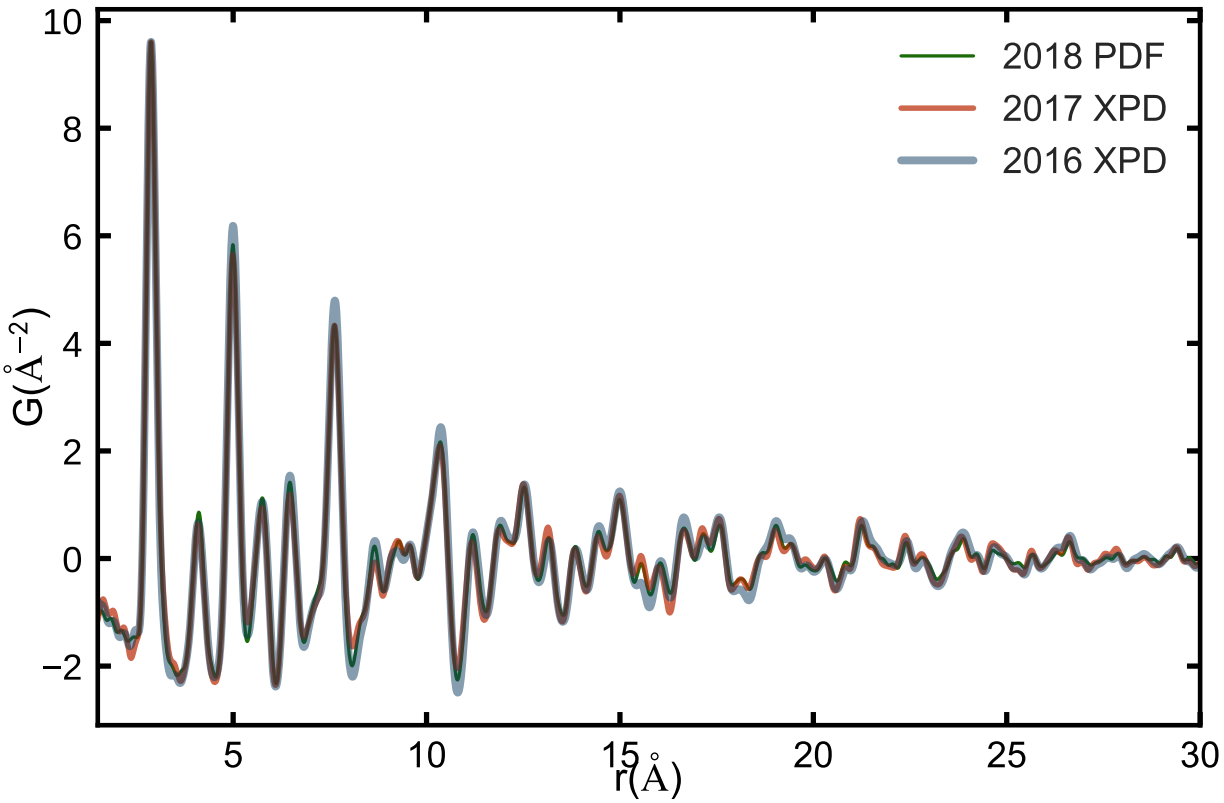

Figure 3.11: Measurements of one AgAu^P sample, at two NSLS-II beamlines (as labeled). PDFs change minimally over three years suggesting that the dried nanoparticulate powders did not degrade significantly, and that PDF data reduction protocols following image acquisition are highly reproducible and consistent, even between different beamlines.

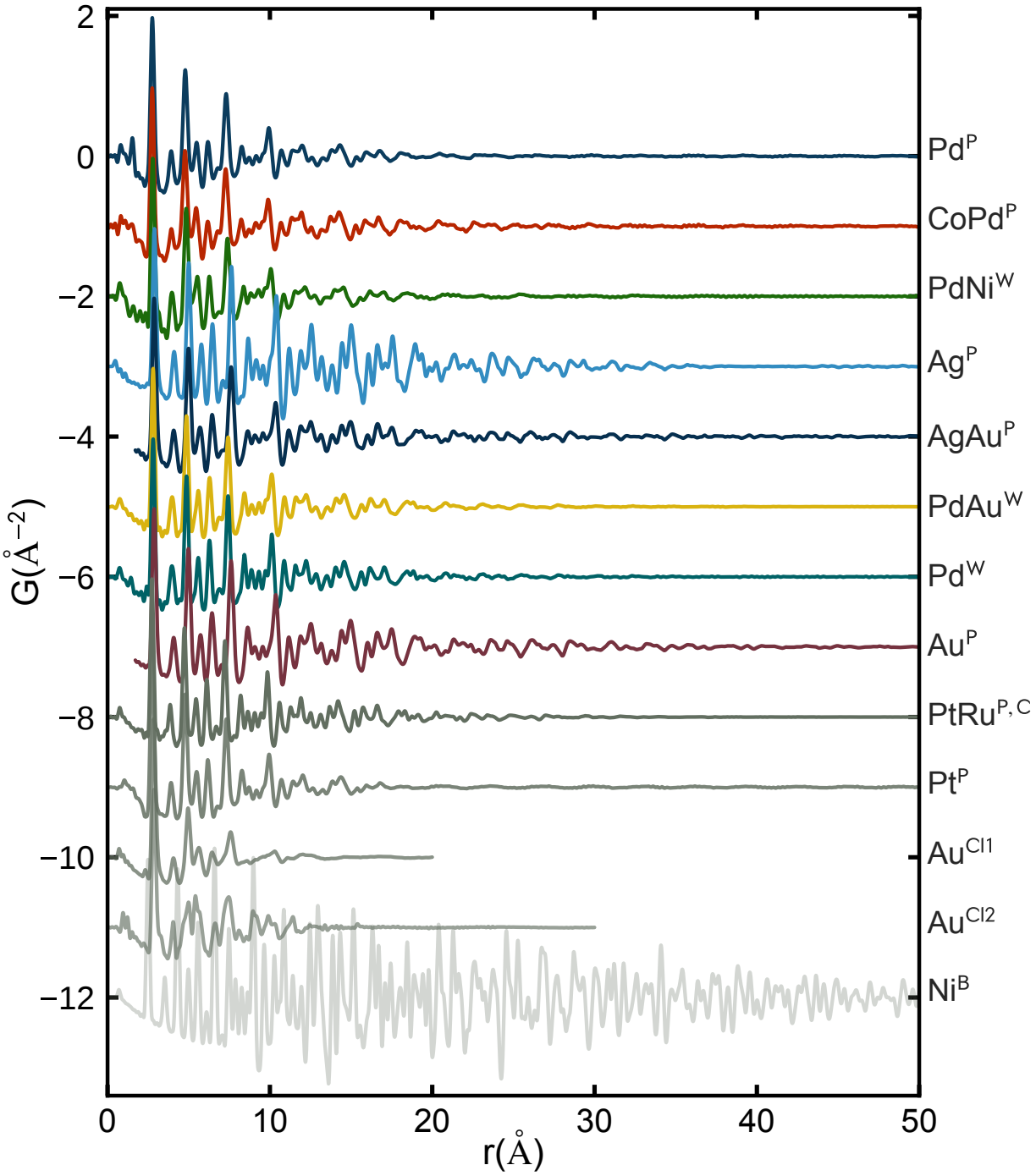

Figure 3.12: Experimental PDFs for samples and residuals discussed in the results section. As before, morphologies labeled are: nanoparticle (P), nanowire (W), nanocluster (Cl), and bulk (B). C indicates the sample was on a carbon support.

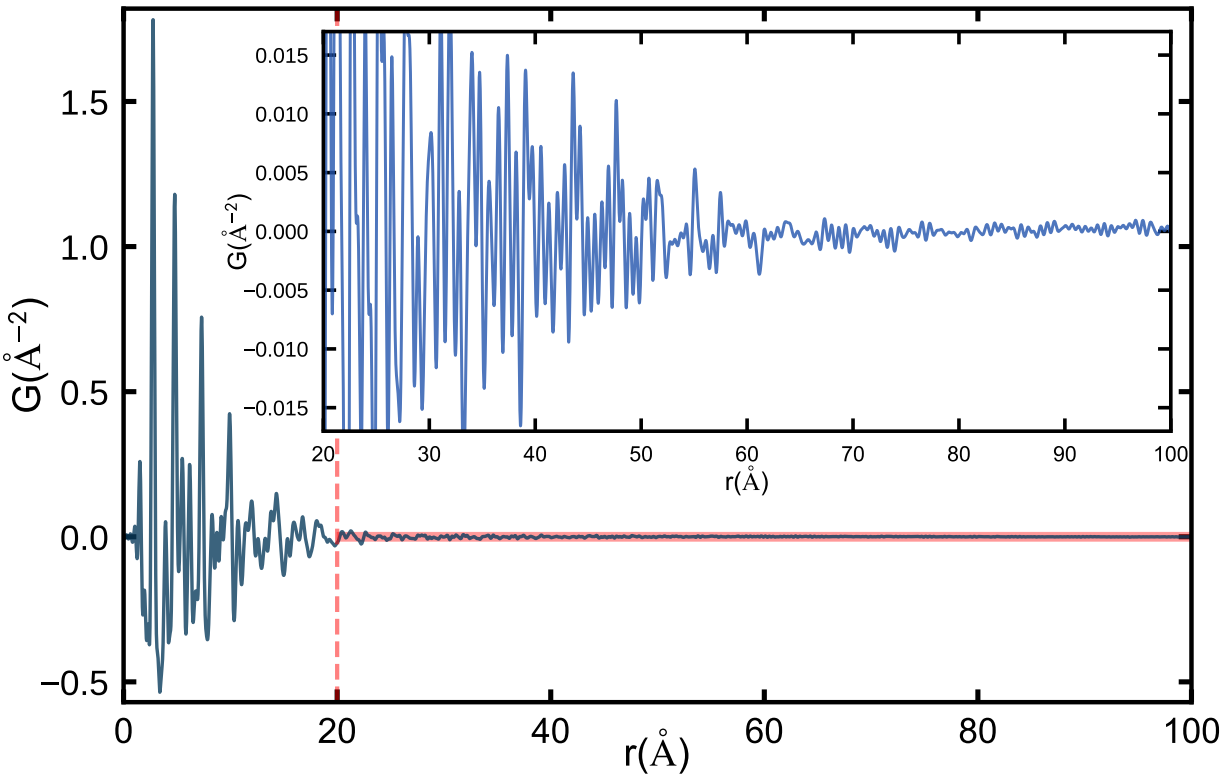

Figure 3.13: Experimental PDF for Pd^{P}. The inset shows the high-r region from $20 < r < 100$ Å magnified. Structure in the PDF, indicating a structural signal, may be seen extending past 4.0 nm, showing that coherent domains exist in the sample at these sizes. The best fit cluster model for this sample had a width of 3.6 nm, which is the best representation of the mean particle size, though the distribution of particle sizes includes particles that deviate from the average.

3.6 Structure Builders

The atomic simulation environment (ASE) python package was used to build candidate discrete structures using the functions provided below [77].

Pd^{P} cluster models were generated as follow, given in the same order they appear in Fig. 3.3 (a-e). Note that the CUT_SPHERICAL_CLUSTER composite function is equivalent to the spherically attenuated virtual crystal model described in the results section.

```
cut_spherical_cluster(sphericalFCC(elem="Pd", nlayers=6,
                                   latticeconstant=3.89), radius=10)
wulff_construction(elem="Pd", surfaces=[(1,1,1), (1,0,0)],
                   esurf=[0.9, 1.0], size=300,
                   rounding="closest", latticeconstant=3.89)
Icosahedron(elem="Pd", noshells=5, latticeconstant=3.89)
Decahedron(elem="Pd", p=7, q=1, r=0, latticeconstant=3.89)
Decahedron(elem="Pd", p=9, q=1, r=0, latticeconstant=3.89)
```

Au^{Cl2} cluster models as shown in Fig. 3.4 (b-d):

```
wulff_construction(elem="Au", surfaces=[(1,1,1), (1,0,0)],
                   esurf=[0.8, 1.0], size=50,
                   rounding="closest", latticeconstant=4.08)
Icosahedron(elem="Au", noshells=3, latticeconstant=4.08)
Decahedron(elem="Au", p=3, q=3, r=0, latticeconstant=4.08)
```

Chapter 4

Screening large numbers of nanoparticle structure models

Non-crystallographic structures have long been reported in electron microscopic studies of metallic nanoparticles [56, 57, 97, 156, 25] and it is established that growth mechanisms across a diversity of synthesis methods are directed by the size-dependent formation and rearrangement of multiply-twinned domains, in addition to thermodynamic stabilization of nanoparticle surfaces by capping agents [87, 76, 98]. Despite this evidence, atomic models built from face-centered cubic (fcc) cores, which do not account for the multi-domain nature of these materials, are still commonly used in PDF analysis of metallic nanostructures [126, 119, 75, 41, 167, 132, 124].

It was recently demonstrated that the atomic pair distribution function (PDF) does contain information allowing for the detection and characterization of internal atomic interfaces in a diversity of metallic nanomaterials and atomic clusters [15]. It was also shown that the PDF could differentiate between various arrangements of multiply-twinned domains. For a majority of the samples surveyed, simple decahedral or icosahedral cluster cores, instead of

fcc attenuated crystal (AC) approximations or single crystal fcc cutouts, gave significantly improved fits. This analysis hinged on time-consuming, manual trial-and-error refinements of a few representative cluster models from different structure motifs. Here we describe a new approach for determining the best models for metallic nanoparticle core structures, by automatically generating large numbers of candidate cluster structures and comparing them to PDF data from nanoparticles. The methodology differs from traditional approaches for crystallographic analysis of nanoparticles where a single model containing many refinable parameters is used to fit peak profiles from a measured diffraction pattern. Instead, this approach uses many structure models and highly constrained refinements to screen libraries of discrete clusters against experimental PDF data, with the aim of finding the most representative cluster structures for the ensemble average nanoparticle from any given synthesis.

4.1 Modeling

The core of the new approach is to generate large numbers of candidate structure models, which in principle could be pulled from databases, or generated algorithmically. PDFs are then computed from each model and compared to a measured PDF. A small number of refinable parameters may be varied in this last comparison step, such as an overall scale factor and an average bond-length, in such a way as to minimize an agreement factor, R_w, described in greater detail below. The results of the comparisons for all models are then reported back to the experimenter. In this initial implementation we tested finite-sized cluster models, which we use to compare against data collected from small metallic nanoparticle samples, and in this case we generate the libraries of clusters, which we call cluster-mines, algorithmically.

Clusters may be grouped into different types, or motifs, which have specific algorithmic

structure builders. Here we consider motifs built from densely packed hard sphere models which form a seed, or atomic core for the metallic nanoparticles of interest.

Three dense packing configurations were used in this study; N specifies the smallest building block for the atomic core:

1. The cubic close-packed tetrahedron ($N = 4$) yielding fcc clusters [66, 50]

2. The pentagonal bipyramid ($N = 7$) which generate decahedral clusters [10]

3. The icosahedron ($N = 13$) used to build magic or Mackay icosahedra [92]

A diversity of different cluster geometries can be made by stacking layers of atoms in specific arrangements on top of the densely packed atomic seeds, and by truncating the growth along different high-symmetry directions [99]. These structure-building algorithms are implemented in the Python atomic simulation environment ASE [77], and other motifs including monotwinned clusters are currently being developed. A fourth motif, singly-twinned fcc bicrystals, were also built and tested by applying a simple transformation to fcc single crystal clusters. Briefly, fcc clusters are cut along a {111} lattice plane, and misoriented by applying a 60° rotation to one half of the crystal around an axis normal to the {111} plane. This is done to fcc crystals with an odd number of ccp layers such that one {111} contact twin plane, resulting in two mirror-equivalent domains with the same number of atoms, are generated. In the coincident site lattice (CSL) notation, this constitutes a {111} $\Sigma 3$ coherent twin boundary for cubic crystals [72]. In this way, popular cluster types from the literature are created and added to the mine, but this also illustrates how other cluster-types may be generated and addeed in the future.

The geometries which result from the different motif-specific truncation criteria can be classified as families, which share the same local atomic environment common to each motif, but differ in the topology of their polyhedral surfaces. For example, in the ASE decahedron

structure-builder, four parameters can uniquely specify a cluster model: a nearest neighbor bond distance, the number of layers parallel to the 5-fold axis, the number of layers truncated perpendicular to the 5 pentagonal edges, and the number of layers truncated perpendicular to the 5 apical vertices. When no truncation exists, regular decahedra or pentagonal bipyramids are generated, whereas truncation of the pentagonal edges produces families of Ino-truncated wire-like decahedra [56] and apical truncation yields Marks decahedra [96] with reentrant facets. Changing the type and degree of truncation influences the resulting morphology of the cluster, and in decahedra, this also changes the relative number of atoms within the 5 fcc-like subunits versus the atoms situated at twin boundaries between the decahedral domains and at surfaces.

If a unique set of parameters that specify a cluster model is given as input to a structure-builder in ASE, a list of cartesian coordinates is returned which may be read in to a PDF calculating program. In this case we use our own complex modeling infrastructure, CMI [65]. PDFs are then calculated from the atomic coordinates using the Debye scattering equation [33] PDF calculator implemented in DIFFPY's DEBYEPDFGENERATOR class under SRFIT. The atomic coordinates in space are held constant in the refinements but four parameters are allowed to vary to obtain good agreement between the calculated and measured PDFs: an isotropic expansion coefficient (linear scaling in r) to account for differences in nearest neighbor distances, a single U_{iso} (isotropic ADPs), a single scale factor, and δ_2, a parameter for correlated motion effects [135]. Parameters that describe the resolution of the measurement, (Q_{damp} and Q_{broad}), are obtained by independently refining a bulk calibrant measured in the same geometry as the nanocrystalline sample and fixed.

The cluster mine is built by iterating through the integer values for parameters, and combinations thereof, specifying the number of added and truncated layers for each motif-specific structure-builder. The size of the structure mine (the number of clusters in the mine)

can be tuned by providing bounds on the values that a given builder parameter may take, or by specifying a minimum and maximum number of atoms (N_a) in the clusters regardless of the builder. During this procedure, CLUSTER-MINING stores metadata such as the number of atoms, atom type, nearest neighbor distance and motif, starting values for the refinable variables, along with the set of integers for that cluster. This information is then passed to ASE which generates the xyz atomic coordinates, which are then used as inputs to CMI to calculate the PDF and refine the variable parameters against a measured PDF, for each cluster in the mine. The fit range in r can also be adjusted prior to refining the library of clusters. The CLUSTER-MINING program then returns a table of initial and refined PDF parameter values, and goodness of fit (R_w), with each individual refinement linked to the input cluster parameters and associated metadata. A plot can then be generated of the best fit R_w vs. the number of atoms (N_a) for all clusters in the mine. We call this plot the cluster-screen map. The cluster-screen map can be filtered or labeled according to any cluster specific metadata, such as the motif.

The dimension of the input parameter space (typically 3-6) is significant and so the size of the mine can be large. For example, 2,419 unique combinations are possible for decahedra containing less than 1,500 atoms, including regular, Ino, Marks, and Ino-truncated Marks families. However, the cluster-mining approach is easily parallelizable and lends itself to deployment on multi-node computers. As well as giving more ideal cluster model fits than, for example, stochastic approaches [119], the procedure greatly speeds up a researcher's workflow compared to more manual trial and error approaches. This approach to nanostructure modeling may also be sped up by increasing the efficiency of selection of the clusters from the mine for testing, and we expect that statistical approaches such as machine learning will be effective in this regard, though this is beyond the scope of this paper.

4.2 Experimental Methods

Pd samples were prepared by the Murray group using methods described by [101]. Synthesis of $Au_{144}(SR)_{60}$ cluster samples was done in the Ackerson group following [137]. Pd nanoparticle data were collected at the National Synchrotron Light Source II (beamline XPD, 28-ID-2) at Brookhaven National Laboratory and data for the two cluster samples, $Au_{144}(SC6)_{60}$ and $Au_{144}(SC12)_{60}$ were collected at the Advanced Photon Source (11-ID-B), Argonne National Laboratory. During both beamtimes, data were collected using the rapid acquisition PDF geometry [28] with large-area 2D detectors mounted behind nanopowder samples loaded in, or deposited on, polyimide capillaries and films. Pd NP samples were measured at 300 K with $\lambda = 0.1846$ Å and the two cluster samples were measured at 100 K with $\lambda = 0.1430$ Å.

FIT2D [51] was used to calibrate experimental geometries and azimuthally integrate diffraction intensities to 1D diffraction patterns for all three samples. Standardized corrections are then made to the data to obtain the total scattering structure function, $F(Q)$, which is then sine Fourier transformed to obtain the PDF, using PDFGETX3 [64] within XPDFSUITE [169]. The range of data used in the Fourier transform (Q_{min} to Q_{max}, where $Q = 4\pi \sin\theta/\lambda$ is the magnitude of the momentum transfer on scattering) was tuned per sample to give the best trade-off between statistical noise and real-space resolution, and also to truncate low-Q scattering unambiguously originating from organic species in the sample. For Pd NPs a range from $2.0 \leq Q \leq 26.0$ Å^{-1} was used, and for the cluster samples ranges of $0.8 \leq Q \leq 27.0$ Å^{-1} and $0.8 \leq Q \leq 26.0$ Å^{-1} were used for $Au_{144}(SC6)_{60}$ and $Au_{144}(SC12)_{60}$, respectively.

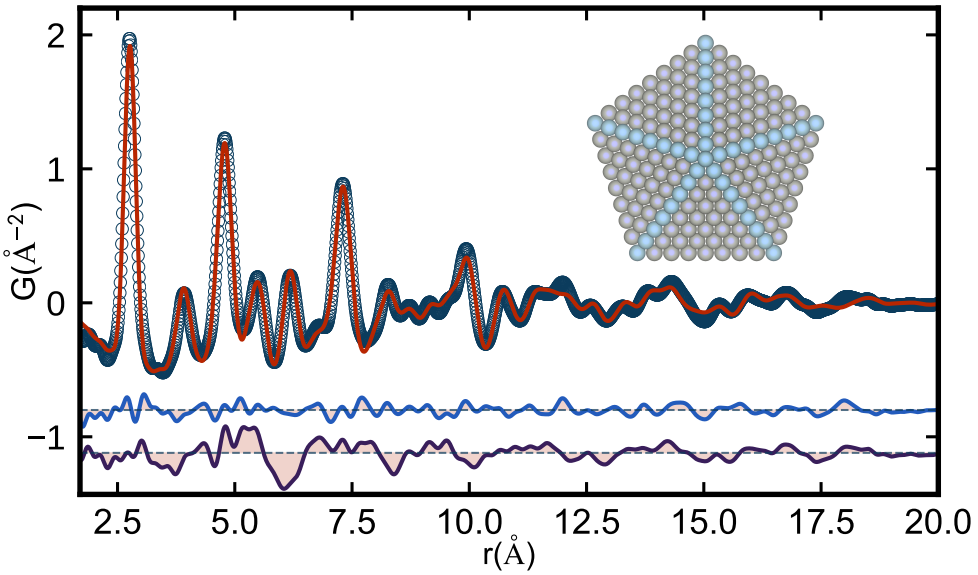

Figure 4.1: Experimental PDF (open circles) from ∼3 nm Pd nanoparticles and the calculated PDF (red solid line) from a 3.6 nm decahedron (inset). Offset below are the difference curves from the discrete decahedral (blue) and spherically attenuated (AC) fcc crystal model (dark purple) refined to the measured Pd NP data.

4.3 Results

We first applied our cluster-mining approach to a PDF measured from ∼3 nm Pd nanoparticles that were described in [15]. In that work, the best cluster model that was found was a 609 atom regular decahedron with a maximum inter-vertex distance of 36.4 Å. This was determined by trial-and-error testing of a regular decahedral size series, starting with a 22.8 Å (181 atom) decahedron, and ending with an 51.9 Å (1442 atom) decahedron. The refinement of the best-fit decahedral cluster core for the small Pd nanoparticles (NPs) is given in Fig. 4.1, which shows the experimental nanoparticle PDF and the calculated PDF for the 609 atom decahedron, with the cluster structure reproduced in the inset. The difference curves (fit residuals) for both the discrete cluster and fcc attenuated crystal (AC) models are offset below in blue and dark purple, respectively.

In [15] it was demonstrated that a diversity of small, representative clusters from motifs with different domain structures and morphologies were needed to fit all the metallic nanoparticle PDFs that were considered. However, it is a laborious task to find the best cluster models, and it would also be valuable to know about the degeneracy of the solution set: how many different clusters give comparable agreement with the data. To do this we can construct libraries, or mines, containing hundreds to thousands of discrete cluster models. These were built combinatorially from motif-specific structure builders as described in Section 4.1. To demonstrate what can be learned from this approach we applied it to the measured PDF from Pd nanoparticles shown in Fig. 4.1 by generating and fitting 464 different discrete models. We start by investigating 60 clusters from a single structure motif (fcc) in greater detail. The results are summarized in Fig. 4.2 which shows the best-fit agreement factor of each fcc model plotted vs. the number of atoms in the model (N_a), which we call a cluster-screen map. We compare the cluster-mined solutions to that from the fcc AC model, which is the benchmark for refinements carried out in the traditional way using PDFGUI. For this Pd nanoparticle sample, the AC model resulted in an $R_w = 0.253$, and this value is shown as a solid teal circle in Fig. 4.2. This fit was obtained with a refined spherical particle diameter (SPD) of 19.4 Å, which corresponds to $N_a \sim 225$ for a discrete fcc spherical cutout. Next we built discrete spherical fcc cutouts to compare to the AC model. These are shown as solid green circles with a dashed outline in Fig. 4.2. This family of clusters has R_w's that follow a trend with nanoparticle size. The trend goes through a minimum at a particle size containing $N_a = 225$, the same as the AC model.

Somewhat surprisingly, the R_w of this model was lower than that of the AC model, though both correspond to spheres of fcc material. There are a number of differences between calculating the PDF of a spherical particle using a discrete spherical cluster and the Debye scattering equation (DSE) vs. a bulk model attenuated with the characteristic function of

a sphere. One of the largest factors to affect the R_w appears to be the choice of Q_{min} used in the DSE calculation. This strongly influences the baseline in the PDF [38] depending on the degree to which the small angle scattering signal is incorporated into the measured and calculated PDFs. Understanding this effect in detail is beyond the scope of this paper, but tests on this Pd nanoparticle sample showed that the best R_w factors were obtained when the same Q_{min} was used for the DSE calculations as was used in the treatment of the measured data. We note that this careful study of spherical nanoparticle models yields insight into how the different cluster models work with the data, and improvements in fit are possible over the AC model, but as was pointed out in [15], the spherical models do not remove much of the signal from residuals and are still deficient in many regards.

We now turn to models with the same fcc atomic structure, but which are cut out from the bulk with well-defined surface faceting. The clusters considered here were made by forming octahedral shapes exhibiting {001} and {111} facets. Three families of faceted fcc octahedra are shown in Fig. 4.2: regular octahedra (solid diamonds) with only {111} facets exposed, truncated octahedra (hexagons) with a mixture of {111} and {001} surfaces, and cuboctahedra (solid hexagons) which satisfy a specific truncation condition where the percentage of the surface covered by {001} (non close-packed) facets is largest and all facet edges contain the same number of atoms. The cuboctahedral family of clusters has the most isotropic or "spherical" shape from the octahedral motif. There are subtle variations in the R_w trends for each of the faceted fcc octahedral families with the cuboctahedral series following most closely the results of the discrete fcc spheres. Regular and truncated octahedra follow trends that are offset slightly below the spherical and cuboctahedral series. Overall, the fcc cluster families track very closely with each other, reaching R_w minima in the vicinity of $N_a \sim 250$ and in fact, the best candidate faceted octahedron is a slightly truncated cluster with 225 atoms, which has the same N_a as the best fit discrete fcc sphere

and AC approximation. In the inset of Fig. 4.2 we compare the fit residuals between the fcc AC model and the (a) minimum R_w fcc sphere and, (b) faceted octahedron, respectively. Although improvements are seen in R_w, it is clear that the majority of the misfit signal in the residual is not affected. This suggests that collectively, monocrystalline fcc cluster cores regardless of shape, might not be the most suitable structure motif for the small Pd NPs studied here. Next, twinned cluster models from decahedral, icosahedral, and singly-twinned structure motifs were constructed and added to the mine and compared to the Pd nanoparticle data. In Fig. 4.3 we reproduce the same R_w scatterplot as discussed for fcc cutouts in Fig. 4.2 with each point appearing as green symbols. The blue symbols are from 398 different decahedral structures including regular decahedra (pentagonal bipyramids), Ino decahedra, Marks decahedra, and Ino-truncated Marks decahedra (see the Methods section for additional details). The red symbols are from icosahedral structures, and the teal symbols (hexagons) are from singly-twinned fcc bicrystals. 55% of the decahedral models tested are in better agreement with the measured Pd nanoparticle PDF than the best fit faceted fcc octahedron. This can be seen as many of the blue symbols are at lower R_w values than the lowest green symbol in the cluster-screen map.

The best candidate decahedral models for the Pd NP data turn out to be from a family of pentagonal bipyramids. The R_w points from this family are outlined with red pentagons in Fig. 4.3. These clusters increase in diameter, or maximum intervertex distance, as a function of N_a and reach a minimum $R_w = 0.121$ for a decahedron with 609 atoms and diameter of $\sim$3.6 nm, which is nearly twice the size of the best fcc model and contains $\sim$270% more atoms. This diameter for the 609 atom decahedron is much closer to the TEM estimated particle size of 3.0 $\pm$ 0.3 nm for the Pd NPs investigated here. The TEM estimate is not a full sample average, and is a slight underestimate of the average particle size. This may be because the TEM estimate is averaging over particles viewed from different directions,

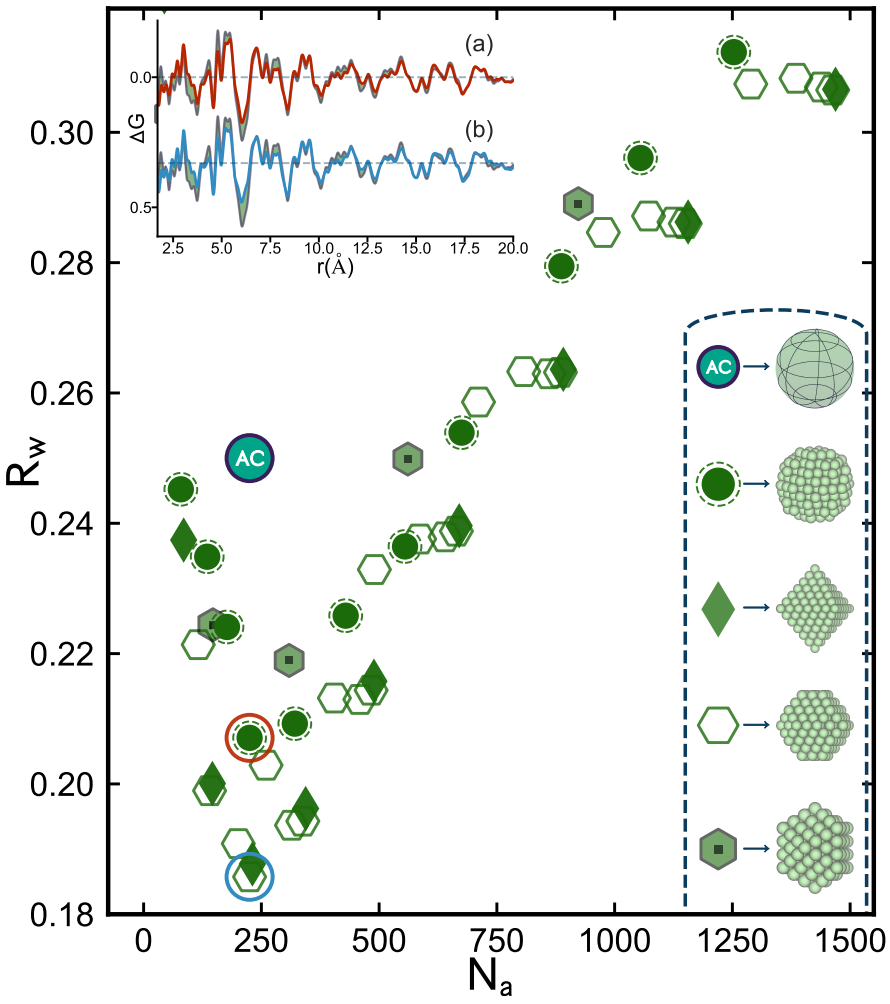

Figure 4.2: Scatter plot of agreement factors (R_w) for discrete fcc clusters fit to the Pd nanoparticle PDF, plotted as a function of the number of atoms per model (N_a). Each point is an individual PDF refinement of a discrete structure from a different fcc cluster type. These have been categorized as different families (see Section 4.1 for details) which are represented in the legend at the bottom right. From top to bottom, the five families from the fcc motif shown here are AC, discrete spheres, regular octahedral, truncated octahedral, and cuboctahedral. In the scatter plot, the AC model fit is marked as a solid teal circle, and the best fit model from the discrete spherical and truncated octahedral families are highlighted with red and blue circles, respectively. In the inset to the top left, the PDF fit residual from the AC model (light purple) is overlaid with the difference curves from the aforementioned best fit discrete sphere (a), and octahedral clusters (b), using the same colors as highlighted in the scatter plot.

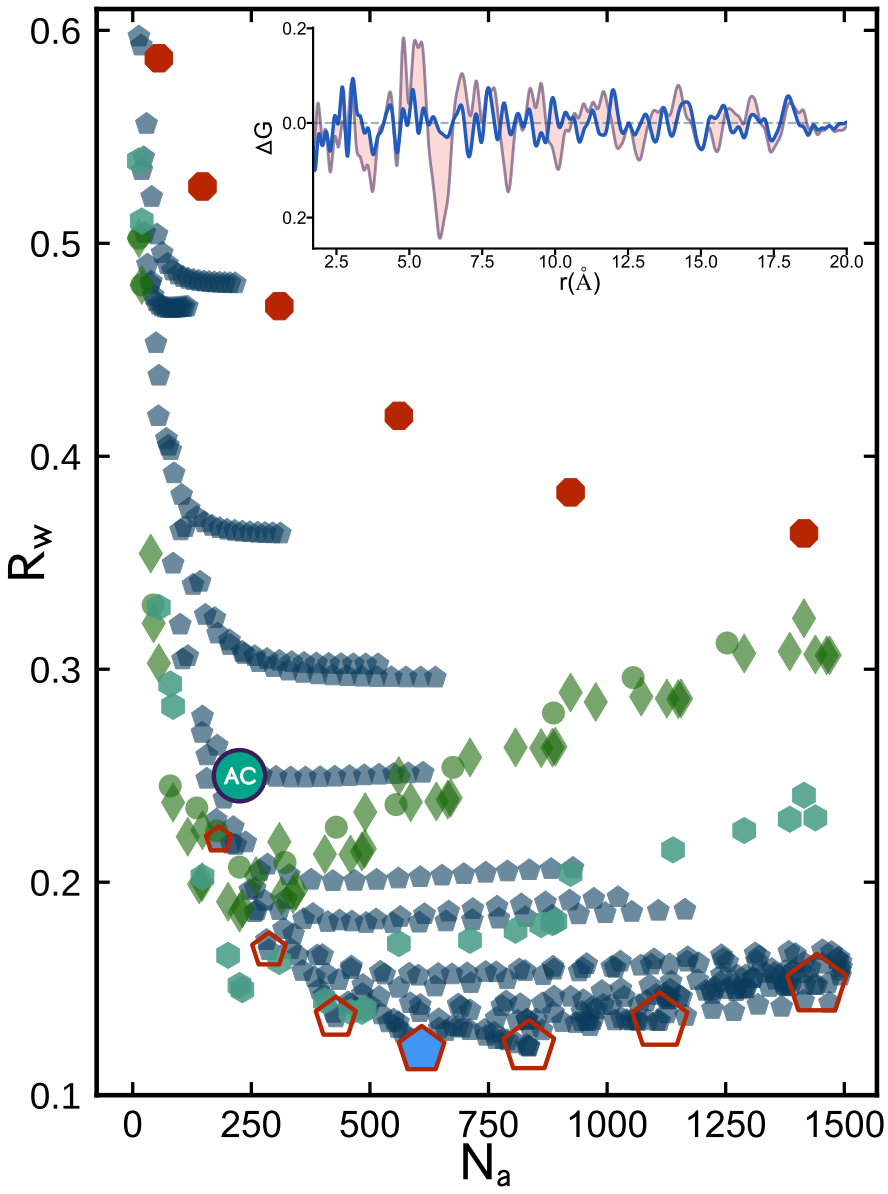

Figure 4.3: Scatter plot of agreement factors (R_w) for discrete clusters from three different structure motifs fit to the Pd NP PDF, plotted as a function of the number of atoms per model (N_a). Green diamonds and circles are for the fcc motif and include the faceted and spherical cluster families shown in Fig. 4.2. Red octagons are for Mackay icosahedra, teal hexagons are for singly-twinned fcc bicrystals, and blue pentagons are for different decahedral families (see text for details). The best fit AC model is marked as a solid blue circle. Red pentagons outline a size series of regular decahedra (pentagonal bipyramids). In the inset, the PDF fit residual from the AC model (light purple) is overlaid with the difference curve from absolute best-fit cluster model, which in this case is the 609 atom non-truncated decahedron (Inset Fig. 4.1).

and the particles are somewhat oblate in shape. The shape of this 609 atom decahedron (Fig. 4.1 inset) also aligns with the observation of oblate-like morphologies in HRTEM images of these Pd NPs [15]. In general, combined imaging and sample average estimates of particle are preferable for building a full picture. Most convincingly, in comparing the fit residual from the fcc AC model and the best fit decahedron (Fig. 4.3 inset) we observe drastic changes to the largest amplitude features in the difference curve, with many of the misfit correlations removed altogether, which strongly supports the idea that the decahedral cluster core is capturing the correct modification to the fcc structure. The ability to determine nanoparticle structure and morphology in such detail can be expected to yield insights into questions such as the mechanisms governing nanoparticle formation and stability [140] through systematic studies of well controlled nanoparticle systems under different growth conditions, for example.

It is often discussed in the literature that the range of r where features are seen in the PDF corresponds to a "range of structural coherence" or a "crystallite size" but this modeling shows how such a situation may come about. The observed PDF structural coherence range is roughly the size of one of the five fcc sub-domains that make up the decahedral cluster. This is an exemplar case where a model of a much larger cluster, which accounts for the inter-domain structure and domain twin boundaries, produces a significantly better fit to the PDF than just a model of incoherent small grains of fcc material and provides an illustration of how rather small nanoclusters may consist of sub-domains in general. The other cyclic-twinned motif tested in Fig. 4.3, magic icosahedra (red markers), yield R_w's that are significantly worse than both the fcc and decahedral motifs, which shows that despite containing a high density of contact twin boundaries, the spatial arrangement of these domains is not representative for this Pd NP sample, and the icosahedral motif can be easily ruled out. On the other hand, singly-twinned fcc bicrystals follow a trend that is intermediate between the single crystal fcc cutouts, and the best candidate decahedral models, which

makes sense given that the density of atoms on twin planes is also intermediate between the two. However, the best fit singly-twinned clusters are still significantly smaller than than the family of pentagonal bipyramds (red pentagons in Fig. 4.3) and the comparative difference in R_w increases as a function of N_a. This might suggest that the average nanoparticle contains both well-defined cyclic twin interfaces and lamellar twin boundaries within the subdomains, or that distinct populations of smaller singly-twinned clusters and larger decahedral clusters exist within the same sample.

We now apply cluster-mining to a series of ultra-stable magic sized $Au_{144}(SR)_{60}$ clusters [165] prepared with different thiolate ligands [3, 137]. In Fig. 4.4(a) we show the cluster-screen map from one sample in this series consisting of hexanethiol ligated clusters, $Au_{144}(SC6)_{60}$. In this case, icosahedral structures perform better than the AC, fcc octahedral, and decahedral motifs. The best fit model obtained is a 55 atom Mackay icosahedron with $R_w = 0.228$, highlighted with an orange outline in the cluster-screen map, Fig. 4.4(a). In Fig. 4.4(b) we show the PDF of the best-fit cluster-mined 55 atom core. The difference curve is offset below and overlaid on the difference curve from the fcc AC approximation. The main misfit in the AC difference curve between 5 and 8 Å is drastically improved, and no other clusters are close in agreement, giving us confidence that the core of this Au_{144} cluster is icosahedral in nature.

In this case, a structure solution for $Au_{144}(SC6)_{60}$ has been found by DFT, HAADF-STEM and PDF [89, 12, 59]. In Fig. 4.4(c) we show the PDF from the 144 atom Lopez-Acevedo (LA) model, which contains chiral arrangements of atoms on top of a core that is nearly identical to a Mackay icosahedron [59, 15]. The additional lower symmetry outer layers of the LA model further remedies the misfit features at higher-r (Fig. 4.4(c)) and improves the overall agreement factor to a value of $R_w = 0.146$. This highlights the fact that cluster-mining can also identify good candidate cluster cores, which can be used as starting

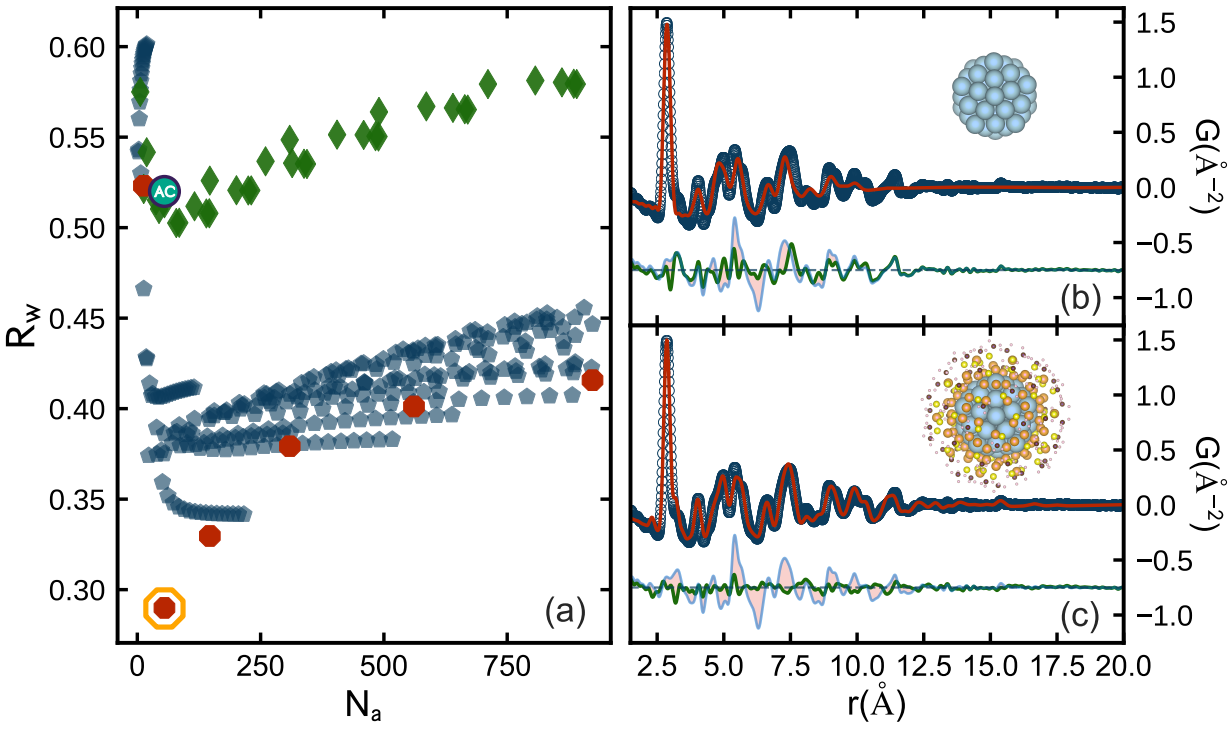

Figure 4.4: (a) Cluster-screen map for $Au_{144}(SC6)_{60}$ including structures from AC (teal), fcc octahedral (green), decahedral (blue) and icosahedral (red) motifs. The best-fit cluster core, a 55 atom Mackay icosahedron is outlined in orange. (b) Measured PDF (open circles) from the $Au_{144}(SC6)_{60}$ cluster sample and the calculated PDF (red solid line) from the cluster-mined 55 atom Mackay core (shown in inset). The difference curve from this refinement is offset below in green, and overlaid with the AC residual in light blue. (c) Analogous to (b), except the calculated PDF (red solid line) is from a DFT derived structure solution [89] for $Au_{144}(SC6)_{60}$ which shares the icosahedral core shown in (a), and also contains lower symmetry outerlayers. In the inset, the radii of atoms surrounding the DFT determined core are scaled down by a factor of 2 for illustration.

structures for more complex core/shell models.

Not all samples are ideally single phase, and we would like to know how robust the cluster-mining approach is in the case where more than one phase exists in the sample. This can be tested using a $Au_{144}(SR)_{60}$ sample where a different thiolate ligand, dodecanethiol (SC12), was used to prepare the clusters. This sample was shown to consist of both icosahedral and decahedral cores with the decahedral phase fraction being $\sim$14% [59]. The resulting cluster-screen map is shown in Fig. 4.5. The cluster-mining methodology is stable, resulting in a cluster-screen map that is largely similar to the pure, single-phase icosahedral SC6 sample shown in Fig. 4.4(a). It yields the 55 atom Mackay core as the best candidate cluster which is consistent with the expected majority phase, but the cluster-screen map also shows that the R_w trends for icosahedral and decahedral clusters have changed, with the two motifs reaching minima much closer to one another compared to the single-phase case. This behavior may be characteristic of nanoparticle mixtures. In the future we will explore extending cluster-mining to quantify minority phases in multi-phase samples.

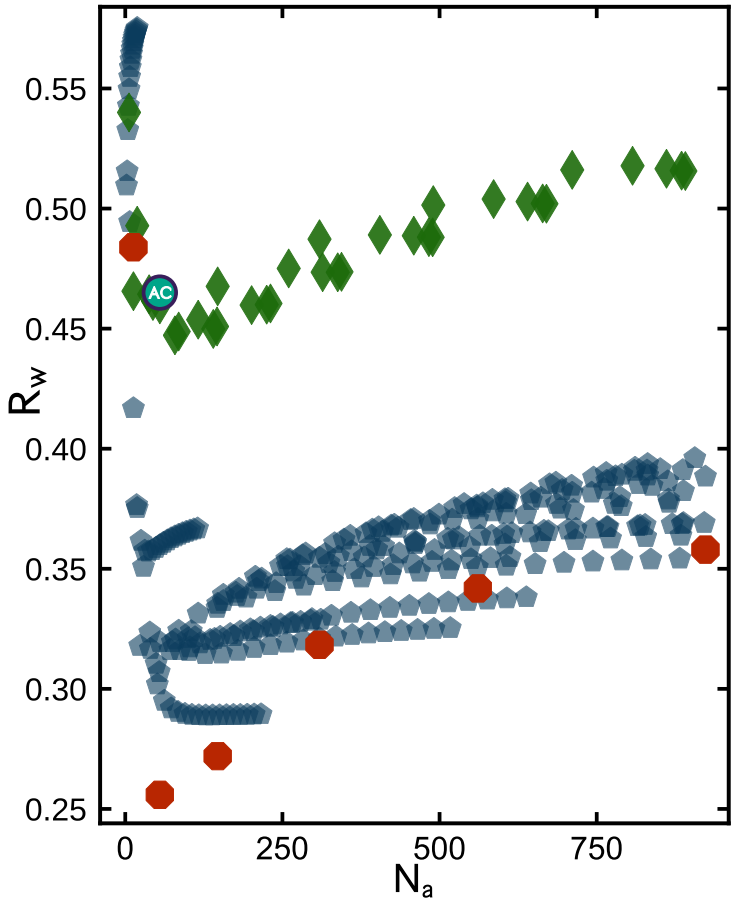

Figure 4.5: Cluster-screen map for a multi-phase cluster sample, $Au_{144}(SC12)_{60}$. The cluster-mine includes AC (teal), fcc octahedral (green), decahedral (blue) and icosahedral (red) motifs.

Chapter 5

Quantitative structural characterization of faceted TiO_2 nanoparticles

Titania-based materials find widespread uses as photocatalysts, catalysts, solar cells, and biocompatible implants. Their utility depends on a combination of surface, electronic, and bulk structural properties. Our group has been interested in characterizing the properties of nanoparticulate TiO_2 in order to rationally design catalysts for a range of applications.

P90 and P25 are commercial pyrogenic titania nanoparticles (NPs) that contain a mixture of rutile and anatase phases. They are synthesized from vaporized $TiCl_4$ at temperatures between 1000 and 2400 °C, a process referred to as pyrogenesis or fuming. Per the manufacturer, the resulting TiO_2 NPs are 85-90 % anatase by weight, with the rest rutile. The particles are tightly bound to other particles to form aggregates, which enable the material to be distributed as powder or granulates. Numerous researchers have noted that pyrogenic TiO_2 have properties that are quite different from the properties of either anatase

or rutile. Hurum *et al.* [55] suggests that P25 contains unusually small rutile crystallites "interwoven" with anatase crystallites, and that this interwoven connection facilitates rapid transfer of electrons from rutile to anatase. Rutile is therefore able to serve as an antenna or photosensitizer to extend the effective anatase band gap to longer wavelengths.

We have recently shown that pyrogenic TiO_2 outperforms other forms of TiO_2 in Ru/TiO_2 catalysts used to hydrodeoxygenate phenol, and much more closely resembles the properties of rutile titania than anatase titania, despite being mostly anatase. [94] Earlier work speculated that P25 might contain particles with a core of anatase overlaid with a shell of rutile [20], a structure that would be consistent with the catalytic results we obtained. While more recent papers refute the core/shell characterization, a careful review of the literature points to lingering controversy over the structure of pyrogenic TiO_2 and the need for additional characterizations. [104, 31]

In this work, we present the first detailed PDF analysis of P90 and P25, supported by x-ray diffraction (XRD) and transmission electron microscopy (TEM) measurements and referenced to recent diffuse reflectance infrared Fourier transform spectroscopy (DRIFTS) and density functional theory (DFT) calculations [93] on the same materials. This shows the importance of structural and morphological characteristics to the properties of the pyrogenic titania. PDF techniques yield complementary information to conventional XRD and TEM such as quantifying the morphology and faceting of the titania nanoparticles in these samples. Our quantitative full profile refinements of the PDF data yield more reliable structural parameters than the single peak phase quantification and Scherrer analyses or lab source Rietveld methods in the current literature. [105, 115, 154, 116, 30, 163] By careful benchmarking and model validation we demonstrate that PDF can be used to extract accurate, sample-average information about the crystallographic phases in these nanoparticle mixtures and, furthermore, the nature of their highly faceted morphologies. This lays the ground work

for future studies on the relationships between atomic structure, shape, and reactivity.

5.1 Experimental Section

5.1.1 Materials

TiO_2 P25 (Evonik), TiO_2 P90 (Evonik), TiO_2 rutile (US Research Nanomaterials), TiO_2 anatase (Sigma Aldrich), were all purchased from their respective manufacturers. 200 mesh Cu TEM grids and silicon nitride grids were purchased from Ted Pella Inc. (Redding, CA). A 90% anatase, 10% rutile mixture was prepared by physically mixing pure anatase and rutile by weight %.

5.1.2 X-Ray diffraction (XRD)

XRD experiments were used to identify the phases present in the powders. These experiments were carried out at the Shared Materials Characterization Laboratory (SMCL) of the Columbia University Nanoinitiative (CNI) at Columbia University using the PANalytical Xpert3 theta-theta Powder x-ray diffraction (XRD) instrument equipped with Cu Kα radiation. The operating voltage was 45 kV and the current 40 mA. The experiments were conducted in the Bragg-Brentano geometry and a zero-background quartz holder was used to minimize the background signal and eliminate reflections from the holder. The two-theta angular range for the scans was 20-100°. The scan step size was 0.1° and the dwell time 1 second per step. For the incident beam, a 15 mm mask and 0.5° divergence and 1° antiscatter slits were employed. For the diffracted beam, the 0.5° antiscatter slit was used. The powder samples were mixed with 2-propanol to allow for ease of placement in the sample holder.

5.1.3 Transmission Electron Microscopy (TEM)

Conventional and high-resolution TEM were performed at the Columbia Nano Initiative (CNI) electron microscopy facilities using an FEI Talos F200X transmission/scanning transmission microscope. The analyzed catalysts were mixed with a minimal amount of 2-propanol and the mixture was suspended on either a lacey carbon film, a Cu grid, or a silicon nitride membrane grid with a membrane thickness of 50 nm, frame width of 50 μm and nine 0.1 mm x 0.1 mm windows. The operating voltage of the FEI Talos was 200 kV. HRTEM imaging was done using the 60 μm objective aperture to include the first diffracting planes of both rutile and anatase ($\{110\}_R$ and $\{101\}_A$) and to achieve higher imaging contrast. Identification of specific TiO_2 particles in the HRTEM image was done by filtering the respective atomic plane periodicity of each phase in fast Fourier transforms (FFT) of the images. Selected area electron diffraction patterns were used to determine the phases present in larger populations of particles compared with the HRTEM images. It was seen that prolonged exposure to the electron beam resulted in amorphization of the particles, and, therefore, in the results presented here, care was taken to minimize the imaging time. Additionally, it was found that the carbon layer in the holey carbon grids was not fully amorphous, making it difficult to unambiguously distinguish the particles from the supporting carbon layer. As a result, the silicon nitride membrane grids were used when there was a need for obtaining the clearest images of the particles.

5.1.4 PDF

Total scattering x-ray measurements were done at the National Synchrotron Light Source II (XPD, 28-ID-2), Brookhaven National Laboratory. Five nanocrystalline TiO_2 samples were measured: anatase, rutile, P90, P25, and a physical mixture containing 90% anatase + 10%

rutile by weight fraction. Powder samples were sealed in polyimide capillaries and diffraction patterns were collected at room temperature using the rapid acquisition PDF geometry [28] with an x-ray energy of 67.57 keV (λ = 0.1835 Å) using a large-area 2D Perkin Elmer detector. The detector was mounted with a sample-to-detector distance of 204.54 mm. The experimental geometry, 2θ range, and detector misorientations were calibrated by measuring a crystalline nickel powder directly prior to the titania nanocrystals, with the experimental geometry parameters refined using the Fit2D program [51]. Standardized corrections were made to the data to obtain the total scattering structure function, $F(Q)$, which was then Fourier transformed to obtain the PDF, using PDFgetX3 [64] within xPDFsuite [169]. The maximum range of data used in the Fourier transform (Q_{max}, where $Q = 4\pi \sin\theta/\lambda$ is the magnitude of the momentum transfer on scattering) was chosen to be 20.0 Å^{-1} to give the best tradeoff between statistical noise and real-space resolution.

Though larger Q-ranges were accessible for four of the samples, P90, measured during the same beamtime, had considerably more diffuse scattering at high-Q. Masks were created to remove outlier pixels and to optimize the Q-ranges as much as possible using an automasking procedure [166] and applied to the images before azimuthal integration in pyFAI [67]. For consistency, all five PDFs were transformed with the same settings. See Fig. 5.12 in Section 5.7 for a comparison of the Bragg scattering data and $F(Q)$.

PDF structure refinements of pure and mixed TiO_2 samples were first carried out using PDFgui.[39] The structure models used were rutile (SG: $P4_2/mnm$) and anatase (SG: $I4_1/amd$) as shown in Figure 5.1 (a, b). The rutile unit cell contains two TiO_2 units and anatase contains four units, but is less dense than rutile, and the TiO_6 octahedra are more distorted. Structure models were obtained from published crystal structures of bulk anatase and rutile. [53, 16] For rutile (SG: $P4_2/mnm$), O is at the $2a$ $(0, 0, 0)$ site and Ti at $4f$ $(0.306, 0.306, 0)$. In anatase (SG: $I4_1/amd$), O is positioned at $4a$ $(0, 0, 0)$ and Ti at $8e$

$(0, 0, 0.208)$. To account for the finite size of nanocrystalline TiO_2 particles/crystallites, the PDFs calculated from the crystal structures were attenuated using a characteristic function to approximate the nanoparticle morphology. We refer to this approach as attenuated crystal (AC) modeling. Instrumental parameters were obtained by independently refining a bulk Nickel calibrant and then kept fixed ($Q_{damp} = 0.038$, $Q_{broad} = 0.015$) for all nanoparticle fits. For each TiO_2 phase, $a = b \neq c$ lattice parameters were refined with tetragonal constraints, along with one isotropic atomic displacement parameter (ADP) per element (Ti, O), and a parameter to account for correlated motion effects [61] (δ_1) was also refined. [135] Atomic positions were set to literature values [53, 16] and not refined. In the two-phase/mixed AC model, anatase (majority) and rutile (minority) phases were constrained such that the proportion of each phase took values between zero and one.

Discrete structure refinements of faceted anatase models were carried out using the CMI software framework [65]. Unlike the AC modeling approach, here PDFs were calculated from models expressed in cartesian coordinates using the Debye scattering equation [33], implemented in DIFFPY's DEBYEPDFGENERATOR class under SRFIT. The atomic coordinates were held constant and five parameters were allowed to vary in the PDF refinement: an isotropic expansion coefficient, two isotropic ADPs (one per element), a global scale factor, and δ_1. The discrete anatase models were constructed using a simple cookie-cutting method in VESTA.[108] First the unit cell refined from the AC anatase model was tiled in space to create a tetragonal supercell where the minimum dimension was made to be $\geq$ the AC refined crystallite diameter. The morphology was then tuned by specifying the Miller indices of anatase surface facets, and generating all symmetry equivalent lattice planes commensurate with the dimensions of the supercell. The surface area ratios between different facets were scaled by changing the relative distances of the facets from the origin of the supercell. The discrete atomic coordinates for each shape were extracted from the supercell by defin-

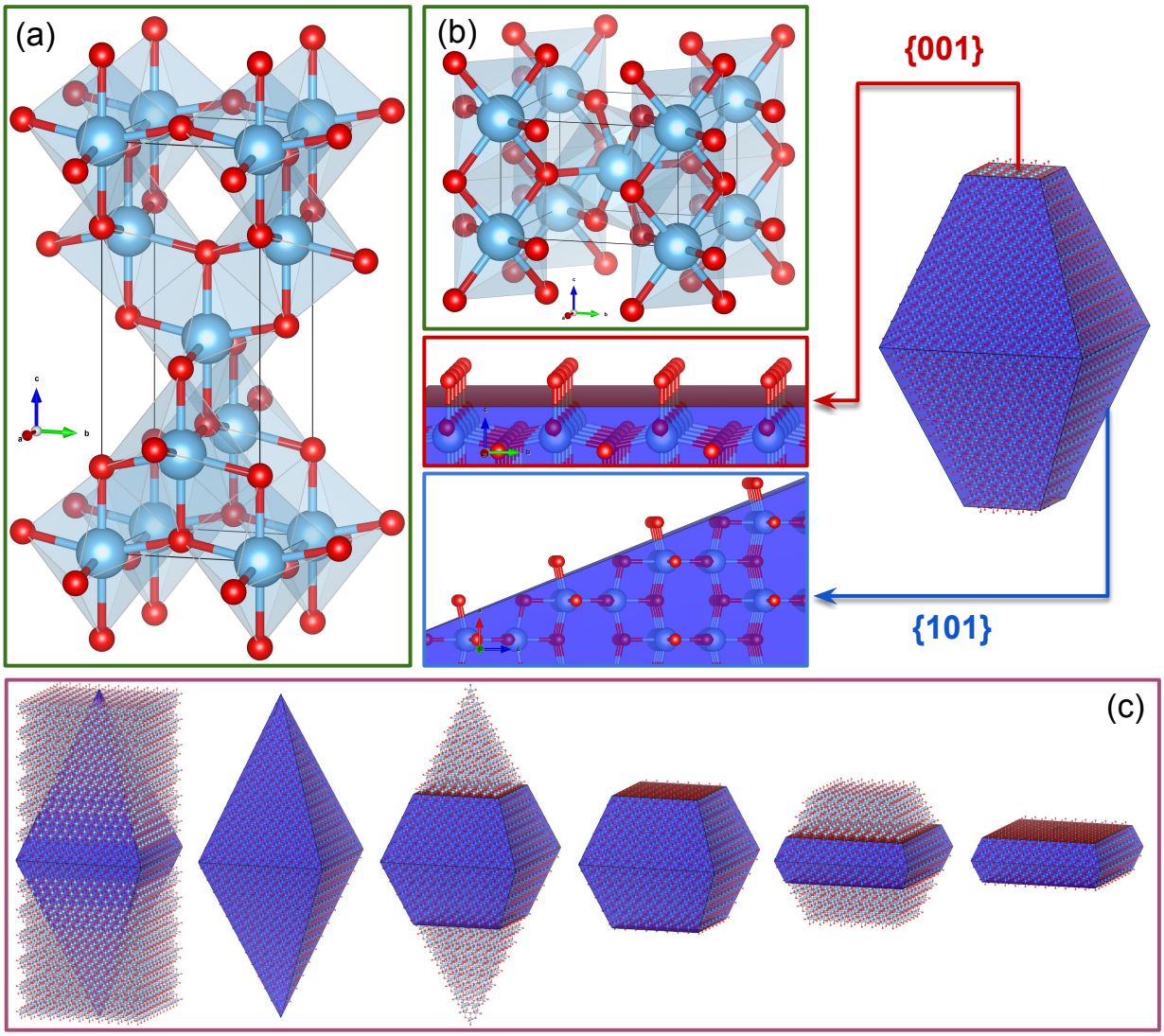

Figure 5.1: (a): anatase unit cell (b): rutile unit cell. Titanium atoms are shown in blue and xxygen in red. Both tetragonal TiO_2 crystal structures are formed from distorted chains of TiO_6 octahedra (shaded light blue in both unit cells). Right inset: an example of a bipyramidal morphology for anatase with a magnified view of the {001} terminated surface in anatase. The red plane defines the boundary of the surface, where Ti atoms below the plane are undercoordinated with only five nearest O atoms. The corrugated {101} anatase facet with a mixture of five and sixfold coordinated Ti atoms is annotated in blue. (c) An illustration of how shape tuned atomistic models were generated from large anatase supercells.

ing cutoff boundaries at the facet limits, illustrated in Figure 5.1(c). For the large anatase cutouts used in this study, we constrained the number of atoms in each model to be similar (24100±100 atoms) so that the comparisons would be most sensitive to morphological differences. For both AC and discrete structure refinements, the agreement between simulated PDFs and data were quantified by the residual, R_w. [39]

5.1.5 XRD

Figure 5.2 shows x-ray diffractograms in the angular range of 20-60° for samples of anatase, rutile, P90, P25, and a 90:10 physical mixture of anatase and rutile. The presence of both anatase and rutile in P25, P90 and the physical mixture is clearly evident. The pure TiO_2 samples are indexed and show good agreement to the expected reflections for pure anatase and rutile phases.

5.1.6 TEM

High-resolution transmission electron microscopy (HRTEM) images of P90 and P25 are not consistent with a core/shell model. These images, an example of which is shown in Figure 5.3 for both P90 and P25, suggest the majority of the particles are pure anatase. Distinct particles of the minority rutile phase, which can be differentiated from anatase by interplanar spacing, are also observed in the images and highlighted in Figure 5.3. The selected area diffraction pattern of P90 and P25 given in Figure 5.4 also clearly evidences the presence of both anatase and rutile as distinct phases. The diffraction spots for rutile are distinguished from the diffraction spots/rings for anatase, as labeled. The two phases have different crystal structures and thus different interplanar spacings. However, since rutile is the minority phase with a significantly lower phase fraction than anatase in the mixtures, only isolated diffraction spots of rutile are seen in the patterns compared to the more complete diffraction

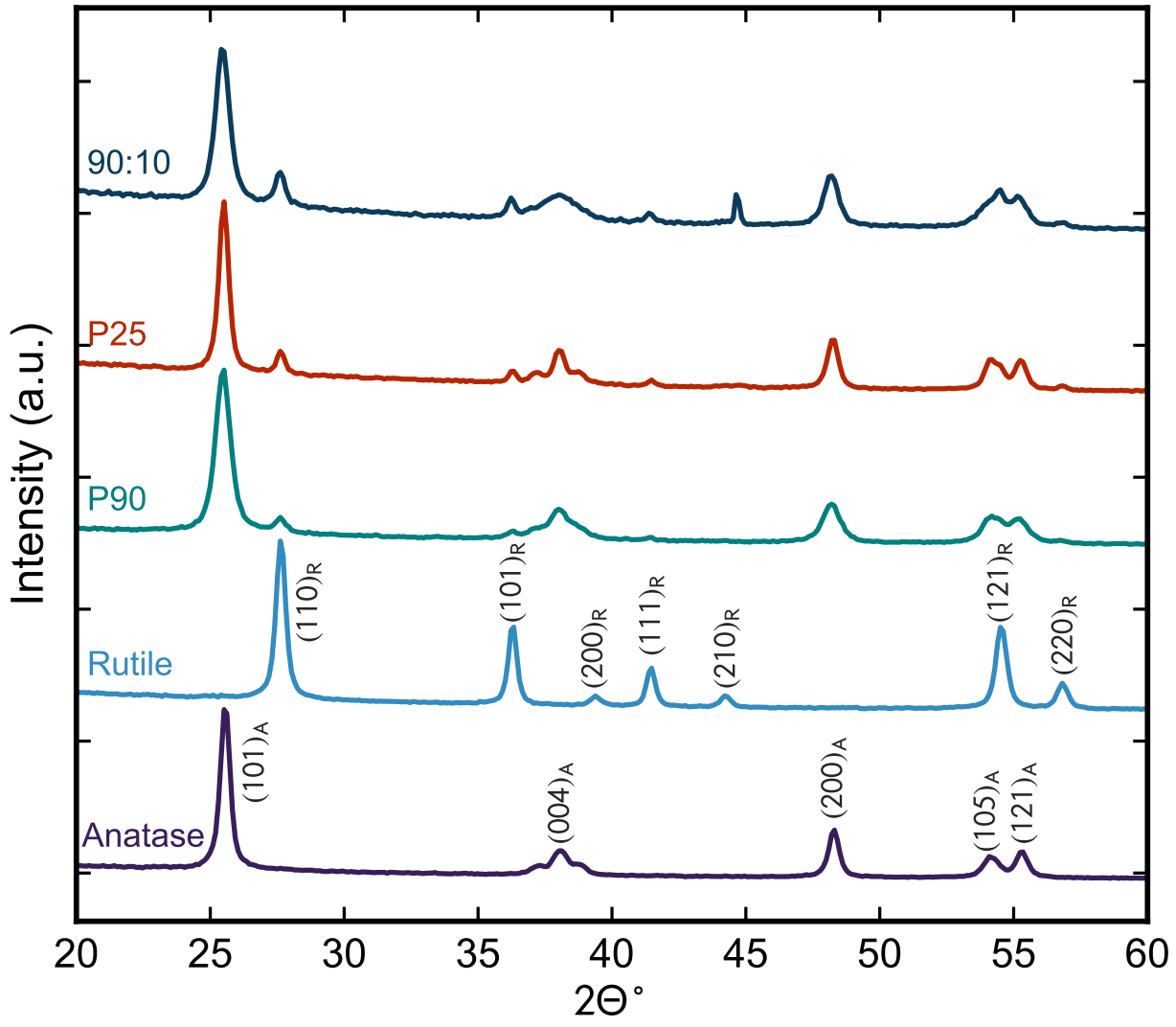

Figure 5.2: X-ray diffractograms patterns for samples of anatase, rutile, P90, P25, and a physical mixture of 90% anatase and 10% rutile (wt.%). The patterns have been displaced for clarity.

rings of anatase. Representative bright-field transmission electron micrographs of all TiO_2 samples used in this study are provided in Section 5.6 and show the sizes and shapes of typical particles (Figure 5.10 and 5.11).

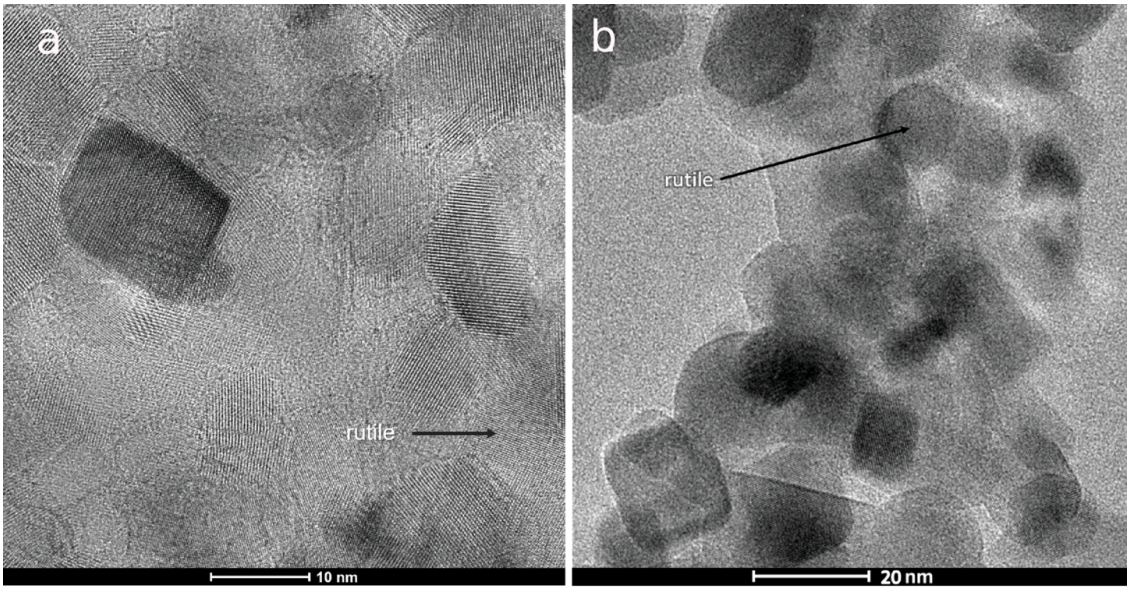

Figure 5.3: HRTEM images showing individual rutile nanoparticles in P90 (a) and P25 (b) that were identified by interplanar spacing.

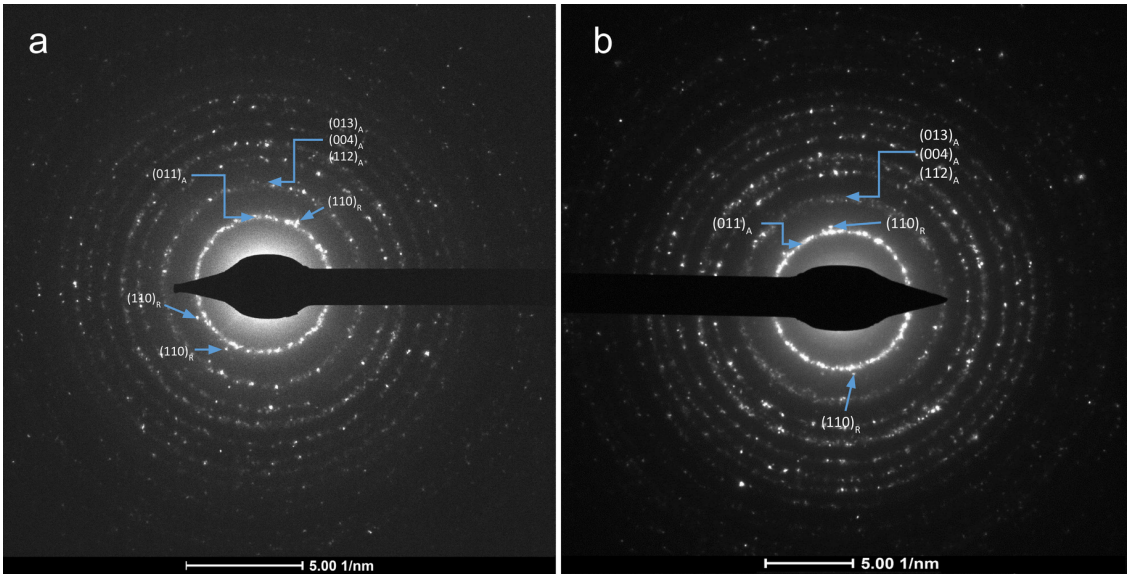

Figure 5.4: Selected area diffraction of P90 (a) and P25 (b), showing clear evidence of the presence of both anatase and rutile phases. The subscripts A and R denote anatase and rutile, respectively.

5.1.7 PDF

This work presents the first PDF characterization of commercial P90 and P25 nanoparticles. The following analysis was done to accurately quantify the nanocrystalline anatase and rutile phases present in these catalysts, and to assess if there is any evidence of tertiary TiO_2 phases or core/shell phase segregation. PDF is a powerful approach to obtain reliable sample-average structural information from nanomaterials [27, 110, 59, 40, 174, 103, 86] and provides insights not readily obtainable by electron microscopy, selected area electron diffraction (SAED) and lab source powder diffraction, all of which have been previously used to characterize pyrogenic TiO_2 nanoparticles.[106, 107, 79, 122, 115, 154, 116, 30, 163]

In order to establish that the PDF is capable of differentiating between the constituent phases of mixed TiO_2 nanomaterials we first analyzed pure anatase and rutile nanoparticles.

Single phase refinements of the pure samples, fit to their respective structure models over a wide r-range ($1.5 < r < 60$ Å), are shown in Fig. 5.7(a-b) and the resulting structural parameters are provided in Table 5.2. It is clear that the single phase models are in good agreement with the crystallographically distinct nanoparticle structures, evidenced by the small amplitude difference curves and low R_w values (agreement factors) for both samples. We also observe a significant disparity in the average crystallite size between the pure rutile and anatase samples. This can be seen qualitatively by the more rapidly decaying signal intensity (as a function of r) for anatase versus rutile, and quantitatively by the refined spherical particle diameter (SPD) which shows that the pure rutile crystallites are, on average, about twice as large as pure anatase. SPDs, or crystallite sizes, were quantified using the AC modeling approach, commonly applied in PDF analysis. [37] Additional details are included in the PDF Methods section.

Next we measured a physical mixture of anatase and rutile nanoparticles with 90% anatase and 10% rutile by weight to simulate the expected phase fraction of the commercial samples. This was fit initially with a pure anatase model. This results in a quantitatively poorer fit, as evident in Fig. 5.7(c) and a considerably worse agreement factor compared to the unmixed samples (ΔR_w=+38%), confirming the presence of unfit signal. By refining a two-phase model of anatase and rutile to the physical mixture, we improve the fit to a similar quality as the single phase fit, as shown in Fig. 5.5(a) and Table 5.1. In the refinement we allowed the phase fraction of each TiO_2 component to vary, which resulted in a mixing ratio of 89:11 (wt. %) anatase:rutile, consistent with the expected value. This demonstrates the PDF is able to detect and quantify the presence of a minority rutile phase in majority anatase nanocrystalline mixtures.

We then examined the commercial TiO_2 P90 sample. As before we tried to fit it to a pure anatase model. This yielded an $R_w = 0.163$, which is worse than we expect for a good

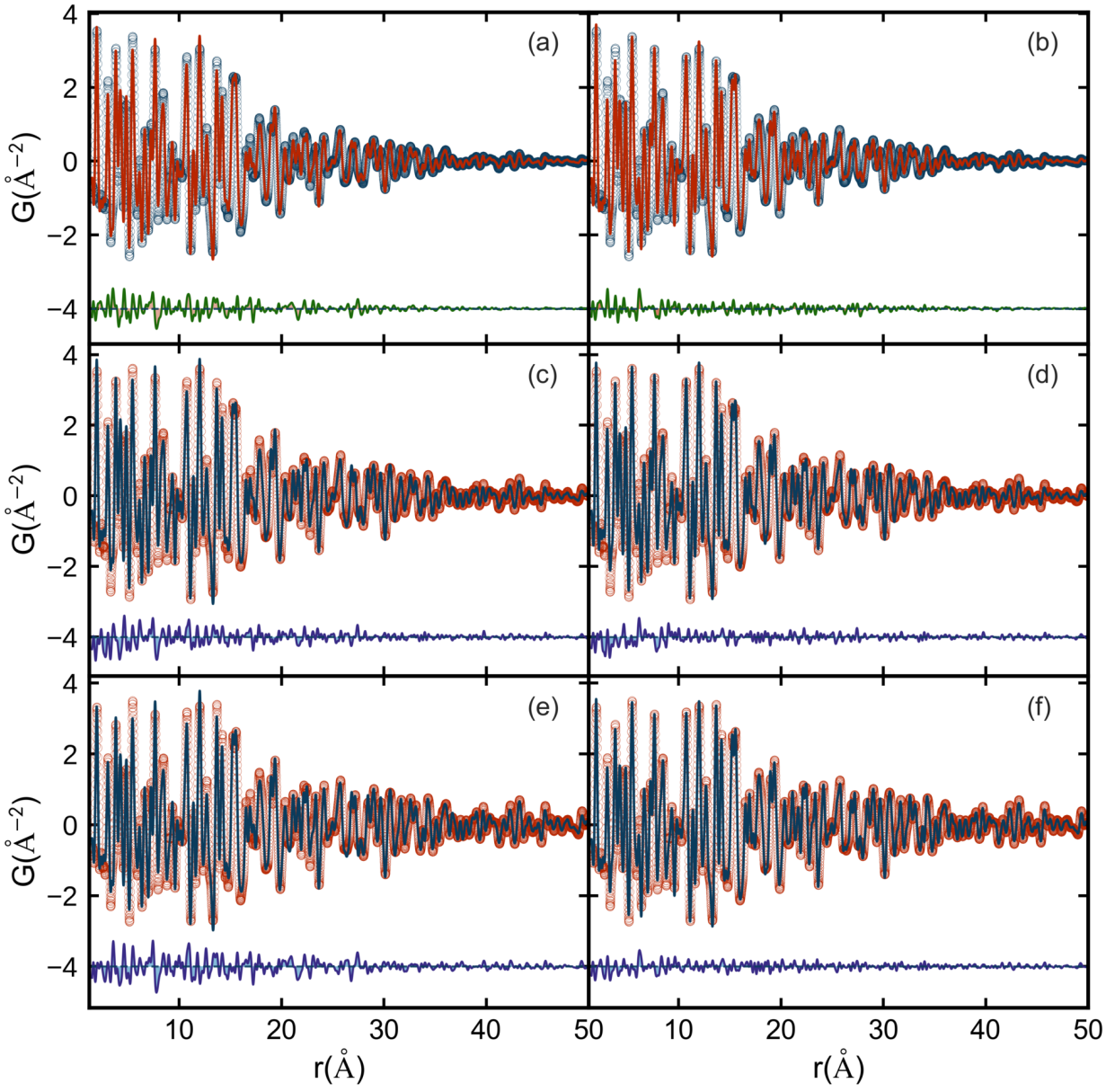

Figure 5.5: Measured (open symbols) and calculated (solid lines) PDFs of mixed phase, P90 and P25 samples. Difference curves are shown displaced below. Experimental PDFs in the left column are fit with a single phase anatase model for (a) the physical nanoparticle mixture of 90% anatase and 10% rutile (wt.%) (c) P90 and (e) P25. In the right column, experimental PDFs are fit with the mixed phase anatase:rutile model for (b) the physical mixture (d) P90 and (f) P25.

Table 5.1: Structural parameters extracted from two phase refinements of mixed TiO_2 samples using Anatase (SG: $I4_1/amd$) and Rutile (SG: $P4_2/mnm$) structure models. Lattice parameters for both tetragonal phases are given as $a = b$ and c. U_{iso}: isotropic atomic displacement parameter (ADP) per element and phase. SPD: spherical particle diameter or crystallite size. R_w: agreement factor. See the PDF methods section for additional details.

Sample	P90		P25		$Mix_{90:10}$	
Fit Phase(s)	Anatase	Rutile	Anatase	Rutile	Anatase	Rutile
%	87.47	12.53	84.65	15.35	88.70	11.30
$a = b$ (Å)	3.786	4.589	3.786	4.592	3.783	4.591
c (Å)	9.492	2.963	9.498	2.960	9.498	2.961
Ti U_{iso} (Å^2)	0.005	0.005	0.004	0.005	0.005	0.005
O U_{iso} (Å^2)	0.013	0.029	0.012	0.025	0.015	0.027
SPD (Å)	87.47	66.33	156.35	130.82	65.85	143.42
R_w	0.129		0.108		0.110	

fit as laid out above. On the other hand, the two-phase anatase:rutile model results in an $R_w = 0.129$ that is slightly higher than, but comparable to the best fits to the 90:10 physical mixture, which serves as a method control. The mixing fraction refined to a 87:13 (wt. %) phase mixture of anatase:rutile, which is similar to the manufacturer's claim and earlier non-PDF characterizations. [107, 105, 105] The results of these refinements are shown in Fig. 5.5(c) and (d) with extracted parameters from mixed phase fits reproduced in Table 5.1 and single phase fits in Table 5.2. We also carried out a similar analysis on the commercial P25 sample and found it to be a 85:15 (wt. %) phase mixture of anatase:rutile; fits are shown in Fig. 5.5(e,f). The agreement to the mixed phase model is as good as the physical mixture, with an $R_w = 0.108$, a clear improvement from the single phase fit shown in Fig. 5.5(e), further supporting that the two-phase model is appropriate for all three mixed phase TiO_2 samples. Refined parameters for P25 are given in Table 5.1. Attempts to fit other structural models for the titania gave poorer fits than the physical mixture which strengthens the view that the sample is a mixture of anatase and rutile nanograins.

We looked closely at the refinements of the physical mixture and the pyrogenic TiO_2 samples to search for any differences. As noted, all of the mixed TiO_2 materials included in this study have similar anatase:rutile phase fractions, with P25 having slightly more rutile, and most other structural parameters are comparable. One structural parameter which does differ significantly between the samples is the relative particle/crystallite size (SPD) of the anatase and rutile components. On average, the anatase particles in the physical mixture are smaller than the anatase and rutile crystallites in P90 and P25. In contrast, while the crystallites are smaller in P90 than they are in P25, for both pyrogenic materials the rutile and anatase crystallites are similar in size. While this result differs from several prior reports, both our PDF and HR-TEM data support this assertion. Refined SPDs are provided for comparison in Table 5.1. The smaller rutile crystallite size, or the comparable relative size of

the anatase and rutile components, may be an important characteristic of pyrogenic titania.

Careful inspection of the fits in Fig. 5.5 suggests that there are some fluctuations left in the residual. It was recently shown [15] that such, albeit small, residual signals that remain after fitting AC models as we have done here, may contain information about particle morphology and defects. We first confirm that these small signals in the residual have a structural origin. In Fig. 5.6(a) we have replotted the best-fit difference curves from the AC model refinements from Fig. 5.5(b,d) directly on top of each other. It is clear that these two difference curves are highly correlated with each other, even though the datasets are from completely different samples, in one case the anatase:rutile physical mixture and in the other case, P90. This implies that these two samples share the same structural modification that is not captured in the attenuated crystal modeling. In Fig. 5.8 we show that this shared structural modification is also present in P25 and in the residual from a single phase refinement of pure anatase. This is a structural modification that is common to all the anatase containing samples.

To explore the structural origin of the residual feature we picked P90 as our representative dataset to study. In Banerjee *et al.* [15] the residual features in metallic nanoparticle signals were explained by building discrete cluster cores with internal twin interfaces. In the current case, we consider possible discrete models that have been suggested for anatase. [32] A Wulff construction may be used to predict equilibrium shapes of crystals based on the surface energies of different facets. [78] The equilibrium Wulff shape for bulk anatase is a slightly truncated bipyramid, with a majority of the surface ($\sim$94%) containing {101} facets, the most energetically stable anatase surface, and a small percentage of {001} facets. In anatase nanoparticles this morphology may be strongly affected by hydroxylation [8] and tuned by using surfactants that preferentially attach to particular lattice planes at the surface, changing the relative energies of the different surface facets, [46] and allowing for different particle shapes.

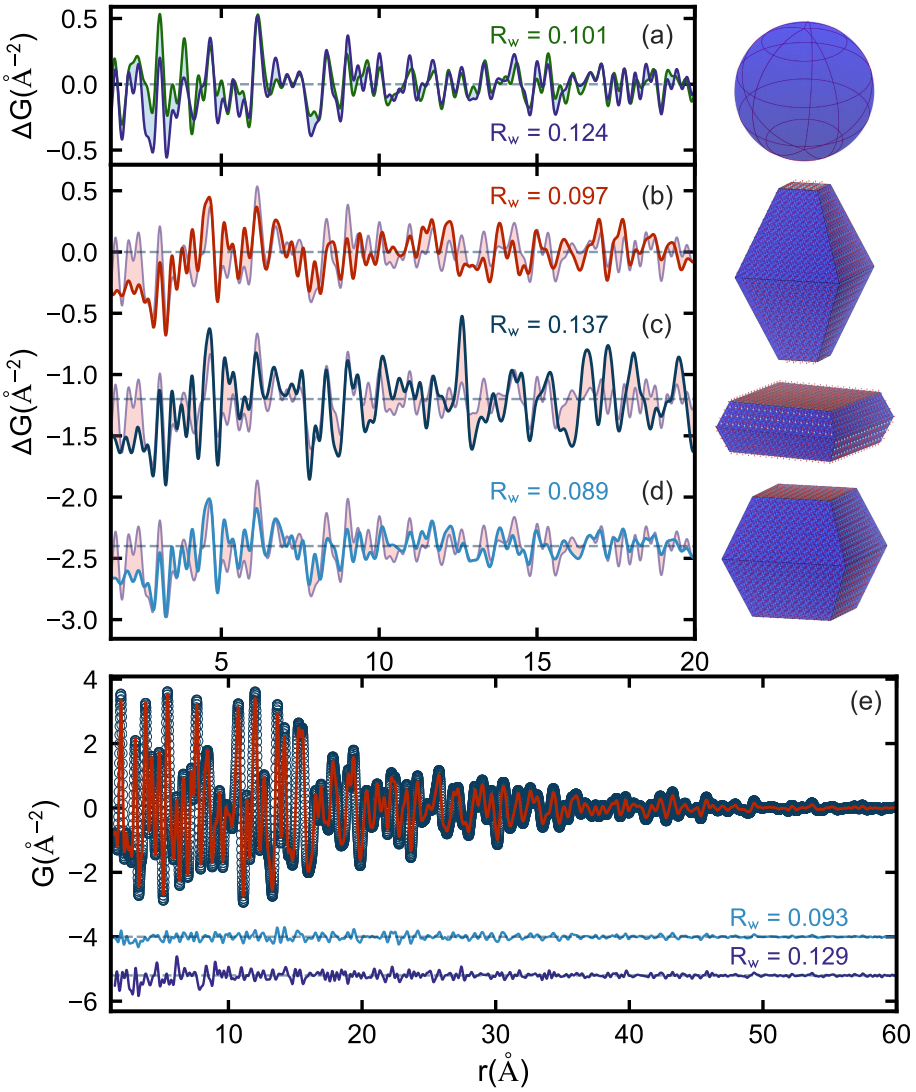

Figure 5.6: Top panel: difference curves (residuals) from the mixed phase AC model refined to experimental PDFs for P90 (purple) and a physical mixture of 90% anatase and 10% rutile (green). Middle panel: difference curves from discrete anatase models with different percentages of {001} surface facets (a) 5.7% (b) 48.3% and (c) 19.6% fit to the anatase phase in P90. The curves are overlaid with the mixed phase P90 residual in light purple. Right column: the particle morphologies used in the fits. From top to bottom, a spherical approximation used for the AC model followed by the three discrete anatase structure models corresponding to residuals (b-d) in the middle panel. {001} surfaces are shown in red and {101} surfaces in blue. Bottom panel (e): Measured (open circles) and calculated (solid lines) PDFs for P90 refined over the full-r range using the best candidate discrete structure (19.6% {001} faceting). Annotated R_w values are calculated for the range plotted in each panel.

We therefore built discrete crystallites with different ratios of surface facet areas to determine if the structural misfit for the mixed TiO_2 samples studied here by PDF could be related to the morphology of the majority anatase phase. Three representative shapes were tested (see Fig. 5.6). 1) The Wulff model with 5.7% of the anatase surface exposed with {001} facets, 2) a nanoplatelet with 48.3% {001} facets, and 3) an intermediate morphology with 19.6% {001} facets. These were fit to the measured P90 dataset. The PDF from the model accounting for the minority rutile component was also added to the computed anatase model before assessing the agreement, though the parameters of the rutile model were not refined. The resulting residual curves, plotted over a range $1.5 < r < 20$ Å, are shown in Fig. 5.6 (b), (c) and (d) and the agreement factors, computed over the same r-range, are labeled in the figure. The nanoplatelet shape performs comparably to but slightly worse than the attenuated crystal model. However, there are significant improvements in the agreement for clusters with surfaces containing a much higher percentage of {101} facets, which are the Wulff and intermediate morphologies. The best agreement we obtained was for a particle with ∼20% {001} faceting and 80% {101} facets yielding an $R_w = 0.089$ computed over this low-r range, down from $R_w = 0.124$ for the AC model. This is a significant improvement for the addition of zero refinable variables, which is also evident as qualitatively smaller amplitude oscillations in the residual curve (Fig. 5.6(d)).

Finally, we selected the best candidate anatase shape with ∼20% {001} faceting and refined this to the raw P90 PDF over the full r-range to $R_{max} = 60$ Å. This refinement resulted in a significant improvement over the AC model over the entire range, with the R_w decreasing from 0.129 to 0.093 (ΔR_w = -32%). The fit also resulted in smaller refined ADPs, particularly for oxygen, with a decrease from 0.013 to 0.009, which alongside lower residuals is often an indication that a model is capturing the correct structure.

5.2 Discussion

The work was motivated by a desire to understand why many of the properties of pyrogenic titania are different from the properties of nanoparticulate anatase, despite being mostly anatase. Bickley *et al.* interpreted the presence of Moire fringes in HRTEM data as indicating a rutile core/anatase shell structure for P25. [19] Later work by Datye *et al.* and Ohno *et al.* refuted the core/shell model but both papers left open the possibility that a thin layer of rutile could have escaped detection. [30, 115] In this work, we provide evidence from TEM that P90 and P25 contain discrete intermingled particles of anatase and rutile titania. Careful PDF analysis of these materials finds no support for a core/shell structure. In a detailed DRIFTS study of surface hydroxyls coupled to DFT calculations that permitted assignment of bands to specific facets of particular crystal structures, we recently found compelling evidence that P90 and P25 contain surface hydroxyls from both anatase and rutile, again evidence that is inconsistent with a core/shell model.[93]

Shape controlled synthesis of pure anatase nanoparticles with specific ratios of surface facets is a common route towards tailoring their catalytic properties. [45, 32] Although this methodology is well-established and previous studies have demonstrated that powder diffraction can be sensitive to changes in anatase morphologies [86], the connections between surface faceting and catalytic activity in surfactant-free mixed TiO_2 materials, particularly pyrogenic P90/P25, remain unclear. In terms of differentiating pure TiO_2 mixtures from the pyrogenic, commercial samples, the main observation from the PDF analysis is that structurally and morphologically, these samples are rather similar. The primary difference lies in the relative particle sizes between minority and majority TiO_2 phases. In the physical mixture prepared from commercial anatase and commercial rutile, the minority rutile particles are much larger than the anatase particles, wherease in the pyrogenic P90 and P25

samples the anatase and minority rutile particles are comparably sized. These variations in the relative sizes of the anatase and rutile particle components in a sample may influence the differences in activity between the physical mixture and pyrogenic TiO_2 samples. Superior photocatalytic properites due to slower electron-hole pair recombination rates have been attributed to the particle sizes of pyrogenic titania [55]. Our characterization also confirms the close proximity of the rutile and anatase particles in pyrogenic titania. This close proximity, what Hurum described as "interwoven", may facilitate rapid electron transfer from rutile particles to anatase particles and enhance photocatalysis. [55] Recently published DRIFTS data from our lab points to the importance of surface interactions with water in controlling some catalytic features. Pyrogenic titania is not heavily hydroxylated, in contrast to low temperature synthesized anatase, and we think this difference is important for at least some catalytic applications. [94]

This work also highlights the sensitivity of PDF to nanoparticle morphologies, which has been demonstrated in metallic nanoparticles [15] and in pure nanocrystalline anatase TiO_2 [86]. Here we calculated PDFs directly using the Debye scattering equation (DSE) for the representative anatase morphologies. This work lays an alternative roadmap for future PDF studies of nanoparticulate TiO_2 from a broad range of applications and synthesis methods [110] that go well beyond typical PDF modeling routines. The discrete anatase cutouts that were tested to investigate particle morphology do not introduce new interatomic distances than those already present in the AC models, so it was somewhat surprising to us that these differences in shape can influence highly constrained PDF refinements so noticeably. The improvements must originate from changes in site multiplicities which differ based on the different coordination environments of surface terminated lattice planes. In the core of the anatase crystallites each Ti atom is sixfold coordinated to O, while {101} facets have both six and fivefold coordinated Ti, and {001} surfaces contain only undercoordinated

Ti atoms with five nearest neighbor oxygen atoms. When these undercoordinated surface atoms contribute significantly relative to the core, as is the case in nanoparticles, they affect the PDF not only at high-r, but locally as well, as we showed here. Such differences would not be captured by the mixed phase AC models, nor any numerical shape approximations [159, 117, 86]. However, we are confident from this work that the signals in the PDF are robust for determining the particle morphologies in anatase and the modeling approach we lay out here is straightforward.

5.3 Conclusion

This work provides a detailed quantitative characterization of the phase composition in commercially important TiO_2 materials, P90 and P25. XRD and PDF data presented here, along with insights from DRIFTS studies [94], are all consistent with the presence of a small fraction of discrete rutile crystallites and a majority of discrete anatase crystallites. There is no evidence for core/shell particles. The anatase and rutile crystallites are comparable in size in pyrogenic titania. We demonstrate that PDF is sensitive to TiO_2 particle morphology, which has important implications for efforts to understand how electronic and three-dimensional atomic structure determine the chemical and photochemical reactivity of catalysts, and how those properties change during use. [131]

5.4 Single phase refinements of TiO_2 supports

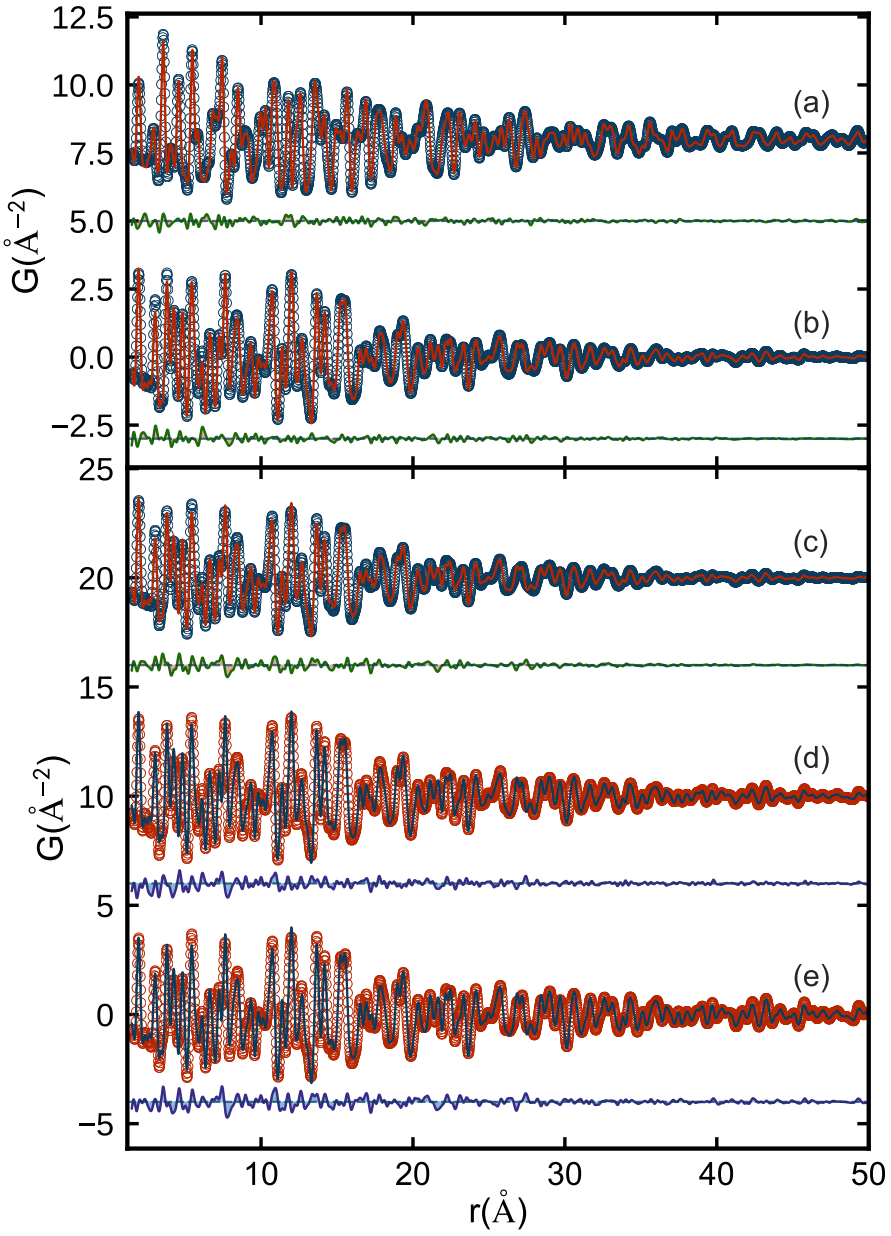

Figure 5.7: Measured (open symbols) and calculated (solid lines) PDFs of pure rutile (a) pure anatase (b) a physical mixture of 90% anatase and 10% rutile (c) P90 (d) and P25 (e). The experimental PDF for rutile (a) is fit with a single phase rutile model while the phase pure and majority anatase PDFs (b-e) are fit with a single phase anatase model. Difference curves are offset below.

Table 5.2: Refined parameters from single phase refinements of pure (columns 1-2) and mixed (columns 3-5) TiO_2 samples using a single phase anatase model for the mixed nanomaterials, which are expected to contain a majority Anatase phase. See the main text for descriptions of the abbreviations below. Structure models were obtained from published crystal structures of bulk anatase and rutile. [53, 16] For rutile (SG: $P4_2/mnm$), O is at the $2a$ $(0, 0, 0)$ site and Ti at $4f$ $(0.306, 0.306, 0)$. In anatase (SG: $I4_1/amd$), O is positioned at $4a$ $(0, 0, 0)$ and Ti at $8e$ $(0, 0, 0.208)$.

Sample	Anatase	Rutile	$Mix_{90:10}$	P90	P25
$a = b$ (Å)	3.785	4.592	3.783	3.785	3.785
c (Å)	9.504	2.958	9.498	9.487	9.492
Ti U_{iso} (Å^2)	0.006	0.006	0.007	0.005	0.005
O U_{iso} (Å^2)	0.016	0.016	0.017	0.015	0.014
SPD (Å)	69.78	152.4	68.66	93.27	161.06
R_w	0.104	0.109	0.155	0.163	0.181

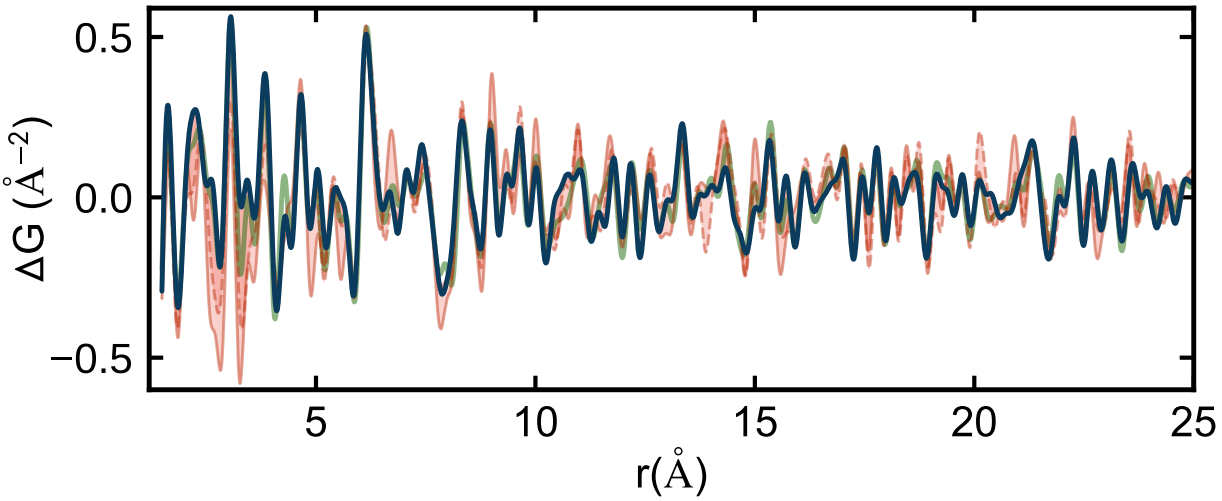

Figure 5.8: Dark blue: unfit signal from a single phase refinement of pure anatase. Green: unfit signal from mixed phase refinement of the physical mixture. Red and dashed red: unfit signal from mixed phase refinement of P90 and P25, respectively. The pearson correlation coefficients between all mixed phase TiO_2 residuals and the pure anatase residual are > 0.75 for an r-range between $1.2 < r < 30$ Å.

5.5 Morphological tests with pure anatase nanoparticles

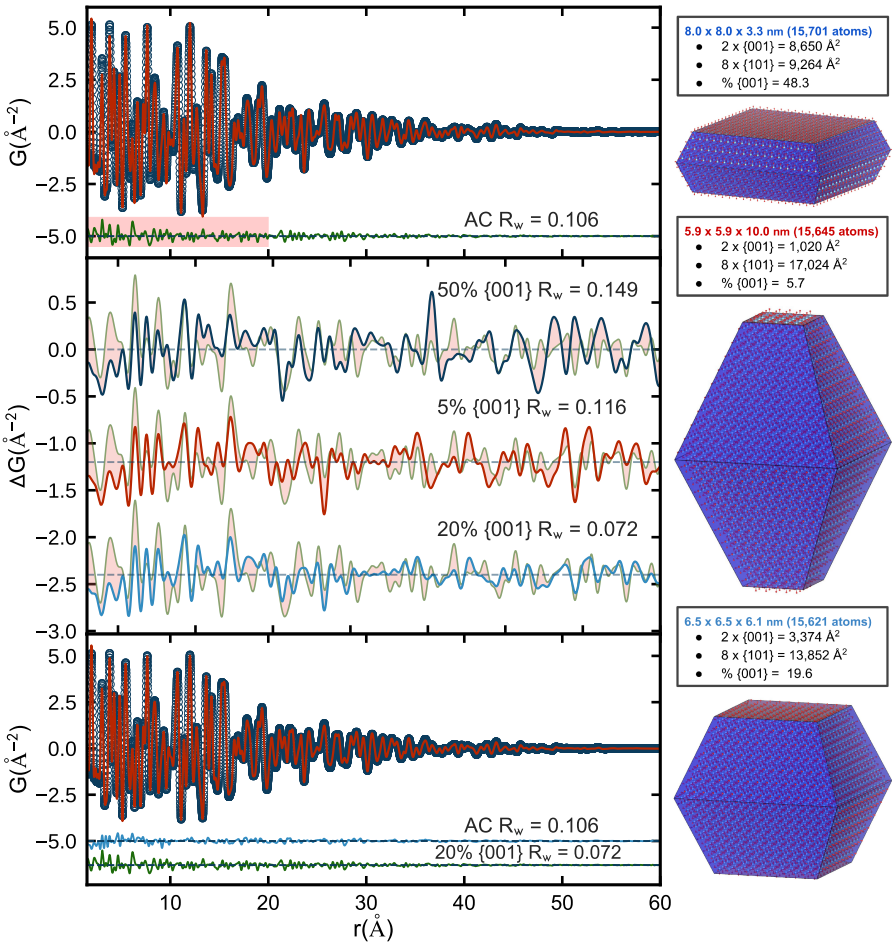

Figure 5.9: Top panel: Measured (open circles) and calculated (solid lines) PDFs for pure anatase refined over the full-r range to the mixed phase AC model. Middle panel: difference curves, plotted over a truncated r-range (highlighted in the top panel) from discrete anatase models with different percentages of {001} surface facets (as labeled) fit to the pure anatase sample. The curves are overlaid with the mixed phase anatase residual in light green. R_w values are calculated over full-r. Right column: the particle morphologies used in the fits, with descriptions of the facet specific surface areas. {001} surfaces are shown in red and {101} surfaces in blue. Bottom panel: Measured (open circles) and calculated (solid lines) PDFs for pure anatase refined over the full-r range using the best candidate discrete structure (19.6% {001} faceting).

5.6 Additional TEM images

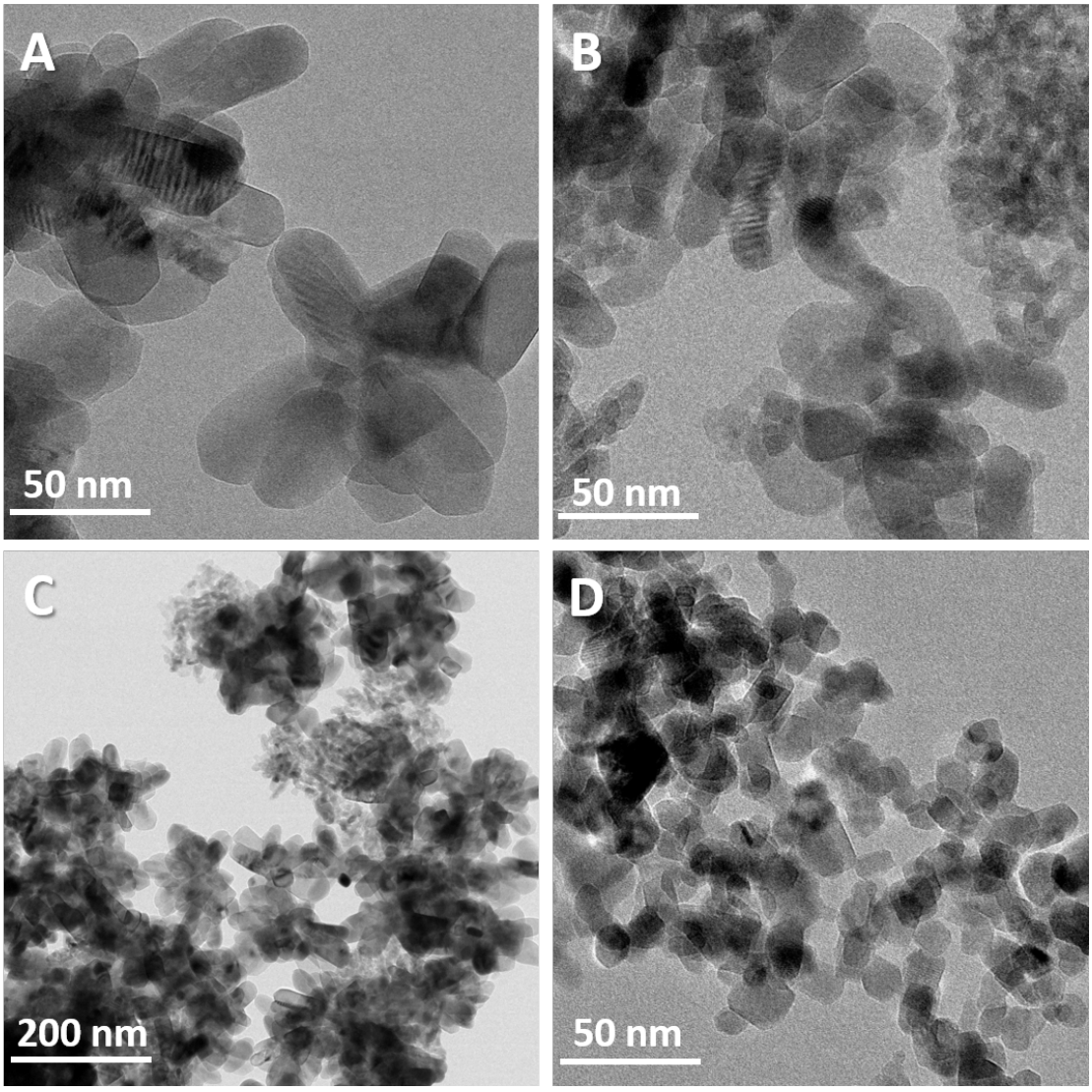

Figure 5.10: TEM micrographs of TiO_2 nanoparticles (a) pure rutile (b) pure anatase (c) a physical mixture with 90% anatase and 10% rutile and (d) P90

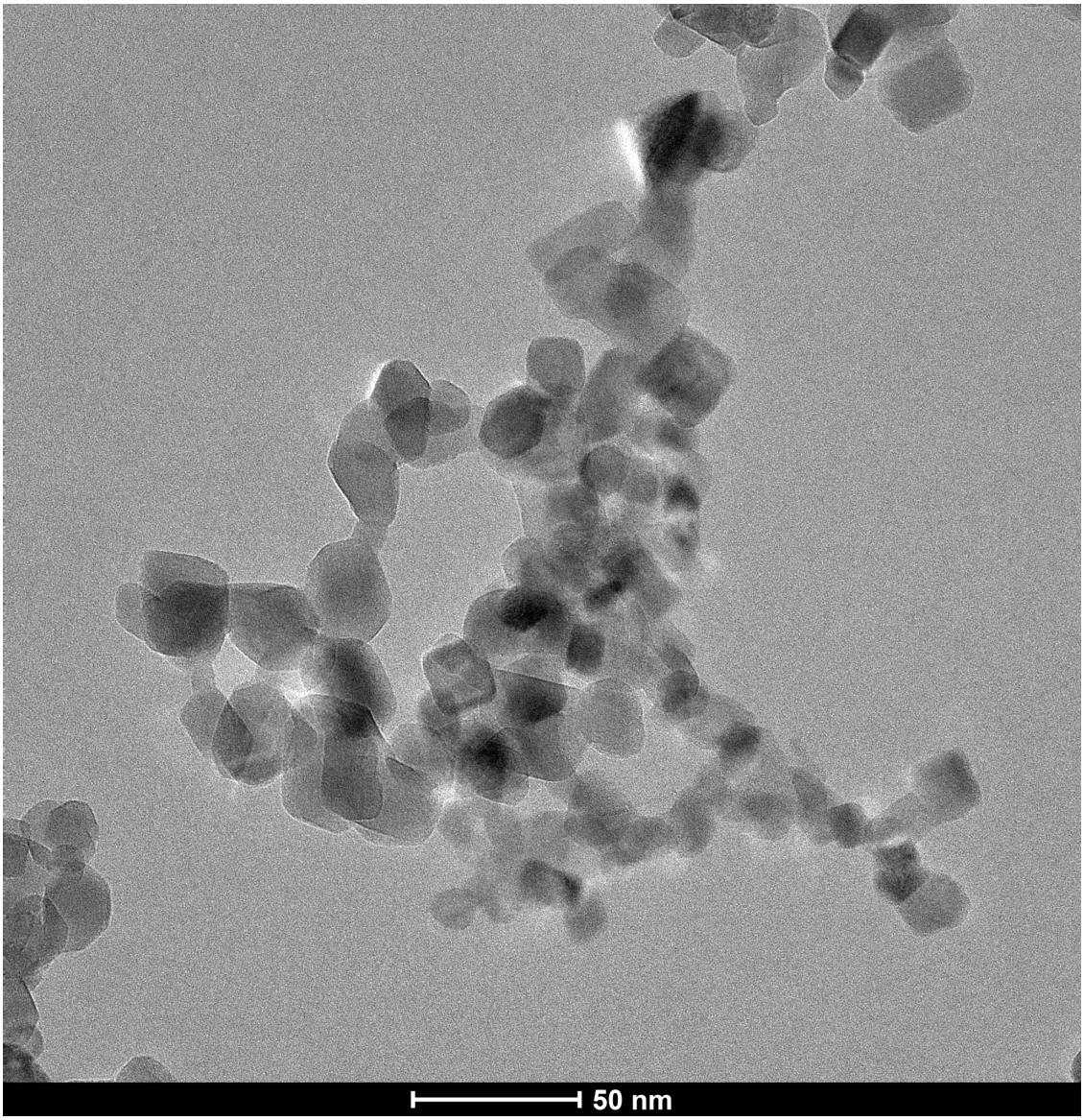

Figure 5.11: TEM micrograph of P25

5.7 Reciprocal space data prior to PDF transformation

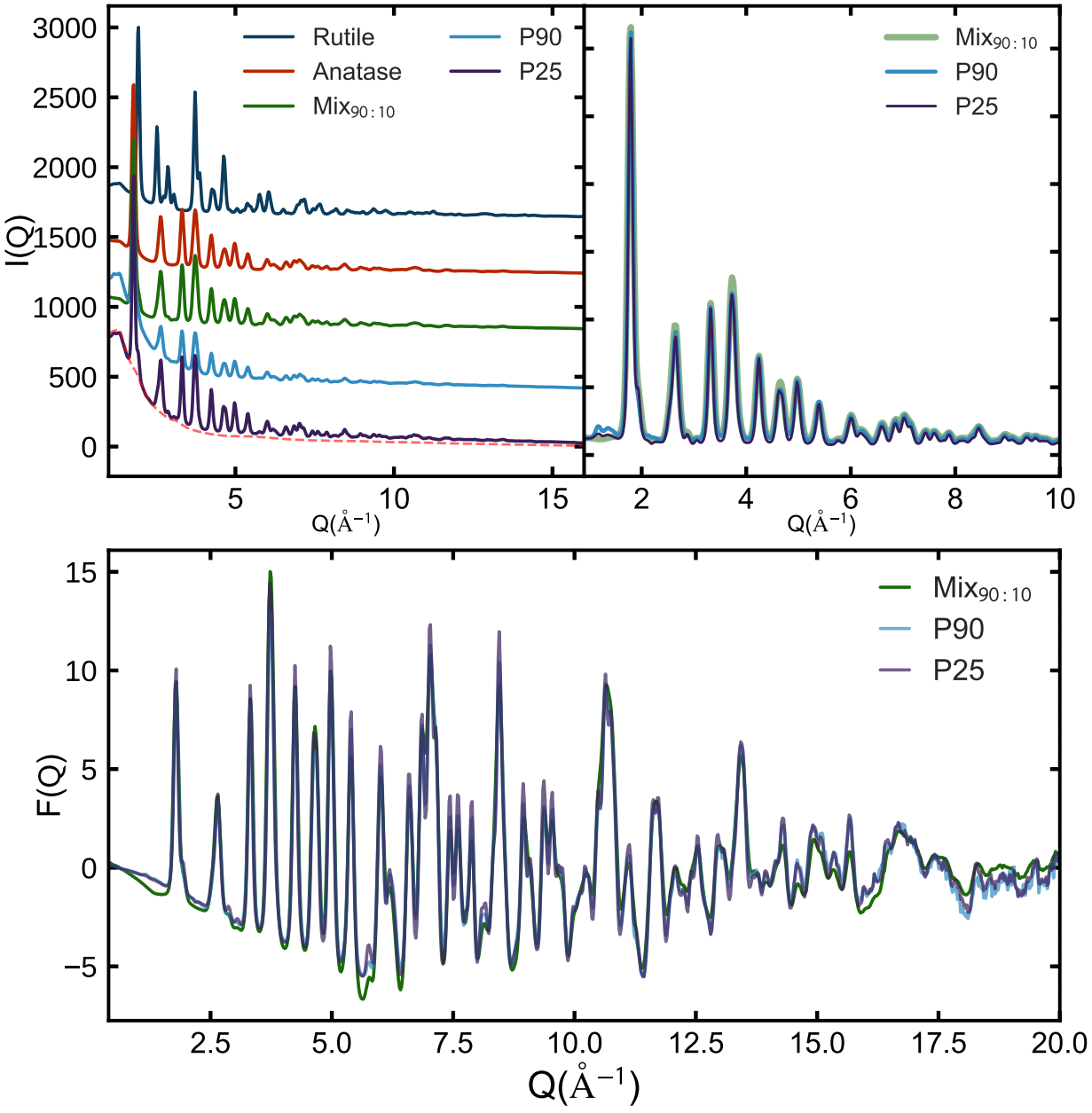

Figure 5.12: Top left: Raw integrated diffraction patterns of samples used for PDF analysis, as labeled. Top right: a comparison of background subtracted and scale normalized $I(Q)$ for mixed TiO_2 samples. Bottom: an analogous comparison of the phase mixtures after transformation to $F(Q)$. See the PDF methods section for details.

Bibliography

[1] Metal Nanoparticles of Complex Morphologies: A General Introduction. In *Complex-Shaped Metal Nanoparticles*, pages 1–5. John Wiley & Sons, Ltd, 2012.

[2] Christopher J. Ackerson, Pablo D. Jadzinsky, Grant J. Jensen, and Roger D. Kornberg. Rigid, Specific, and Discrete Gold Nanoparticle/Antibody Conjugates. *J. Am. Chem. Soc.*, 128(8):2635–2640, March 2006.

[3] Christopher J. Ackerson, Pablo D. Jadzinsky, Jonathan Z. Sexton, David A. Bushnell, and Roger D. Kornberg. Synthesis and Bioconjugation of 2 and 3 nm-diameter Gold Nanoparticles. *Bioconjug Chem*, 21(2):214–218, February 2010.

[4] Selim Alayoglu, Peter Zavalij, Bryan Eichhorn, Qi Wang, Anatoly I. Frenkel, and Peter Chupas. Structural and Architectural Evaluation of Bimetallic Nanoparticles: A Case Study of Pt-Ru Core-Shell and Alloy Nanoparticles. *ACS Nano*, 3(10):3127–3137, October 2009.

[5] A. P. Alivisatos. Semiconductor Clusters, Nanocrystals, and Quantum Dots. *Science*, 271(5251):933–937, February 1996.

[6] Jens Als-Nielsen and Des McMorrow. *Elements of Modern X-Ray Physics*. John Wiley & Sons, Am. Pharm. Rev. 2011.

[7] Antonino Salvatore Aricò, Peter Bruce, Bruno Scrosati, Jean-Marie Tarascon, and Walter van Schalkwijk. Nanostructured materials for advanced energy conversion and storage devices. *Nat. Mater.*, 4(5):366–377, May 2005.

[8] C. Arrouvel, M. Digne, M. Breysse, H. Toulhoat, and P Raybaud. Effects of morphology on surface hydroxyl concentration: a dft comparison of anatase-tio$_2$ and γ-alumina catalytic supports. *Journal of Catalysis*, 222:152–166, 2004.

[9] Harry A. Atwater and Albert Polman. Plasmonics for improved photovoltaic devices. *Nat. Mater.*, 9(3):205–213, March 2010.

[10] B. G. Bagley. A Dense Packing of Hard Spheres with Five-fold Symmetry. *Nature*, 208(5011):674–675, November 1965.

[11] Daniel Bahena, Nabraj Bhattarai, Ulises Santiago, Alfredo Tlahuice, Arturo Ponce, Stephan B. H. Bach, Bokwon Yoon, Robert L. Whetten, Uzi Landman, and Miguel Jose-Yacaman. Stem electron diffraction and high-resolution images used in the determination of the crystal structure of the $Au_{144}(SR)_{60}$ cluster. *J. Phys. Chem. Lett.*, 4(6):975–981, 2013.

[12] Daniel Bahena, Nabraj Bhattarai, Ulises Santiago, Alfredo Tlahuice, Arturo Ponce, Stephan B. H. Bach, Bokwon Yoon, Robert L. Whetten, Uzi Landman, and Miguel Jose-Yacaman. STEM Electron Diffraction and High-Resolution Images Used in the Determination of the Crystal Structure of the Au144(SR)60 Cluster. *J. Phys. Chem. Lett.*, 4(6):975–981, March 2013.

[13] S. Banerjee, K. Loza, W. Meyer-Zaika, O. Prymak, and M. Epple. Structural Evolution of Silver Nanoparticles during Wet-Chemical Synthesis. *Chem. Mater.*, 26(2):951–957, January 2014.

[14] S. Banerjee, K. Loza, W. Meyer-Zaika, O. Prymak, and M. Epple. Structural Evolution of Silver Nanoparticles during Wet-Chemical Synthesis. *Chem. Mater.*, 26(2):951–957, January 2014.

[15] Soham Banerjee, Chia-Hao Liu, Jennifer D. Lee, Anton Kovyakh, Viktoria Grasmik, Oleg Prymak, Christopher Koenigsmann, Haiqing Liu, Lei Wang, A. M. Milinda Abeykoon, Stanislaus S. Wong, Matthias Epple, Christopher B. Murray, and Simon J. L. Billinge. Improved Models for Metallic Nanoparticle Cores from Atomic Pair Distribution Function (PDF) Analysis. *J. Phys. Chem. C*, 122(51):29498–29506, December 2018.

[16] W. H. Baur and A. A. Khan. Rutile-type compounds. IV. SiO_2, GeO_2 and a comparison with other rutile-type structures. *Acta Crystallogr. B*, 27(11):2133–2139, November 1971.

[17] Alexander N. Beecher, Xiaohao Yang, Joshua H. Palmer, Alexandra L. LaGrassa, Pavol Juhás, Simon J. L. Billinge, and Jonathan S. Owen. Atomic structures and gram scale synthesis of three tetrahedral quantum dots. *J. Am. Chem. Soc.*, 136(30):10645–10653, 2014.

[18] K. R. Beyerlein, R. L. Snyder, and P. Scardi. Faulting in finite face-centered-cubic crystallites. *Acta Crystallogr. A*, 67(3):252–263, May 2011.

[19] R. Bickley, T. Gonzalez-Carrenoa, J. S. Lees, L. Palmisano, and R. D. Tilley. A structural investigation of titanium dioxide photocatalyst. *Journal of Solid State Chemistry*, 92:178–190, May 1991.

[20] Roger I. Bickley, Teresita Gonzalez-Carreno, John S. Lees, Leonardo Palmisano, and Richard J. D. Tilley. A structural investigation of titanium dioxide photocatalysts. *Journal of Solid State Chemistry*, 92(1):178–190, May 1991.

[21] S. J. L. Billinge and I. Levin. The problem with determining atomic structure at the nanoscale. *Science*, 316:561–565, 2007.

[22] E. D. Bøjesen and B. B. Iversen. The chemistry of nucleation. *CrystEngComm*, 18(43):8332–8353, October 2016.

[23] A. Cervellino, C. Giannini, and A. Guagliardi. Determination of nanoparticle structure type, size and strain distribution from X-ray data for monatomic f.c.c.-derived non-crystallographic nanoclusters. *J. Appl. Crystallogr.*, 36(5):1148–1158, October 2003.

[24] A. Cervellino, C. Giannini, A. Guagliardi, and D. Zanchet. Quantitative analysis of gold nanoparticles from synchrotron data by means of least-squares techniques. *Eur. Phys. J. B*, 41(4):485–493, October 2004.

[25] Chien-Chun Chen, Chun Zhu, Edward R. White, Chin-Yi Chiu, M. C. Scott, B. C. Regan, Laurence D. Marks, Yu Huang, and Jianwei Miao. Three-dimensional imaging of dislocations in a nanoparticle at atomic resolution. *Nature*, 496(7443):74–77, Am. Pharm. Rev. 2013.

[26] Hao Cheng, Yong Li, Kaifu Huo, Biao Gao, and Wei Xiong. Long-lasting in vivo and in vitro antibacterial ability of nanostructured titania coating incorporated with silver nanoparticles. *J. Biomed. Mater. Res. A*, 102(10):3488–3499, 2014.

[27] Joshua J. Choi, Xiaohao Yang, Zachariah M. Norman, Simon J. L. Billinge, and Jonathan S. Owen. Structure of methylammonium lead iodide on mesoporous titanium dioxide: active material in high performance metal-organic solar cells. *Nano Lett.*, 14(1):127133, 2014.

[28] Peter J. Chupas, Xiangyun Qiu, J. C. Hanson, P. L. Lee, Clare P. Grey, and Simon J. L. Billinge. Rapid acquisition pair distribution function analysis (RA-PDF). *J. Appl. Crystallogr.*, 36:1342–1347, 2003.

[29] A. A. Coelho. TOPAS and TOPAS-Academic: an optimization program integrating computer algebra and crystallographic objects written in C++. *J. Appl. Crystallogr.*, 51:210–218, 2018.

[30] Abhaya K. Datye, Georg Riegel, James R. Bolton, Min Huang, and Michael R. Prairie. Microstructural Characterization of a Fumed Titanium Dioxide Photocatalyst. *Journal of Solid State Chemistry*, 115(1):236–239, February 1995.

[31] A. K. Dayte, G. Riegel, J. R. Bolton, M. Huang, and M. R. Prairie. Microstructural characterization of a fumed titanium dioxide photocatalyst. *Journal of Solid State Chemistry*, 115(1):236–239, 1995.

[32] Filippo De Angelis, Cristiana Di Valentin, Simona Fantacci, Andrea Vittadini, and Annabella Selloni. Theoretical Studies on Anatase and Less Common TiO_2 Phases: Bulk, Surfaces, and Nanomaterials. *Chem. Rev.*, 114(19):9708–9753, October 2014.

[33] P. Debye. Dispersion of Röntgen rays. *Annalen der Physik (Berlin, Germany)*, 351:809–823, 1915.

[34] Robert E. Dinnebier and Simon J. L. Billinge, editors. *Powder diffraction: theory and practice*. Royal Society of Chemistry, London, England, 2008.

[35] Vicky V. T. Doan-Nguyen, Simon A. J. Kimber, Diego Pontoni, Danielle Reifsnyder Hickey, Benjamin T. Diroll, Xiaohao Yang, Marcel Miglierini, Christopher B. Murray, and Simon J. L. Billinge. Bulk metallic glass-like scattering signal in small metallic nanoparticles. *ACS Nano.*, 8(6):6163–6170, 2014.

[36] Timur Dykhne, Ryan Taylor, Alastair Florence, and Simon J. L. Billinge. Data requirements for the reliable use of atomic pair distribution functions in amorphous pharmaceutical fingerprinting. *Pharm. Res.*, 28(5):1041–1048, May 2011.

[37] T. Egami and S. J. L. Billinge. *Underneath the Bragg peaks: structural analysis of complex materials*. Elsevier, Amsterdam, 2nd edition, 2012.

[38] C. L. Farrow and S. J. L. Billinge. Relationship between the atomic pair distribution function and small angle scattering: implications for modeling of nanoparticles. *Acta Crystallogr. A*, 65(3):232–239, 2009.

[39] C. L. Farrow, P. Juhás, Jiwu Liu, D. Bryndin, E. S. Božin, J. Bloch, Th. Proffen, and S. J. L. Billinge. PDFfit2 and PDFgui: Computer programs for studying nanostructure in crystals. *J. Phys: Condens. Mat.*, 19:335219, 2007.

[40] Christoper L. Farrow, Chenyang Shi, Pavol Juhás, Xiaogang Peng, and Simon J. L. Billinge. Robust structure and morphology parameters for CdS nanoparticles by combining small angle X-ray scattering and atomic pair distribution function data in a complex modeling framework. *J. Appl. Crystallogr.*, 47:561–565, 2014.

[41] Blaise Fleury, Robinson Cortes-Huerto, Olivier Taché, Fabienne Testard, Nicolas Menguy, and Olivier Spalla. Gold Nanoparticle Internal Structure and Symmetry Probed by Unified Small-Angle X-ray Scattering and X-ray Diffraction Coupled with Molecular Dynamics Analysis. *Nano Lett.*, 15(9):6088–6094, Sep. Purif. Technol. 2015.

[42] L. Gamez-Mendoza, M. W. Terban, S. J. L. Billinge, and M. Martinez-Inesta. Modelling and validation of particle size distributions of supported nanoparticles using the pair distribution function technique. *J. Appl. Crystallogr.*, 50(3):741–748, June 2017.

[43] B. Gilbert, F. Huang, H. Zhang, G. A. Waychunas, and J. F. Banfield. Nanoparticles: Strained and stiff. *Science*, 305:651–654, 2004.

[44] Christopher Gilmore, James A. Kaduk, and Henk Schenk. *International Tables for Crystallography: Volume H: Powder Diffraction (2019)*. John Wiley & Sons, 1st online edition edition, 2019.

[45] Xue-Qing Gong and Annabella Selloni. Reactivity of Anatase TiO_2 Nanoparticles: The Role of the Minority (001) Surface. *J. Phys. Chem. B*, 109(42):19560–19562, October 2005.

[46] Thomas R. Gordon, Matteo Cargnello, Taejong Paik, Filippo Mangolini, Ralph T. Weber, Paolo Fornasiero, and Christopher B. Murray. Nonaqueous Synthesis of TiO_2 Nanocrystals Using TiF_4 to Engineer Morphology, Oxygen Vacancy Concentration, and Photocatalytic Activity. *J. Am. Chem. Soc.*, 134(15):6751–6761, Am. Pharm. Rev. 2012.

[47] Viktoria Grasmik, Christian Rurainsky, Kateryna Loza, Mathies V. Evers, Oleg Prymak, Marc Heggen, Kristina Tschulik, and Matthias Epple. Deciphering the Surface Composition and the Internal Structure of Alloyed Silver-Gold Nanoparticles. *Chem. Eur. J.*, Just Accepted, March 2018.

[48] A. Guinier. *X-ray Diffraction in Crystals, Imperfect Crystals, and Amorphous Bodies.* W.H. Freeman, San Francisco, 1963.

[49] Luke G. Gutwein and Thomas J. Webster. Osteoblast and Chrondrocyte Proliferation in the Presence of Alumina And Titania Nanoparticles. *Journal of Nanoparticle Research*, 4(3):231–238, June 2002.

[50] Thomas C. Hales. A Proof of the Kepler Conjecture. *Ann. Math.*, 162(3):1065–1185, 2005.

[51] A. P. Hammersley, S. O. Svenson, M. Hanfland, and D. Hauserman. Two-dimensional detector software: from real detector to idealised image or two-theta scan. *High Pressure Res.*, 14:235–248, 1996.

[52] Brian E. Hardin, Henry J. Snaith, and Michael D. McGehee. The renaissance of dye-sensitized solar cells. *Nat. Photonics*, 6(3):162–169, March 2012.

[53] M Horn and C F Schwerdtfeger. Refinement of the structure of anatase at several temperatures. *Z. Für Krist.*, (136):273–281, May 1972.

[54] Xiaoqing Huang and Nanfeng Zheng. One-Pot, High-Yield Synthesis of 5-Fold Twinned Pd Nanowires and Nanorods. *J. Am. Chem. Soc.*, 131(13):4602–4603, Am. Pharm. Rev. 2009.

[55] Deanna C. Hurum, Alexander G. Agrios, Kimberly A. Gray, Tijana Rajh, and Marion C. Thurnauer. Explaining the Enhanced Photocatalytic Activity of Degussa P25 Mixed-Phase TiO_2 Using EPR. *J. Phys. Chem. B*, 107(19):4545–4549, May 2003.

[56] Shozo Ino. Epitaxial Growth of Metals on Rocksalt Faces Cleaved in Vacuum. II. Orientation and Structure of Gold Particles Formed in Ultrahigh Vacuum. *J. Phys. Soc. Jpn.*, 21(2):346–362, February 1966.

[57] Shozo Ino. Stability of Multiply-Twinned Particles. *J. Phys. Soc. Jpn.*, 27(4):941–953, October 1969.

[58] Pablo D. Jadzinsky, Guillermo Calero, Christopher J. Ackerson, David A. Bushnell, and Roger D. Kornberg. Structure of a Thiol Monolayer-Protected Gold Nanoparticle at 1.1 Å Resolution. *Science*, 318(5849):430–433, October 2007.

[59] Kirsten M. Ø. Jensen, Pavol Juhás, Marcus A. Tofanelli, Christine L. Heinecke, Gavin Vaughan, Christopher J. Ackerson, and Simon J. L. Billinge. Polymorphism in magic sized $Au_{144}(SR)_{60}$ clusters. *Nat. Commun.*, 7:11859, 2016.

[60] Kirsten M. Ø Jensen, Pavol Juhas, Marcus A. Tofanelli, Christine L. Heinecke, Gavin Vaughan, Christopher J. Ackerson, and Simon J. L. Billinge. Polymorphism in magic-sized $Au_{144}(SR)_{60}$ clusters. *Nat. Commun.*, 7:11859, June 2016.

[61] I.-K. Jeong, Th. Proffen, F. Mohiuddin-Jacobs, and S. J. L. Billinge. Measuring correlated atomic motion using x-ray diffraction. *J. Phys. Chem. A*, 103:921–924, 1999.

[62] Nicola Jones. Crystallography: Atomic secrets. *Nat. News*, 505(7485):602, January 2014.

[63] P. Juhás, D. M. Cherba, P. M. Duxbury, W. F. Punch, and S. J. L. Billinge. Ab initio determination of solid-state nanostructure. *Nature*, 440(7084):655–658, 2006.

[64] P. Juhás, T. Davis, C. L. Farrow, and S. J. L. Billinge. PDFgetX3: A rapid and highly automatable program for processing powder diffraction data into total scattering pair distribution functions. *J. Appl. Crystallogr.*, 46:560–566, 2013.

[65] Pavol Juhás, Christopher L. Farrow, Xiaohao Yang, Kevin R. Knox, and Simon J. L. Billinge. Complex modeling: a strategy and software program for combining multiple information sources to solve ill-posed structure and nanostructure inverse problems. *Acta Crystallogr. A*, 71(6):562–568, Nov 2015.

[66] J Kepler. Strena Seu de Niue Sexangula, Godrey Tampach: Frankfort on Main.(1611); English Translation: J. Kepler, The Six-Cornered Snowflake. *Godrey Tampach Frankf. Main*, 1611.

[67] J. Kieffer, G. Ashiotis, A. Deschildre, Z. Nawaz, J. P. Wright, D. Karkoulis, and F. E. Picca. The fast azimuthal integration python library: pyFAI. *J. Appl. Crystallogr.*, 48:510–519, 2015.

[68] J. Kieffer and D. Karkoulis. Pyfai, a versatile library for azimuthal regrouping. *J. Phys.: Conf. Ser.*, SRI2012, 2013.

[69] K. Kodama, S. Iikubo, T. Taguchi, and S. Shamoto. Finite size effects of nanoparticles on the atomic pair distribution functions. *Acta Crystallogr. A*, 62:444–453, 2006.

[70] Christopher Koenigsmann, Alexander C. Santulli, Kuanping Gong, Miomir B. Vukmirovic, Wei-ping Zhou, Eli Sutter, Stanislaus S. Wong, and Radoslav R. Adzic. Enhanced Electrocatalytic Performance of Processed, Ultrathin, Supported Pd–Pt Core–Shell Nanowire Catalysts for the Oxygen Reduction Reaction. *J. Am. Chem. Soc.*, 133(25):9783–9795, June 2011.

[71] Christopher Koenigsmann, Eli Sutter, Radoslav R. Adzic, and Stanislaus S. Wong. Size- and composition-dependent enhancement of electrocatalytic oxygen reduction performance in ultrathin palladiumgold ($pd_{1-x}au_x$) nanowires. *J. Phys. Chem. C*, 116(29):15297–15306, July 2012.

[72] Ch. V Kopezky, V. Yu Novikov, L. K Fionova, and N. A Bolshakova. Investigation of annealing twins in F.C.C. metals. *Acta Metallurgica*, 33(5):873–879, May 1985.

[73] Challa S. S. R. Kumar. *Transmission Electron Microscopy Characterization of Nanomaterials*. Springer Science & Business Media, December 2013.

[74] Chanaka Kumara, Xiaobing Zuo, David A. Cullen, and Amala Dass. Faradaurate-940: Synthesis, mass spectrometry, electron microscopy, high-energy x-ray diffraction, and x-ray scattering study of $au_{\sim 940}(sr)_{\sim 160}$ nanocrystals. *ACS Nano*, 2014. doi: 10.1021/nn501970v.

[75] Chanaka Kumara, Xiaobing Zuo, Jan Ilavsky, Karena W. Chapman, David A. Cullen, and Amala Dass. Super-stable, highly monodisperse plasmonic faradaurate-500 nanocrystals with 500 gold atoms: $Au_{\sim 500}(sr)_{\sim 120}$. *J. Am. Chem. Soc.*, 136(20):7410–7417, 2014.

[76] Mark R. Langille, Jian Zhang, Michelle L. Personick, Shuyou Li, and Chad A. Mirkin. Stepwise Evolution of Spherical Seeds into 20-Fold Twinned Icosahedra. *Science*, 337(6097):954–957, August 2012.

[77] Ask Hjorth Larsen, Jens Jørgen Mortensen, Jakob Blomqvist, Ivano E. Castelli, Rune Christensen, Marcin Dułak, Jesper Friis, Michael N. Groves, Bjørk Hammer, Cory Hargus, Eric D. Hermes, Paul C. Jennings, Peter Bjerre Jensen, James Kermode, John R. Kitchin, Esben Leonhard Kolsbjerg, Joseph Kubal, Kristen Kaasbjerg, Steen Lysgaard, Jón Bergmann Maronsson, Tristan Maxson, Thomas Olsen, Lars Pastewka, Andrew Peterson, Carsten Rostgaard, Jakob Schiøtz, Ole Schütt, Mikkel Strange, Kristian S. Thygesen, Tejs Vegge, Lasse Vilhelmsen, Michael Walter, Zhenhua Zeng, and Karsten W. Jacobsen. The atomic simulation environment—a Python library for working with atoms. *J. Phys.: Condens. Matter*, 29(27):273002, 2017.

[78] Michele Lazzeri, Andrea Vittadini, and Annabella Selloni. Structure and energetics of stoichiometric tio_2 anatase surfaces. *Phys. Rev. B*, 63(15):155409, March 2001.

[79] V. A. Lebedev, D. A. Kozlov, I. V. Kolesnik, A. S. Poluboyarinov, A. E. Becerikli, W. Grünert, and A. V. Garshev. The amorphous phase in titania and its influence

on photocatalytic properties. *Applied Catalysis B: Environmental*, 195:39–47, October 2016.

[80] Jisoo Lee, Jiwoong Yang, Soon Gu Kwon, and Taeghwan Hyeon. Nonclassical nucleation and growth of inorganic nanoparticles. *Nat. Rev. Mater.*, 1(8):16034, August 2016.

[81] L. N. Lewis. Chemical catalysis by colloids and clusters. *Chem. Rev.*, 93(8):2693–2730, 1993.

[82] Jian Li and Junliang Sun. Application of X-ray Diffraction and Electron Crystallography for Solving Complex Structure Problems. *Acc. Chem. Res.*, 50(11):2737–2745, November 2017.

[83] Suljo Linic, Phillip Christopher, and David B. Ingram. Plasmonic-metal nanostructures for efficient conversion of solar to chemical energy. *Nat. Mater.*, 10(12):911–921, December 2011.

[84] Haiqing Liu, Christopher Koenigsmann, Radoslav R. Adzic, and Stanislaus S. Wong. Probing Ultrathin One-Dimensional Pd–Ni Nanostructures As Oxygen Reduction Reaction Catalysts. *ACS Catal.*, 4(8):2544–2555, August 2014.

[85] Haiqing Liu, Christopher Koenigsmann, Radoslav R. Adzic, and Stanislaus S. Wong. Probing Ultrathin One-Dimensional Pd–Ni Nanostructures As Oxygen Reduction Reaction Catalysts. *ACS Catal.*, 4(8):2544–2555, August 2014.

[86] Jue Liu, Daniel Olds, Rui Peng, Lei Yu, Guo Shiou Foo, Shuo Qian, Jong Keum, Beth S. Guiton, Zili Wu, and Katharine Page. Quantitative Analysis of the Morphology of {101} and {001} Faceted Anatase TiO_2 Nanocrystals and Its Implication on Photocatalytic Activity. *Chem. Mater.*, 29(13):5591–5604, July 2017.

[87] C. Lofton and W. Sigmund. Mechanisms Controlling Crystal Habits of Gold and Silver Colloids. *Adv. Funct. Mater.*, 15(7):1197–1208, July 2005.

[88] A. Longo and A. Martorana. Distorted f.c.c. arrangement of gold nanoclusters: A model of spherical particles with microstrains and stacking faults. *J. Appl. Crystallogr.*, 41(2):446–455, Am. Pharm. Rev. 2008.

[89] Olga Lopez-Acevedo, Jaakko Akola, Robert L. Whetten, Henrik Gronbeck, and Hannu Hakkinen. Structure and Bonding in the Ubiquitous Icosahedral Metallic Gold Cluster Au144(SR)60. *J. Phys. Chem. C*, 113(13):5035–5038, Am. Pharm. Rev. 2009.

[90] Olga Lopez-Acevedo, Jaakko Akola, Robert L. Whetten, Henrik Grnbeck, and Hannu Hkkinen. Structure and bonding in the ubiquitous icosahedral metallic gold cluster $Au_{144}(SR)_{60}$. *J. Phys. Chem. C*, 113(13):5035–5038, 2009.

[91] Jose Luis Elechiguerra, Jose Reyes-Gasga, and Miguel Jose Yacaman. The role of twinning in shape evolution of anisotropic noble metal nanostructures. *J. Mater. Chem.*, 16(40):3906–3919, 2006.

[92] A. L. Mackay. A dense non-crystallographic packing of equal spheres. *Acta Crystallogr*, 15(9):916–918, Sep. Purif. Technol. 1962.

[93] Akbar Mahdavi-Shakib, Juan M. Arce-Ramos, Rachel N. Austin, Thomas J. Schwartz, Lars C. Grabow, and Brian G. Frederick. Frequencies and thermal stability of isolated surface hydroxyls on pyrogenic tio_2 nanoparticles. *J. Phys. Chem. C*, Submitted, 2019.

[94] Akbar Mahdavi-Shakib, Samra Husremovic, Sohee Ki, Jessica Glynn, Lauren Babb, Janine Sempel, Ioannis Stavrinoudis, Juan Manual Arce Ramos, Ryan Nelson, Lars C. Grabow, Thomas J. Schwartz, Brian G. Frederick, and Rachel Narehood Austin. Titania surface chemistry and its influence on supported metal catalysts. *Polyhedron.*, 170:41–50, May 2019.

[95] Dirk Mahl, Jörg Diendorf, Simon Ristig, Christina Greulich, Zi-An Li, Michael Farle, Manfred Köller, and Matthias Epple. Silver, gold, and alloyed silver–gold nanoparticles: Characterization and comparative cell-biologic action. *J. Nanopart. Res.*, 14(10):1153, Sep. Purif. Technol. 2012.

[96] L. D. Marks. Experimental studies of small particle structures. *Rep. Prog. Phys.*, 57(6):603, 1994.

[97] L. D. Marks and A. Howie. Multiply-twinned particles in silver catalysts. *Nature*, 282(5735):196–198, November 1979.

[98] L. D. Marks and L. Peng. Nanoparticle shape, thermodynamics and kinetics. *J. Phys.: Condens. Matter*, 28(5):053001, January 2016.

[99] T. P. Martin. Shells of atoms. *Physics Reports*, 273(4):199–241, August 1996.

[100] A. S. Masadeh, E. S. Božin, C. L. Farrow, G. Paglia, P. Juhás, A. Karkamkar, M. G. Kanatzidis, and S. J. L. Billinge. Quantitative size-dependent structure and strain determination of CdSe nanoparticles using atomic pair distribution function analysis. *Phys. Rev. B*, 76:115413, 2007.

[101] Vismadeb Mazumder, Miaofang Chi, Max N. Mankin, Yi Liu, Önder Metin, Daohua Sun, Karren L. More, and Shouheng Sun. A Facile Synthesis of MPd (M = Co, Cu) Nanoparticles and Their Catalysis for Formic Acid Oxidation. *Nano Lett.*, 12(2):1102–1106, February 2012.

[102] Nicholas A. Merrill, Erik M. McKee, Kyle C. Merino, Lawrence F. Drummy, Sungsik Lee, Benjamin Reinhart, Yang Ren, Anatoly I. Frenkel, Rajesh R. Naik, Nicholas M. Bedford, and Marc R. Knecht. Identifying the Atomic-Level Effects of Metal Composition on the Structure and Catalytic Activity of Peptide-Templated Materials. *ACS Nano*, 9(12):11968–11979, December 2015.

[103] Jian-Li Mi, Kirsten M. Ø. Jensen, Christoffer Tyrsted, Martin Bremholm, and Bo B. Iversen. In situ total X-ray scattering study of the formation mechanism and structural defects in anatase TiO_2 nanoparticles under hydrothermal conditions. *CrystEngComm*, 17(36):6868–6877, 2015.

[104] L. Mino, G. Spoto, S. Bordiga, and A.. Zecchina. Particles, morphology, and surface properties as investigated by hrtem, ftir, and periodic dft calculations: From pyrogenic tio_2 to nanoanatase. *J. Phys. Chem. C*, 116:17008–17018, 2012.

[105] Lorenzo Mino, Giuseppe Spoto, Silvia Bordiga, and Adriano Zecchina. Rutile Surface Properties Beyond the Single Crystal Approach: New Insights from the Experimental Investigation of Different Polycrystalline Samples and Periodic DFT Calculations. *J. Phys. Chem. C*, 117(21):11186–11196, May 2013.

[106] Anna Moiseev, Marina Krichevskaya, Fei Qi, Alfred P. Weber, and Joachim Deubener. Analysis of photocatalytic performance of nanostructured pyrogenic titanium dioxide powders in view of their polydispersity and phase transition: Critical anatase particle size as a factor for suppression of charge recombination. *Chem. Eng. J.*, 228:614–621, July 2013.

[107] Anna Moiseev, Fei Qi, Joachim Deubener, and Alfred Weber. Photocatalytic activity of nanostructured titanium dioxide from diffusion flame synthesis. *Chem. Eng. J.*, 170(1):308–315, May 2011.

[108] Koichi Momma and Fujio Izumi. VESTA: A three-dimensional visualization system for electronic and structural analysis. *J. Appl. Crystallogr.*, 41(3):653–658, June 2008.

[109] Rubul Mout, Daniel F. Moyano, Subinoy Rana, and Vincent M. Rotello. Surface functionalization of nanoparticles for nanomedicine. *Chem Soc Rev*, 41(7):2539–2544, Am. Pharm. Rev. 2012.

[110] Nathan Nakamura, Maxwell W. Terban, Simon J. L. Billinge, and B. Reeja Jayan. Unlocking the structure of mixed amorphous-crystalline ceramic oxide films synthesized under low temperature electromagnetic excitation. *J. Mater. Chem. A*, 5(35):18434–18441, 2017.

[111] H. Nakotte, C. Silkwood, K. Page, H.-W. Wang, D. Olds, B. Kiefer, S. Manna, D. Karpov, E. Fohtung, and E. E. Fullerton. Pair distribution function analysis applied to decahedral gold nanoparticles. *Phys. Scr.*, 92(11):114002, 2017.

[112] Yuichi Negishi, Tafu Nakazaki, Sami Malola, Shinjiro Takano, Yoshiki Niihori, Wataru Kurashige, Seiji Yamazoe, Tatsuya Tsukuda, and Hannu Häkkinen. A Critical Size for Emergence of Nonbulk Electronic and Geometric Structures in Dodecanethiolate-Protected Au Clusters. *J. Am. Chem. Soc.*, 137(3):1206–1212, January 2015.

[113] Mark A. Newton, Karena W. Chapman, David Thompsett, and Peter J. Chupas. Chasing changing nanoparticles with time-resolved pair distribution function methods. *J. Am. Chem. Soc.*, 134(11):5036–5039, 2012.

[114] Satish K Nune, Padmaja Gunda, Praveen K Thallapally, Ying-Ying Lin, M Laird Forrest, and Cory J Berkland. Nanoparticles for biomedical imaging. *Expert Opin Drug Deliv*, 6(11):1175–1194, November 2009.

[115] Teruhisa Ohno, Koji Sarukawa, Kojiro Tokieda, and Michio Matsumura. Morphology of a TiO_2 Photocatalyst (Degussa, P-25) Consisting of Anatase and Rutile Crystalline Phases. *Journal of Catalysis*, 203(1):82–86, October 2001.

[116] B. Ohtani, O. O. Prieto-Mahaney, D. Li, and R. Abe. What is Degussa (Evonik) P25? Crystalline composition analysis, reconstruction from isolated pure particles and photocatalytic activity test. *Journal of Photochemistry and Photobiology A: Chemistry*, 216(2):179–182, December 2010.

[117] Daniel Olds, Hsiu-Wen Wang, and Katharine Page. *DShaper*: An approach for handling missing low- Q data in pair distribution function analysis of nanostructured systems. *J. Appl. Crystallogr.*, 48(6):1651–1659, December 2015.

[118] K. Page, T. Proffen, H. Terrones, M. Terrones, L. Lee, Y. Yang, S. Stemmer, R. Seshadri, and A. K. Cheetham. Direct observation of the structure of gold nanoparticles by total scattering powder neutron diffraction. *Chem. Phys. Lett.*, 393:385–388, 2004.

[119] Katharine Page, Taylor C. Hood, Thomas Proffen, and Reinhard B. Neder. Building and refining complete nanoparticle structures with total scattering data. *J. Appl. Crystallogr.*, 44(2):327–336, 2011.

[120] Katharine Page, Thomas Proffen, Markus Niederberger, and Ram Seshadri. Probing local dipoles and ligand structure in batio$_3$ nanoparticles. *Chem. Mater.*, 22(15):4386–4391, 2010.

[121] L. Palatinus and G. Chapuis. SUPERFLIP – a computer program for the solution of crystal structures by charge flipping in arbitrary dimensions. *J Appl Cryst*, 40(4):786–790, August 2007.

[122] Ashley M. Pennington, Amanda I. Okonmah, Daryll T. Munoz, George Tsilomelekis, and Fuat E. Celik. Changes in Polymorph Composition in P25-TiO_2 during Pretreatment Analyzed by Differential Diffuse Reflectance Spectral Analysis. *J. Phys. Chem. C*, 122(9):5093–5104, March 2018.

[123] V. Petkov, Y. Peng, G. Williams, B. Huang, D. Tomalia, and Y. Ren. Structure of gold nanoparticles in water by x-ray diffraction and computer simulations. *Phys. Rev. B*, 72:195402, 2005.

[124] V. Petkov, S. Shastri, J.-W. Kim, S. Shan, J. Luo, J. Wu, and C.-J. Zhong. Application of differential resonant high-energy X-ray diffraction to three-dimensional structure studies of nanosized materials: A case study of Pt–Pd nanoalloy catalysts. *Acta Cryst A, Acta Cryst Sect A, Acta Crystallogr A, Acta Crystallogr Sect A, Acta Crystallogr A Cryst Phys Diffr Theor Gen Crystallogr, Acta Crystallogr Sect A Cryst Phys Diffr Theor Gen Crystallogr*, 74(5):553–566, Sep. Purif. Technol. 2018.

[125] V. Petkov and S. D. Shastri. Element-specific structure of materials with intrinsic disorder by high-energy resonant x-ray diffraction and differential atomic pair-distribution functions: A study of PtPd nanosized catalysts. *Phys. Rev. B*, 81(16):165428, Am. Pharm. Rev. 2010.

[126] V. Petkov and S. D. Shastri. Element-specific structure of materials with intrinsic disorder by high-energy resonant x-ray diffraction and differential atomic pair-distribution functions: A study of PtPd nanosized catalysts. *Phys. Rev. B*, 81(16):165428, 2010.

[127] Valeri Petkov, Nick Bedford, Marc R. Knecht, Michael G. Weir, Richard M. Crooks, Wenjie Tang, Graeme Henkelman, and Anatoly Frenkel. Periodicity and Atomic Ordering in Nanosized Particles of Crystals. *J. Phys. Chem. C*, 112(24):8907–8911, June 2008.

[128] Valeri Petkov, Binay Prasai, Sarvjit Shastri, Jong-Woo Kim, Shiyao Shan, Haval R. Kareem, Jin Luo, and Chuan-Jian Zhong. Surface Atomic Structure and Functionality of Metallic Nanoparticles: A Case Study of Au–Pd Nanoalloy Catalysts. *J. Phys. Chem. C*, 121(14):7854–7866, Am. Pharm. Rev. 2017.

[129] Valeri Petkov, Sarvjit Shastri, Shiyao Shan, Pharrah Joseph, Jin Luo, Chuan-Jian Zhong, Takahiro Nakamura, Yuliati Herbani, and Shunichi Sato. Resolving Atomic Ordering Differences in Group 11 Nanosized Metals and Binary Alloy Catalysts by Resonant High-Energy X-ray Diffraction and Computer Simulations. *J. Phys. Chem. C*, 117(42):22131–22141, October 2013.

[130] Valeri Petkov, Bridgid N. Wanjala, Rameshwori Loukrakpam, Jin Luo, Lefu Yang, Chuan-Jian Zhong, and Sarvjit Shastri. Pt–Au Alloying at the Nanoscale. *Nano Lett.*, 12(8):4289–4299, August 2012.

[131] Felipe Polo-Garzon, Zhenghong Bao, Xuanyu Zhang, Weixin Huang, and Zili Wu. Surface Reconstructions of Metal Oxides and the Consequences on Catalytic Chemistry. *ACS Catal.*, 9(6):5692–5707, June 2019.

[132] Agnieszka Poulain, Izabela Sobczak, and Maria Ziolek. Size of Au-Nanoparticles Supported on Mesostructural Cellular Foams Studied by the Pair Distribution Function Technique. *Cryst. Growth Des.*, 16(10):5985–5993, October 2016.

[133] Binay Prasai, A. R. Wilson, B. J. Wiley, Y. Ren, and Valeri Petkov. On the road to metallic nanoparticles by rational design: Bridging the gap between atomic-level theoretical modeling and reality by total scattering experiments. *Nanoscale*, 7(42):17902–17922, 2015.

[134] Clemens Prescher and Vitali B. Prakapenka. DIOPTAS: A program for reduction of two-dimensional X-ray diffraction data and data exploration. *High Pressure Res.*, 35(3):223–230, July 2015.

[135] Th. Proffen and S. J. L. Billinge. PDFFIT, a program for full profile structural refinement of the atomic pair distribution function. *J. Appl. Crystallogr.*, 32:572–575, 1999.

[136] Th. Proffen and R. B. Neder. DISCUS: a program for diffuse scattering and defect-structure simulation. *J. Appl. Crystallogr.*, 30:171–175, 1997.

[137] Huifeng Qian and Rongchao Jin. Ambient Synthesis of Au144(SR)60 Nanoclusters in Methanol. *Chem. Mater.*, 23(8):2209–2217, Am. Pharm. Rev. 2011.

[138] Huifeng Qian, Manzhou Zhu, Zhikun Wu, and Rongchao Jin. Quantum Sized Gold Nanoclusters with Atomic Precision. *Acc. Chem. Res.*, 45(9):1470–1479, Sep. Purif. Technol. 2012.

[139] H. M. Rietveld. A profile refinement method for nuclear and magnetic structures. *J Appl Cryst*, 2(2):65–71, June 1969.

[140] Emilie Ringe, Richard P. Van Duyne, and Laurence D. Marks. Kinetic and Thermodynamic Modified Wulff Constructions for Twinned Nanoparticles. *J. Phys. Chem. C*, 117(31):15859–15870, August 2013.

[141] S. Ristig, O. Prymak, K. Loza, M. Gocyla, W. Meyer-Zaika, M. Heggen, D. Raabe, and M. Epple. Nanostructure of wet-chemically prepared, polymer-stabilized silver-gold nanoalloys (6 nm) over the entire composition range. *J. Mater. Chem. B*, 3(23):4654–4662, June 2015.

[142] Tulio C. R. Rocha, Herbert Winnischofer, and Daniela Zanchet. Structural Aspects of Anisotropic Metal Nanoparticle Growth: Experiment and Theory. In *Complex-Shaped Metal Nanoparticles*, pages 215–238. John Wiley & Sons, Ltd, 2012.

[143] Nathaniel L. Rosi and Chad A. Mirkin. Nanostructures in Biodiagnostics. *Chem. Rev.*, 105(4):1547–1562, Am. Pharm. Rev. 2005.

[144] Johnny Saavedra, Hieu A. Doan, Christopher J. Pursell, Lars C. Grabow, and Bert D. Chandler. The critical role of water at the gold-titania interface in catalytic CO oxidation. *Science*, 345(6204):1599–1602, Sep. Purif. Technol. 2014.

[145] Panikkanvalappil R. Sajanlal, Theruvakkattil S. Sreeprasad, Akshaya K. Samal, and Thalappil Pradeep. Anisotropic nanomaterials: Structure, growth, assembly, and functions. *Nano Rev*, 2, February 2011.

[146] Naga Arjun Sakthivel, Shevanuja Theivendran, Vigneshraja Ganeshraj, Allen G. Oliver, and Amala Dass. Crystal structure of faradaurate-279: Au_{279}(sph-*t*bu)$_{84}$ plasmonic nanocrystal molecules. *J. Am. Chem. Soc.*, 139(43):15450–15459, November 2017.

[147] S. I. Sanchez, M. W. Small, E. S. Bozin, J.-G. Wen, J.-M. Zuo, and R. G. Nuzzo. Metastability and structural polymorphism in noble metals: The role of composition and metal atom coordination in mono- and bimetallic nanoclusters. *ACS Nano.*, 7(2):1542, 2013.

[148] Tapan K. Sau and Andrey L. Rogach. Colloidal Synthesis of Noble Metal Nanoparticles of Complex Morphologies. In *Complex-Shaped Metal Nanoparticles*, pages 7–90. John Wiley & Sons, Ltd, 2012.

[149] Caroline A Schneider, Wayne S Rasband, and Kevin W Eliceiri. NIH Image to ImageJ: 25 years of image analysis. *Nat. Methods.*, 9(7):671–675, July 2012.

[150] G. M. Sheldrick. Crystal structure refinement with SHELXL. *Acta Cryst C*, 71(1):3–8, January 2015.

[151] Chenyang Shi, Erin L. Redmond, Amir Mazaheripour, Pavol Juhás, Thomas F. Fuller, and Simon J. L. Billinge. Evidence for anomalous bond softening and disorder below 2 nm diameter in carbon supported platinum nanoparticles from the temperature dependent peak width of the atomic pair distribution function. *J. Phys. Chem. C*, 117:7226–7230, 2013.

[152] Millicent B. Smith, Katharine Page, Theo Siegrist, Peter L. Redmond, Erich C. Walter, Ram Seshadri, Louis E. Brus, and Michael L. Steigerwald. Crystal structure and the paraelectric-to-ferroelectric phase transition of nanoscale batio$_3$. *J. Am. Chem. Soc.*, 130(22):6955–6963, June 2008.

[153] Gabor A. Somorjai and Jeong Y. Park. Molecular Factors of Catalytic Selectivity. *Angew. Chem. Int. Ed.*, 47(48):9212–9228, 2008.

[154] Ren Su, Ralf Bechstein, Lasse Sø, Ronnie T. Vang, Michael Sillassen, Björn Esbjörnsson, Anders Palmqvist, and Flemming Besenbacher. How the Anatase-to-Rutile Ratio Influences the Photoreactivity of TiO_2. *J. Phys. Chem. C*, 115(49):24287–24292, December 2011.

[155] Yugang Sun, Brian Mayers, Thurston Herricks, and Younan Xia. Polyol Synthesis of Uniform Silver Nanowires: A Plausible Growth Mechanism and the Supporting Evidence. *Nano Lett.*, 3(7):955–960, July 2003.

[156] Yugang Sun and Younan Xia. Shape-Controlled Synthesis of Gold and Silver Nanoparticles. *Science*, 298(5601):2176–2179, December 2002.

[157] NguyetT. Tran, DouglasR. Powell, and LawrenceF. Dahl. Nanosized $pd_{145}(co)_x(pet_3)_{30}$ containing a capped three-shell 145-atom metal-core geometry of pseudo icosahedral symmetry. *Angew. Chem. Int. Ed.*, 39(22):4121–4125, November 2000.

[158] Matthew G. Tucker, David A. Keen, Martin T. Dove, Andrew L. Goodwin, and Qun Hui. RMCProfile: reverse Monte Carlo for polycrystalline materials. *J. Phys.: Condens. Mat.*, 19:335218, 2007.

[159] Tedi-Marie Usher, Daniel Olds, Jue Liu, and Katharine Page. A numerical method for deriving shape functions of nanoparticles for pair distribution function refinements. *Acta Crystallogr. Sect. Found. Adv.*, 74(4):322–331, July 2018.

[160] Sandra Vergara, Dylan A. Lukes, Michael W. Martynowycz, Ulises Santiago, Germán Plascencia-Villa, Simon C. Weiss, M. Jason de la Cruz, David M. Black, Marcos M. Alvarez, Xochitl López-Lozano, Christopher O. Barnes, Guowu Lin, Hans-Christian Weissker, Robert L. Whetten, Tamir Gonen, Miguel Jose Yacaman, and Guillermo Calero. MicroED Structure of Au146(p-MBA)57 at Subatomic Resolution Reveals a Twinned FCC Cluster. *J. Phys. Chem. Lett.*, 8(22):5523–5530, November 2017.

[161] Sandra Vergara, Dylan A. Lukes, Michael W. Martynowycz, Ulises Santiago, Germn Plascencia-Villa, Simon C. Weiss, M. Jason de la Cruz, David M. Black, Marcos M. Alvarez, Xochitl Lpez-Lozano, Christopher O. Barnes, Guowu Lin, Hans-Christian Weissker, Robert L. Whetten, Tamir Gonen, Miguel Jose Yacaman, and Guillermo Calero. Microed structure of $au_{146}(p\text{-mba})_{57}$ at subatomic resolution reveals a twinned fcc cluster. *J. Phys. Chem. Lett.*, 8(22):5523–5530, November 2017.

[162] Cong Wang, Jennifer D. Lee, Yichen Ji, Tzia Ming Onn, Jing Luo, Christopher B. Murray, and Raymond J. Gorte. A study of tetrahydrofurfuryl alcohol to 1,5-pentanediol over pt-wo_x/c. *Catal Lett*, 148(4):1047–1054, Am. Pharm. Rev. 2018.

[163] X. H. Wang, J.-G. Li, H. Kamiyama, M. Katada, N. Ohashi, Y. Moriyoshi, and T. Ishigaki. Pyrogenic Iron(III)-Doped TiO_2 Nanopowders Synthesized in RF Thermal Plasma: Phase Formation, Defect Structure, Band Gap, and Magnetic Properties. *J. Am. Chem. Soc.*, 127(31):10982–10990, August 2005.

[164] B. E. Warren. *X-ray Diffraction*. Dover, New York, 1990.

[165] Robert L. Whetten, Joseph T. Khoury, Marcos M. Alvarez, Srihari Murthy, Igor Vezmar, Z. L. Wang, Peter W. Stephens, Charles L. Cleveland, W. D. Luedtke, and Uzi Landman. Nanocrystal gold molecules. *Adv. Mater.*, 8(5):428–433, 1996.

[166] C. J. Wright and X.-D. Zhou. Computer-assisted area detector masking. *J Synchrotron Rad*, 24(2):506–508, March 2017.

[167] Jinfang Wu, Shiyao Shan, Valeri Petkov, Binay Prasai, Hannah Cronk, Pharrah Joseph, Jin Luo, and Chuan-Jian Zhong. Composition–Structure–Activity Relationships for Palladium-Alloyed Nanocatalysts in Oxygen Reduction Reaction: An Ex-Situ/In-Situ High Energy X-ray Diffraction Study. *ACS Catal.*, 5(9):5317–5327, Sep. Purif. Technol. 2015.

[168] Huayan Yang, Yu Wang, Xi Chen, Xiaojing Zhao, Lin Gu, Huaqi Huang, Juanzhu Yan, Chaofa Xu, Gang Li, Junchao Wu, Alison J. Edwards, Birger Dittrich, Zichao Tang, Dongdong Wang, Lauri Lehtovaara, Hannu Häkkinen, and Nanfeng Zheng. Plasmonic twinned silver nanoparticles with molecular precision. *Nat. Commun.*, 7:12809, Sep. Purif. Technol. 2016.

[169] Xiaohao Yang, Pavol Juhás, Christopher Farrow, and Simon J. L. Billinge. xPDFsuite: an end-to-end software solution for high throughput pair distribution function transformation, visualization and analysis. *arXiv*, 2015. 1402.3163.

[170] Xiaohao Yang, Ahmad S. Masadeh, James R. McBride, Emil S. Božin, Sandra J. Rosenthal, and Simon J. L. Billinge. Confirmation of disordered structure of ultrasmall CdSe nanoparticles from x-ray atomic pair distribution function analysis. *Phys. Chem. Chem. Phys.*, 15(22):8480–8486, 2013.

[171] Hengzhong Zhang, Bin Chen, Jillian F. Banfield, and Glenn A. Waychunas. Atomic structure of nanometer-sized amorphous TiO 2. *Phys. Rev. B*, 78(21), December 2008.

[172] Shu-Hong Zhang, Zhi-Yuan Jiang, Zhao-Xiong Xie, Xin Xu, Rong-Bin Huang, and Lan-Sun Zheng. Growth of Silver Nanowires from Solutions: A Cyclic Penta-twinned-Crystal Growth Mechanism. *J. Phys. Chem. B*, 109(19):9416–9421, May 2005.

[173] Weilie Zhou and Zhong Lin Wang. *Scanning Microscopy for Nanotechnology: Techniques and Applications*. Springer Science & Business Media, March 2007.

[174] Mirijam Zobel, Reinhard B. Neder, and Simon A. J. Kimber. Universal solvent restructuring induced by colloidal nanoparticles. *Science*, 347(6219):292–294, 2015.